Role of proteolytic processing of Opa1 in mitochondrial quality control and stress response

Inaugural – Dissertation zur

Zur Erlangung des Doktorgrades
der Mathematisch-Naturwissenschaftlichen Fakultät
der Universität zu Köln

vorgelegt von

Lilli Amal Pazurek-Weber

Angenommen im Jahr 2026

“What we know is a drop, what we don’t know is an ocean.”

— *Isaac Newton*

Table of contents

List of Figures

List of Tables

List of abbreviations

AAA	ATPase associated with diverse cellular activities
ADOA	Autosomal dominant optic atrophy
ADP	Adenosine diphosphate
AFG3L2	ATPase family gene 3-like subunit 2
ALS	Amyotrophic lateral sclerosis
AMP	Adenosine monophosphate
AMPK	Adenosine monophosphate-activated protein kinase
ANOVA	Analysis of variance
ATF4	Activating transcription factor 4
ATP	Adenosine triphosphate
BAK	Bcl-2 homologous antagonist/killer
BAX	Bcl-2-associated X protein
bp	Base pairs
CI-V	Respiratory complex 1-5
Ca^{2+}	Calcium ion
Cas9	CRISPR-associated protein 9
CCCP	Carboxycyanide m-chlorophenylhydrazone
cGAMP	Cyclic GMP-AMP
cGAS	Cyclic GMP-AMP synthase
CJs	Cristae junctions
CL	Cardiolipin
ClpXP	Clp protease ATP-binding subunit clpX-like
CLUH	Clustered mitochondria homologue
CRISPR	Clustered regularly interspaced short palindromic repeats
Cytb	Cytochrome b
DAMPS	Damage-Associated Molecular Patterns
ddC	2′,3′-dideoxycytidine
DNA	Deoxyribonucleic acid
DNP	2,4-dinitrophenol
dNTPs	Deoxy nucleoside triphosphate
DRP1	Dynamin-related protein 1
e^-	Electrons
eIF2α	Eukaryotic translation initiation factor 2 subunit alpha
ER	Endoplasmic reticulum
et al.	Latin et alii, meaning “and others”

ETC	Electron transport chain
EVs	Extracellular vesicles
FACS	Fluorescent activated cell sorting
$FADH_2$	Flavin adenine ainucleotide
FAM210A	Family with sequence similarity 210 member A
FAO	Fatty acid oxidation
FBS	Fetal bovine serum
FeS	Iron sulfur
FMN	Flavin mononucleotide
$FMNH_2$	1,5-Dihydroriboflavin-5'-(dihydrogen phosphate)
g	Gravity on earth
GDP	Guanosine diphosphate
GFP	Green fluorescent protein
GTP	Guanosine triphosphate
h	Hours
H^+	Protons
HRI	Heme-regulated inhibitor eIF2α kinase
HU	Hydroxyurea
IF	Immunofluorescence staining
IFIT3	Interferon induced protein with tetratricopeptide repeats 3
IFN	Interferon
IFNAR	Interferon-alpha-receptor
IM	Inner membrane
IMP	Inosine monophosphate
IMS	Intermembrane space
IRF3	Interferon regulatory factor 3
ISG	Interferon-stimulated gene
ISR	Integrated stress response
KD	Knockdown
KO	Knockout
KSS	Kearns-Sayre syndrome MELAS syndrome
LHON	Leber's hereditary optic neuropathy
LonP1	Lon protease homolog
m	Meter
M	Molar (mol/L)
m-AAA	Matrix AAA protease

MAVS	Mitochondrial antiviral signaling
MDVs	Mitochondrial derived vesicles
MEFs	Mouse embryonic fibroblasts
MELAS	Mitochondrial Encephalopathy, Lactic Acidosis, and Stroke-like episodes
MFN 1/ 2	Mitofusin 1/ 2
MGME1	Mitochondrial genome maintenance exonuclease 1
MIC19	MICOS subunit 19
MICOS	mitochondrial contact site and cristae organizing system
min	Minute
mPTP	Mitochondrial permeability transition pore
mRNA	Messenger RNA
mtDNA	Mitochondrial desoxyribonucleic acid
mTOR	Mechanistic target of rapamycin
MTS	Mitochondrial targeting sequence
NADH	Nicotinamide adenine dinucleotide (NAD) hydrogen (H)
NCR	Non-coding region
NF-κB	Nuclear factor kappa-light-chain-enhancer of activated B cells
NRF1/2	Nuclear Respiratory Factor 1 & 2
OM	Outer mitochondrial membrane
OMA	Overlapping activity with *m*-AAA protease
OPA1	Optical atrophy 1
OXPHOS	Oxidative phosphorylation
PAM	Presequence translocase-associated motor
PAMS	Pathogen-associated molecular patterns
PARL	Presenilin-associated rhomboid-like protease
PBS	Phosphate buffered saline
PC	Phosphatidylcholine
PCR	Polymerase chain reaction
PFA	Paraformaldehyde
PGC-1α	Peroxisome proliferator-activated receptor gamma coactivator 1-alpha
PI	Phosphatidylinositol
PINK1	PTEN-induced putative kinase 1
POLRMT	DNA-directed RNA polymerase, mitochondrial
PRELI	Protein of relevant evolutionary and lymphoid interest

PS	Phosphatidylserine
qPCR	Quantitative PCR
RIG-1	Retinoic acid inducible gene I
RNA	Ribonucleic acid
RNR	Ribonucleotide reductase
rNTPs	Ribonucleoside triphosphate
ROS	Reactive oxygen species
RT	Room temperature (approx. 22°C)
RT-qPCR	Real time quantitative PCR
SD	Standard deviation
SLP-2	Stomatin-like protein 2
SNX	Sorting nexin
SOD	Superoxide dismutase
STAT1/2	Signal transducer and activator of transcription 1/2
STING	Stimulator of interferon genes
TBK1	TANK-binding kinase 1
TCA cycle	Tricarboxylic acid cycle
TFAM	Transcription factor A, mitochondrial
TFB2M	Mitochondrial transcription factor B2
TIM23	Mitochondrial import inner membrane translocase subunit Tim23
TOM20	Translocase of outer mitochondrial membrane 20
tRNA	Transfer RNA
TWINKLE	Twinkle mtdna helicase
UCP1	Uncoupling protein 1
UPR	Unfolded protein response
VDAC	Voltage dependent anion channel
WT	Wildtype
YME1L	Yeast mitochondrial escape 1 like
µ	Micro
Δ	Delta
$\Delta\Psi_m$	Transmembrane potential
%	Percent
°C	Degree celsius
5-FU	5-fluorouracil

Abstract

Mitochondrial plasticity enables mitochondria to adapt to changing cellular demands through continuous remodeling of their morphology, proteome and function. This dynamic equilibrium is maintained by constant fusion and fission processes of the organelle. Proteins driving the mitochondrial dynamics are Drp1 and Mfn1/2 on the outer membrane (OM) and Opa1 on the inner membrane (IM). Mitochondrial plasticity is further controlled by the IM proteases Yme1l and Oma1, which influence mitochondrial signaling through substrate cleavage. While Yme1l performs constitutive housekeeping cleavage of the fusion-active l-Opa1 into soluble s-Opa1 at the S2 site, Oma1 acts as a stress-responsive protease and recognizes the S1 cleavage site in Opa1. Here, we showed that the expression of only one Opa1 isoform (isoform variant 1) is sufficient for embryonic and adult development in mice. Yme1l-mediated Opa1 cleavage is dispensable in basal conditions and upon metabolic and thermal stress. Additional suppression of Oma1-dependent processing through the modification of four amino acids in the S1 region of Opa1 also shows no phenotype until adult age. Nevertheless, we found evidence of unhealthy aging due to a lack of the Opa1 isoforms and processing in old age. These mild effects appear to be tissue-specific and vary in severity. By an additional introduction of an OXPHOS deficiency model, we identified the necessity of Opa1 processing by Oma1 for maintaining the balance of biogenesis and mitophagy in order to execute an adequate stress response. Mice lacking Opa1 processing fail to undergo compensatory cardiac hypertrophy upon *Cox10*$^{-/-}$, resulting in a shortened lifespan. Fibroblasts derived from these Opa1 mutants show decreased OXPHOS complexes, impaired respiration and reduced mtDNA maintenance. The imbalance of l- to s-Opa1 alters mitochondrial distribution within the cell, accompanied by a disruption of mitochondria-endoplasmic reticulum (ER) contact sites. The lack of Oma1-dependent Opa1 cleavage is associated with a delayed response upon H_2O_2 treatment and a reduced interferon-stimulated gene response (ISG response) under basal and nucleotide imbalance conditions. Proteomic analysis identified the interactome of s-Opa1 with OM proteins involved in fission, mitophagy, and cytoskeletal dynamics, providing an explanation for the disrupted mitophagy observed in Opa1-uncleavable hearts. In addition, we linked s-Opa1 to mitochondrial translation by identifying a promising interaction partner, Fam210a, which might explain the disrupted mitochondrial biogenesis *in vivo*. Together, our finding uncover a central role of Oma1-dependent Opa1 processing in coordinating mitochondrial architecture with stress adaptation, energy maintenance and in mitochondrial quality control.

1 Introduction

1.1 Mitochondria: Biology of life

In her endosymbiotic theory, Lynn Margulis postulated that eukaryotic cells evolved through the engulfment of archaeobacteria by a pre-eukaryotic cell. This symbiotic relationship gave rise to mitochondria that we know today containing double membranes, their own genome (mtDNA) and their ability to synthesize proteins (Introduction Figure 1)[1,2]. The inner mitochondrial membrane (IM) additionally forms so-called cristae, invaginations that protrude into the matrix and are rich in enzymes and other important proteins. Margulis[2] argued that mitochondria evolved from a symbiotic relationship between an α-proteobacteria and another eukaryotic cell 1.5-2 billion years ago. Over time, the ancestral host cell and the engulfed bacterium co-evolved into a highly coordinated endosymbiotic partnership forming modern mitochondria, which are present in all human tissues with the sole exception of mature erythrocytes. Mitochondrial function is especially crucial in tissues with high energy demands such as muscle cells, neurons, sensory cells, and oocytes. The quantity of mitochondria varies, typically ranging from 1,000 to 2,000 per cell and constituting roughly 25 % of cellular volume, though it can reach up to 36 % in cardiac tissue[3-5]. Their characteristic function is to generate adenosine triphosphate (ATP) via oxidative phosphorylation (OXPHOS), which occurs in the cristae of the IM (Introduction Figure 1). Electrons from nicotinamide adenine dinucleotide hydrogen (NADH), Flavin adenine dinucleotide ($FADH_2$), and 1,5-Dihydroriboflavin-5'-(dihydrogen phosphate) ($FMNH_2$) are transferred through complexes I-IV of the electron transport chain with a final ATP production at complex V (see section 1.1.2)[6]. Beyond energy metabolism, mitochondria regulate ion homeostasis, lipid metabolism, and programmed cell death-pathways[7-10]. Furthermore, they host both fatty acid β-oxidation (FAO) and the tricarboxylic acid (TCA) cycle generating intermediates that supply electrons to the respiratory chain[11]. When mitochondria malfunction, it can lead to a wide range of mitochondrial diseases, which are among the most common inherited disorders worldwide[12]. Well-known examples include Kearns-Sayre syndrome (KSS), MELAS syndrome (Mitochondrial Encephalopathy, Lactic Acidosis, and Stroke-like episodes), Leber's hereditary optic neuropathy (LHON), and Leigh syndrome. These disorders predominantly affect the neuromuscular system, emphasizing mitochondria’s critical role in high-energy-demand systems[13].

Mitochondrial inheritance is primarily maternal, as mitochondria from sperm are typically eliminated post-fertilisation. Consequently, mutations in mtDNA are chiefly transmitted via the maternal lineage[14]. This feature facilitates the use of mtDNA as a molecular marker for tracing maternal ancestry and human migration patterns across generations.

Mitochondria also play a significant role in ageing. With increasing age, mitochondrial efficiency declines, manifesting as accumulated mtDNA damage and higher reactive oxygen species (ROS) production[15]. This dysfunction results in diminished ATP synthesis, cellular stress, and contributes to aging phenotypes and age-related diseases, including Alzheimer's disease, Parkinson's disease, heart failure, and type 2 diabetes mellitus[16]. Given its central involvement, mitochondrial dysfunction represents a promising therapeutic target for age-associated pathologies.

1.1.1 Circular helix: The mtDNA

Mitochondria contain their own genome, a circular double-stranded DNA molecule. This mtDNA is located in the matrix and comprises 16,569 base pairs in humans, encoding 13 OXPHOS proteins, 22 tRNAs, and 2 rRNAs[17-19] (Introduction Figure 1). The remaining approximately 1,100 mitochondrial proteins are encoded in the nucleus and must be imported into the mitochondria mostly via a mitochondrial targeting sequence (MTS). The number of mtDNA copies per organelle varies depending on the cell type and physiological state but rarely exceeds ten. The mtDNA forms nucleoids, which are compacted by the TFAM (transcription factor A) protein[20]. This packaging protects the DNA from damage and enables the targeted regulation of transcription and replication. The replication of mtDNA occurs independently of the cell cycle and is regulated by a special control region (D-loop) performed by the DNA polymerase-γ (POLγ) and the DNA helicase TWINKLE which unwinds the DNA duplex[21]. Transcription initiation is driven by an mtDNA-directed RNA polymerase (POLRMT), with TFAM and TFB2M (mitochondrial transcription factor B2) serving as transcription factors [22,23]. The mitochondrial mRNA is translated by its own mitochondrial ribosomes (mitoribosomes) and tRNAs, which are also located in the matrix. Precise regulation of mtDNA copy number is crucial for maintaining cell health and is closely related to

metabolic demand. Primary mtDNA mutation may occur *de novo* and are usually presented in cells as heteroplasmic. Additionally, defects in mtDNA replication or maintenance machinery can generate mtDNA deletions, depletions or point mutations. Most of these mtDNA defect lead to a range of mitochondrial diseases varying from severe early onset multisystem diseases to mild adult onset pathologies. Clinical symptoms usually only appear once a certain threshold of mutated mtDNA molecules is reached[24]. This threshold can range from 60 % to 90 %, depending on the type of mutation and the affected tissue. Carriers of pathogenic mtDNA variants often remain symptom-free for a long time before the disease manifests, and even among carriers, the same mutation can vary in severity due to heteroplasmy, the concurrent presence of healthy and defective mtDNA molecules. This phenomenon also plays a role in disease inheritance. The number of mtDNA copies sharply decreases in oogenesis, the so-called bottleneck effect, resulting in random fluctuations in heteroplasmy in the next generation and leading to different disease manifestations in the offspring[25]. The influence of different mtDNA mutations on the human body has not yet been fully clarified and requires additional research.

1.1.2 Shuttle-service: The electron transport chain

The electron transport chain (ETC) is derived from prokaryotic ancestors and integrated into eukaryotic cells via mitochondrial endosymbiosis. During the TCA cycle, NAD^+ and FAD are reduced in the mitochondrial matrix, becoming electron carriers. Then, they shuttle electrons to the individual respiratory chain complexes (Introduction Figure 1)[26-28]. Complex I (NADH dehydrogenase; CI) oxidizes NADH and transfers the electrons to coenzyme Q through catalysis by flavin mononucleotide (FMN) and iron-sulfur (FeS) clusters. This reaction results in the translocation of 3 to 4 protons from the matrix to the IMS. Complex I is the largest ETC complex, comprising 44 subunits, the FMN prosthetic group, and eight FeS clusters. The downstream succinate dehydrogenase (complex II, CII) participates in both the citric acid cycle and ETC by oxidizing succinate to fumarate while transferring electrons via $FADH_2$ to coenzyme Q. The complex consists of four subunits and also harbors FeS clusters. The cytochrome c reductase (complex III, CIII) is formed by 11 subunits and oxidizes coenzyme QH_2, transferring electrons to cytochrome c. For each electron transferred, two H^+ are

pumped into the IMS. Complex IV (cytochrome c oxidase, CIV) comprises 13 subunits and an active metal center formed by heme a, heme a3, Cu_A, and Cu_B. It oxidizes cytochrome c and reduces molecular oxygen to water, using the energy released to pump four protons into the IMS. Oxidative phosphorylation takes place at complex V (CV), the ATP synthase, which consists of two parts. The F_1 part protrudes into the mitochondrial matrix, and the F_o part forms a proton channel through the IM. The proton gradient generated by the ETC is leveraged in the final step as H^+ ions are pumped back through the CV channel into the matrix. The voltage difference due to charge separation across the membranes (membrane potential or $\Delta\Psi$) together with the H^+ concentration gradient create the electrochemical gradient. The F_o subunit begins to rotate and energy is released, which is used by the F_1 subunit to synthesize ATP[29]. In the end 3 to 4 protons are used to convert ADP and phosphate into energy-rich ATP.

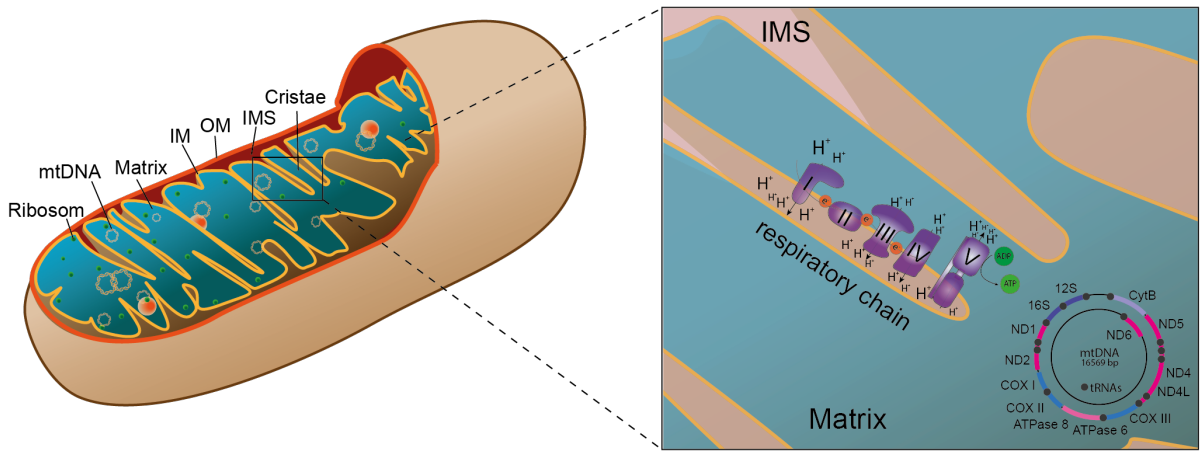

Introduction Figure 1: Detailed structure of a mitochondrion and its mtDNA. Schematic illustration of a mitochondrion with the outer membrane (OM), inner membrane (IM) and its invagination's (cristae), the intermembrane space (IMS) and matrix with mitochondrial ribosomes and the mtDNA. Close-up of the respiratory chain in the cristae tip and the encoded proteins in the mtDNA.

1.1.3 Inhibitors and decouplers of the respiratory chain

Several inhibitors have been identified that significantly disrupt the functionality of the ETC. They all attack at different targets: Rotenone and amobarbital are classic complex I inhibitors[30,31]. They block NADH oxidase activity, thus preventing electron transfer from NADH to coenzyme Q. Other very prominent inhibitors are antimycin A, which specifically prevents the transfer of electrons from coenzyme Q to cytochrome b in CIII, and oligomycin which directly blocks the proton channel in CV[32]. All these substances usually lead to increased ROS production. When electron transport

through the complexes is disrupted, they react with molecular O_2, resulting in the production of superoxide anions ($O2^-$). In a reaction catalyzed by superoxide dismutase (SOD), these negatively charged molecules can be further converted into hydrogen peroxide (H_2O_2) and hydroxyl radicals ($OH\cdot$), with potential damaging effects in the cell. They can damage DNA, oxidize proteins, or cause lipid peroxidation. Usually, oxidative stress leads to increased cell stress and commonly results in cell death (e.g. ferroptosis).

Uncoupling the respiratory chain separates the process of electron transport from ATP synthesis. Rather than using the H^+ stream via the proton channel in the CV, the ions flow back into the matrix before, releasing energy in the form of heat[33]. This mechanism is utilized physiologically by the uncoupling protein 1 (UCP1) in brown adipose tissue for thermogenesis. Chemical uncouplers such as 2,4-dinitrophenol (DNP) and carboxycyanide m-chlorophenylhydrazone (CCCP) bind H^+ ions in the IMS and transport them back into the matrix bypassing the ATP synthase. These uncouplers increase oxygen consumption and a significant loss of energy in the form of heat instead of ATP.

1.2 Keep it dynamic: Mitochondrial plasticity

Mitochondria range in size from 0.5 to 1.5 µm and can be bean-shaped, elongated, or spherical[34]. Mitochondria form a dynamic network that undergoes continuous fusion and fission events, spanning the entire cell. Mitochondrial plasticity enables the organelles to adapt their structure, function, and distribution in response to cellular demands[35]. These adaptations allow mitochondria to flexibly support cellular energy needs, oxidative stress, and metabolic states. Cellular conditions such as nutrient excess or dysfunction can disrupt the mitochondrial network and drive fission, enabling mitophagy and removal of damaged mitochondria. In contrast, increased fusion can be promoted as a protective response to metabolic stress, to increase ATP production and to prevent cell death[36,37]. Thus, the mitochondria morphology is tightly regulated by so-called “mitochondria-shaping” proteins[38]. The dynamin-like GTPases mitofusin1 (MFN1) and mitofusin2 (MFN2) mediate the outer membrane fusion whereas the optic atrophy 1 (OPA1) protein controls the fusion of the inner membrane. Conversely, the dynamin-related protein 1 (DRP1) mediates outer membrane fission[39-41]. Regulation of

dynamics goes down to the proteolytic level and is mainly controlled by the proteases overlapping activity with *m*-AAA protease (OMA1) and yeast mitochondrial escape 1 like (YME1L). They mediate processing of OPA1 in the IM, which is triggered by stress signals and posttranslational mechanisms. These processes modulate mitochondrial morphology and function, enabling the cell to precisely respond to environmental challenges and maintain cellular adaptation (more in section 1.2.1-1.2.3).

1.2.1 YME1L- Master regulator of mitochondrial proteostasis

The mitochondrial *i*-AAA protease YME1L is localized in the IM and is a key player in protein homeostasis and mitochondrial dynamics[42]. The homohexameric protease features an ATPase domain which couples the ATP hydrolysis to substrate processing, as well as a metallopeptidase domain located in the IMS, where YME1L degrades numerous mitochondrial proteins, including components of the respiratory chain and mitochondrial dynamics machinery, among others[43]. It degrades unassembled respiratory chain subunits such as NDUFB6, COX4, and ND1 and prevents their deposition and possibly deleterious effects[44]. Substrates also include components of the TIM23 and TIM22 complexes, such as ROMO1 a part of the TIM23 complex, which are responsible for importing proteins into mitochondria[45]. YME1L also degrades proteins like TOM22 and OM45 at the OM to maintain the membrane quality[46]. One of the most studied regulatory functions of YME1L is the proteolysis of OPA1 to ensure the balance between fusion and fragmentation of the mitochondria (Introduction Figure 2)[47]. Furthermore, YME1L interacts with the scaffold protein SLP-2 (or STOML2) and the protease PARL forming the so-called SPY complex[48]. SLP2 acts as a membrane scaffold and anchors PARL and YME1L in the IM. The spatial organization of the proteases leads to efficient proteolysis and significantly supports mitochondrial integrity. Furthermore, YME1L influences lipid synthesis by targeting PRELI (protein of relevant evolutionary and lymphoid interest)-like lipid transfer proteins and proteins important for phosphatidylserine synthesis[42,49]. Conversely, upon hypoxia or nutrient starvation, mTOR (mechanistic target of rapamycin) inhibition triggers a signaling cascade that eventually leads to decreased PE levels in the IM which promotes YME1L proteolysis[49,50]. YME1L broadly rewires the mitochondrial proteome and metabolic function and limits mitochondrial biogenesis by degrading key components of protein translocases in the IM and lipid transfer proteins in the IMS[51]. Loss of YME1L leads to

mitochondrial fragmentation due to a lack of OPA1 regulation and by activating OMA1. *YME1L*$^{-/-}$ cells further show significantly increased ROS and reduced ATP production. *In vivo*, deletion of Yme1l in the whole body is embryonical lethal[52]. Tissue-specific *Yme1l*$^{-/-}$ in mice lead to different manifestations depending on the target: In neuronal cells, *Yme1l*$^{-/-}$ leads to severe neurodegenerative defects, increased mitochondrial fragmentation, increased apoptosis, and a reduced lifespan[49,53]. Neuronal function is severely impaired, leading to motor and cognitive deficits. In the retina of neuron-specific (Nestin-cre) *Yme1l*$^{-/-}$ mice the defective proteostasis results in a neuroinflammatory response (interferon-stimulated gene response, ISG response). This ISG response occurs due to increased mtDNA release and activation of the cGAS-STING pathway. *Sprenger et al.* showed that the mtDNA release is based on a nucleotide imbalance triggered by pyrimidine deficiencies due to *Yme1l*$^{-/-}$, which results in an increased incorporation of ribonucleotides into mtDNA and replication stress[54]. In muscles, *Yme1l*$^{-/-}$ results in muscle atrophy, reduced ATP production, and increased ROS production, leading to muscle atrophy[55].. In summary, Yme1l is responsible for maintaining mitochondrial protein homeostasis, regulating mitochondrial dynamics, and controlling mitochondrial signaling, and it targets a wide range of substrates that are essential for mitochondrial function.

1.2.2 OMA1- The heart of mitochondrial quality control

The mitochondrial metalloprotease OMA1 is localized to the IM[56] and plays a central role in the stress response and quality assurance of mitochondria. The structure of OMA1 has not yet been fully elucidated, nevertheless homology models suggest that OMA1 possesses multiple transmembrane α-helices that form a type of pore or reaction chamber in the membrane[57]. OMA1 is a metallopeptidase of the M48 family and possesses a HEXXH zinc motif at its catalytic center. The protease most likely forms homo-oligomeric complexes that are embedded in the IM. OMA1 is activated upon different stressors such as the loss of membrane potential (ΔΨm), oxidative stress, ATP depletion, and impaired protein import via a special N-terminal sensor region[58]. Activation of this region results in a conformational change and oligomerisation of the protease into its active form. In addition, OMA1 is autocatalytically degraded or degraded by YME1L[59] that ensures the reversibility of the stress response. In the IM, OMA1 recognizes and cleaves its substrates such as OPA1

and DELE1 (Introduction Figure 2)[58,60,61]. This allows OMA1 to intervene in mitochondrial dynamics and actively act in stress signaling cascades. In addition, OMA1 regulates mitochondrial fission and mitophagy under certain stress conditions via the degradation of PGAM5[48,62]. PGAM5 has been shown to regulate mitophagy, however, cleavage via OMA1 only takes place under specific stress conditions such as in PARL loss. OMA1 also regulates mitochondrial protein import quality by cleaving the chaperone DNAJC15, enabling its degradation by the m-AAA protease AFG3L2[63]. This influences the import of OXPHOS proteins and affects mitochondrial protein homeostasis. Upon PARL inhibition, OMA1 cleaves mislocalized PINK1 (PTEN-induced putative kinase 1) proteins, which also supports mitochondrial quality control[64]. Recent studies have described OMA1 a potential "metabolic safeguard" linking it activity to the regulation of glucose utilisation and mitochondrial metabolism[65]. Under DNA damage induced stress, the loss of OMA1 led to the accumulation of OXPHOS proteins, reduced glycolysis and cell death. Mice lacking Oma1 are viable and fertile, but develop obesity and impaired thermogenesis[66]. In brown adipose tissue, Oma1-mediated disruption of Opa1 processing leads to enlarged, rather fused mitochondria, reduced β-oxidation, and impaired cold adaptation[66]. White adipose tissue mass increases, and the mice develop fatty livers upon high fat diet. Loss of Oma1 in skeletal muscle results in reduced expression of nuclear-encoded mitochondrial genes (e.g., Sdha, Atp5a), indicating that the resulting changes in mitochondrial dynamics and quality control lead to adjustments in gene expression. Oma1 deletion leads to very mild phenotype raising the question of its role in cellular function. To tackle this question, many studies have crossed Oma1 depleted mice with additional knock-out models that show mitochondrial dysfunction. In hippocampal neurons, deletion of Phb2 leads to destabilization of Opa1 and neurodegenerative changes[67]. Additional loss of Oma1 prevents the destabilization of Opa1 and mitigates the neurodegenerative effects, demonstrating that active Oma1 plays a harmful role. Similar observations were made for *Yme1l*$^{-/-}$ in cardiomyocytes[52]. The knockout leads to Oma1-dependent fragmentation of the mitochondria and dilated cardiomyopathy. The additional deletion of Oma1 prevents Opa1 cleavage and normalizes mitochondrial morphology and heart function. However, if *Yme1l*$^{-/-}$ occurs in the central nervous system, additional deletion of Oma1 restores mitochondrial morphology but axonal degeneration is worsened[53]. This study highlights that Oma1 has a dual role and is also protective in stress conditions. This was also demonstrated in a cardiac

and skeletal muscle-specific *Cox10*$^{-/-}$ model[68]. *Cox10*$^{-/-}$ mice develop early-onset cardiomyopathy, skeletal muscle atrophy resulting in early death whereas additional loss of Oma1 leads to worsening cardiomyopathy and the overall phenotype. Here, the protease is essential for the activation of the mitochondrial integrated stress response (ISR^{mt}) via Dele1, which mediates protection against cardiac damage via ferroptotic cell death. Overall, findings from various knockout models show tissue- and context-specific effects of Oma1 showing that the precise balance of Oma1 activity is essential for maintaining mitochondrial dynamics and organ function under stressed conditions.

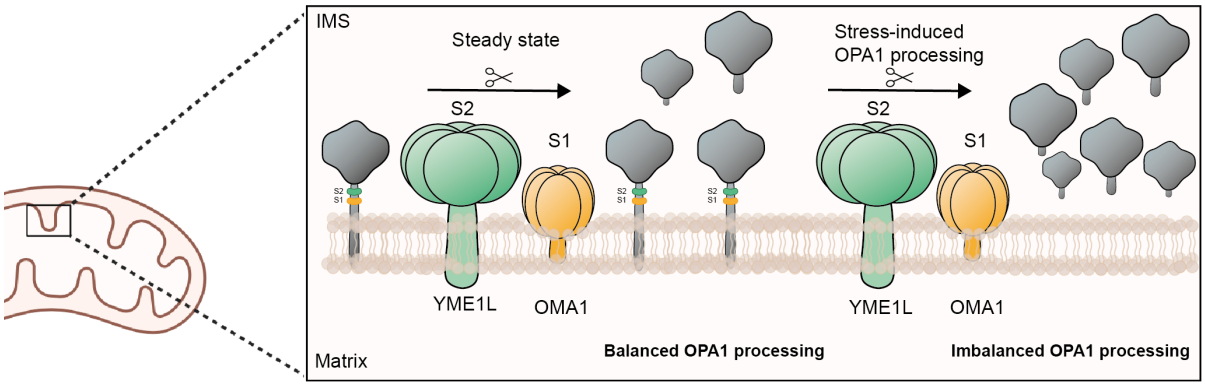

Introduction Figure 2: Model of OPA1 processing by YME1L and OMA1. Within the IM, YME1L (green) and OMA1 (yellow) cleave OPA1(grey) in steady state resulting in balanced OPA1 processing. Upon stress activation, excessive OPA1 cleavage results in imbalanced processing.

1.2.3 A balancing act: l-OPA1 and s-OPA1

OPA1 is a nuclear encoded protein that is transported into the mitochondria where it is embedded in the IM with an N-terminal transmembrane domain. The dynamin-like protein is evenly distributed in the IM and is involved in the cristae and the cristae junctions (CJs) organization[69], the narrowing of the IMS. OPA1 is one of the mitochondrial shaping proteins that controls the fusion of the IM in cooperation with the mitofusins (MFN1/MFN2 on the OM), thereby enabling the tubular network state of the mitochondria[70]. At the same time, OPA1 stabilizes the cristae structure, interacts with MICOS, and thus prevents the opening of CJs and the release of cytochrome c[69]. Through these structural functions, OPA1 directly links the organization of the IM to mitochondrial respiration[71] by ensuring the efficiency of oxidative phosphorylation and protection against stress-induced fragmentation and depolarization (more in 1.2.4) [69,72]. OPA1 has several functional domains: a GTPase domain (motor function), a BSE domain (lever), a stalk and a membrane-associated “paddle” region that allows

attachment and deformation of the membrane[73]. The protein assembles into tightly coiled helices that attach to the lipid membrane of the inner mitochondrial membrane. The binding of OPA1 to specific lipids, such as cardiolipin, supports membrane stabilization and promotes fusion efficiency[74]. OPA1 oligomerizes dynamically, with its uncleaved and cleaved form, and assembles into hetero-oligomeric complexes. During the fusion process, membrane-bound OPA1 proteins form cis/trans oligomers on opposing membranes[75]. GTP binding induces assembly on membrane tubules, and hydrolysis triggers a “power stroke” that reduces the distance between the membranes. Repeated GTP cycles cause hemi-fusion of the membranes and pore formation in the inner membrane. Cardiolipin interactions and OPA1 oligomers stabilize the intermediate states[76,77].

In humans, eight transcript variants encoding different isoforms of OPA1 have been found (V1-V8), which differ in the exons 4, 4b, 5 and 5b. Interestingly, only isoforms 1, 5, 7 and 8 are present in mice which are differently expressed throughout the body. OPA1 activity is proteolytically regulated. The long, membrane-bound form (l-OPA1), OPA1 is fusion active. Upon specific cutting by the proteases YME1L and OMA1, soluble short fragments (s-OPA1) are created lacking the membrane anchor[78]. The exact function of s-OPA1 remains unclear. In the soluble form, however, the protein is no longer capable of membrane fusion. Under physiological conditions, a balance of l- and s-OPA1 exists. Recently, it has been shown that the balanced ratio of l- and s-OPA1 plays a significant role in mediating fusion[75]. While l-OPA1 alone is sufficient for membrane fusion, the process is more efficient and faster with the presence of s-OPA1 (heterotypic membrane tethering)[75]. Under stress or in mitochondrial dysfunction, OMA1 is activated and processes OPA1 into its short form (disrupted l-/s-OPA1 balance). The fusion-active l-OPA form is cleaved, and ongoing fission events result in mitochondrial fragmentation. In addition to membrane fusion, OPA1 also fulfils many other functions. Mutations in the *OPA1* gene lead to autosomal dominant optic atrophy (DOA) disease in humans which is characterized by ataxia, hearing impairment and blindness. OPA1 is essential for embryonic development as the knockout mice die at around at embryonic day 9[79]. Heterozygous $Opa1^{+/-}$ mice, analogous to human ADOA, show age-dependent progressive degeneration of retinal ganglion cells with optic nerve atrophy and loss of visual acuity, while other tissues show only mild or subclinical mitochondrial changes[57]. In addition to membrane fusion, OPA1 controls cristae shape and thus OXPHOS function and participates in mtDNA maintenance. In MEFs, the loss

of Opa1 leads to highly fragmented mitochondria and a depletion or disorganisation of cristae in the form of a “ballooned” matrix space. Opa1$^{-/-}$ MEFs respiration is severely affected, with reduced OXPHOS and supercomplex assembly, and the cells rely on glycolysis. The mtDNA content is decreased by two-thirds and the mtDNA molecules are no longer efficiently distributed in the mitochondria[80,81]. Re-expression of all individual Opa1 isoforms largely restores OXPHOS capacity, respiratory complex levels and ATP production, thereby normalizing bioenergetic function[82]. Also re-expressing isoform 5 that is only present as s-OPA1 due to continual processing can also restore morphology, mitochondrial respiration, and mtDNA levels. However, Opa1v5 does not restore mitochondrial fragmentation as l-Opa1 is essential for fusion. Nevertheless, the presence of l- and s-OPA1 is required to restore complete cristae organisation and mitochondrial dynamics. *In vitro* studies documented that OPA1 overexpression is proteotoxic for the cell and results in mitochondrial fragmentation and increased apoptosis which further enhances the idea that balanced levels of s- and l-OPA1 isoforms are critical[83].

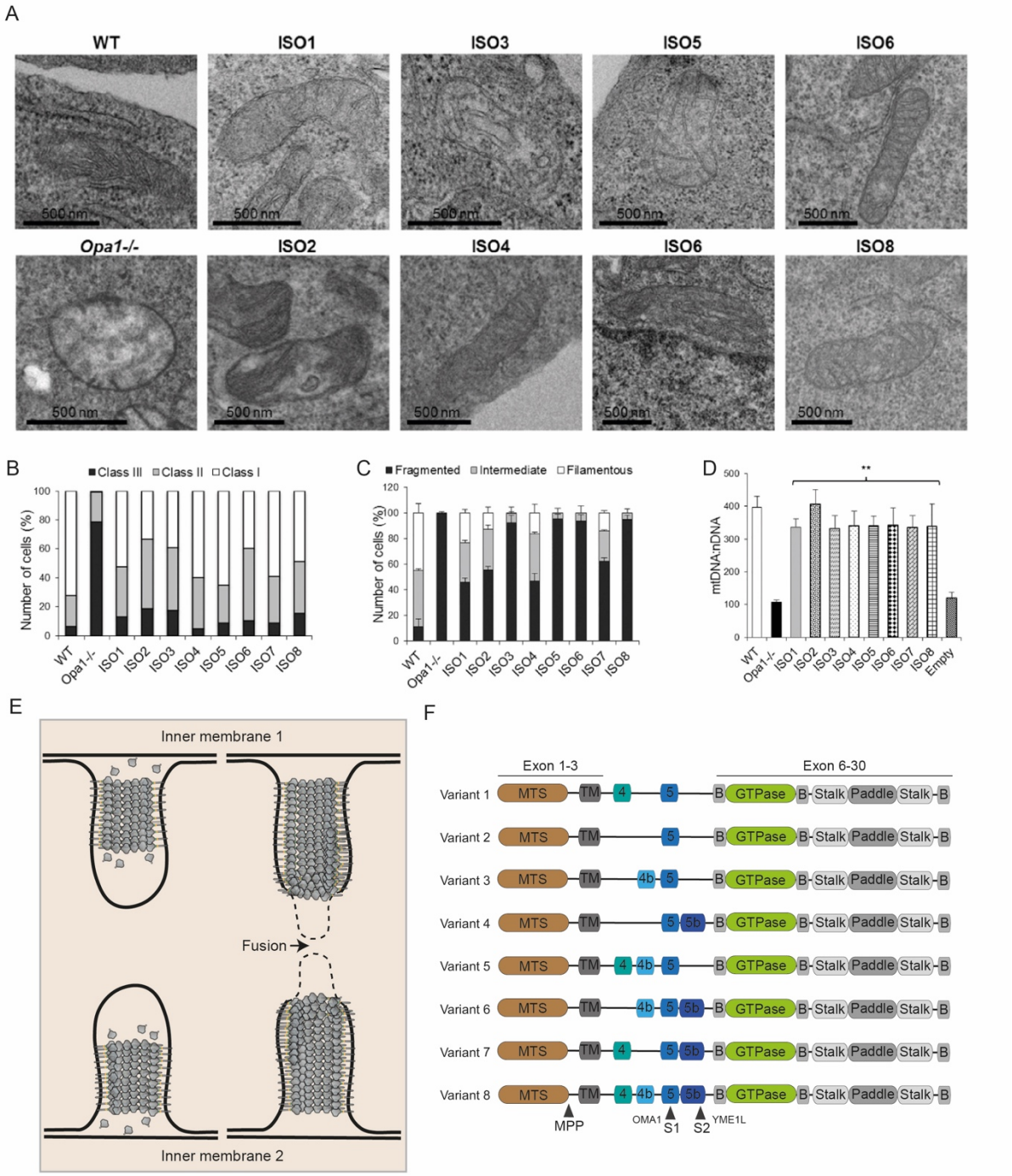

Introduction Figure 3: OPA1 isoforms and oligomerization during fusion and cristae formation. (A-D): Observations from Del Dotto et al. (2017)[82] showing that *Opa1*$^{-/-}$ results in loss of cristae formation and the restoration by the integration of the various OPA1 isoforms (Class I: more than four cristae, class II: between two and three cristae, class III: one or no cristae per mitochondrion). Observation of overall mitochondrial morphology and mtDNA content in WT and *Opa1*$^{-/-}$ MEFs with reintegrated isoforms 1 to 8. **(E):** Model of OPA1-mediated fusion. OPA1 oligomerized on the IM creating a membrane tube. GTP hydrolysis leads to a conformational change in the quaternary structure resulting in membrane curvature at the tip of the tubule allowing easy fusion with the adjacent membrane. Adapted from[84]. **(F):** Human OPA1 isoforms 1 to 8 harboring the different exons 4, 4b, 5 and 5b. MTS is cleaved by MPP protease, and the S1 and S2 cleavage sites are recognized by OMA1 and YME1L.

1.2.4 The diverse nature of cristae

Cristae are the characteristic invaginations of the IM, which greatly increase the membrane surface area and form the main site of the respiratory chain and ATP synthase. They are functionally crucial as their shape and density directly determine how efficiently a mitochondrion can produce ATP and control signals like cytochrome c release[85-87]. Cristae are not static structures, but rather 3D formations with a complex topology. They can appear as stacked lamellae with flat, plate-like membrane folds that are densely packed in overlapping leaves, creating a large respiratory surface area with a small volume[88]. In addition, cristae can appear as tubular structures, protruding into the matrix in a pipe-like form[89]. They often split off as they pass through the matrix, forming a network system[90]. Tomography shows that there are smooth transitions between lamellar and tubular sections. “Cut-through” cristae are cristae that appear to form separate segments in cross sections, but are actually part of a continuous, three-dimensionally intertwined fold. Additionally, cristae can form lamellar-like structures which holes or openings in the membrane sheet[90]. Depending on the cell type, metabolic state, and protein composition, cristae can be dynamically remodelled and lengthen or shorten, fuse or divide and open or close their CJs within seconds to minutes. The MICOS complex is preferentially located at CJs and defines the position and number of them[91,92]. ATP synthase dimers localize at the cristae tips and enables strongly curved crista edges. Together with OPA1 oligomers these proteins form a functional network to maintain the cristae integrity.[93] Hereby, l-OPA1 promotes lamellar, longer cristae while s-OPA1 dominance is associated with tubular, vesicular cristae morphology[94]. OPA1-dependent cristae modulation has emerged as a central mechanism by which mitochondria flexibly adapt their IM architecture to the energy status of the cell. Work by *Patten et al.* has shown that upon starvation conditions, OPA1 oligomerization increases, leading to a narrowing of the cristae lumen, an organized stacking of lamellar cristae and a more stable organization of ATP synthase dimers and supercomplexes[93]. These structural adaptations improve the coupling of electron transport and ATP synthesis while protecting against uncontrolled cytochrome c release and apoptotic sensing. Nevertheless, only l-OPA1-regulated cristae exhibit suboptimal adaptation to metabolic stress and are functionally rather inflexible[94]. Under conditions of increased OPA1 cleavage (e.g. cellular stress resulting in OMA1 activation), the cristae become shorter and more irregular in shape, with a tubular appearance[94]. Tomography studies of s-OPA1-dominant cells also reveal an enlarged

cristae lumen and widened CJs, associated with unstable OXPHOS organisation and increased cytochrome c release[95]. Only the balance of l- and s-Opa1 allows stable CJs for optimal respiration and dynamic adaptation to external influences.

1.3 Biogenesis and protein synthesis to increase the mitochondrial mass

Mitochondrial biogenesis needs to be balanced between the transcription and translation of genes in the mitochondrial and nuclear genomes to produce all the proteins required to increase mitochondrial mass and to replicate mtDNA. AMPK (adenosine monophosphate-activated protein kinase) functions as a cellular energy sensor that is activated when cellular energy demand increases[96], thereby promoting mitochondrial biogenesis. The kinase directly phosphorylates PGC-1α (Peroxisome proliferator-activated receptor gamma coactivator 1-alpha) and coactivates NRF1/2 (Nuclear Respiratory Factor 1 & 2) and TFAM, key regulators of the mitochondrial biogenesis. These transcription factors control the expression of genes responsible for mitochondrial DNA replication, transcription, protein synthesis, and the assembly of respiratory chain complexes. Upregulation of PGC-1α results in gene expression involved in oxidative metabolism and glucose uptake[97]. Meanwhile, TFAM stabilizes mtDNA by packaging it, thereby supporting the recruitment of mitochondrial RNA polymerase and other transcription factors. NRF1 and NRF2 activate genes that code for mitochondrial respiratory complexes, antioxidants, and import proteins. Majority of mitochondrial proteins synthesized in the cytosol need to be imported into the mitochondria. This can be done for example via specific import signal sequences that allows them to enter the mitochondria through the TOM (translocase of the outer membrane) and TIM (translocase of the inner membrane) complexes[98-100]. Chaperones, primarily Hsp70, assist in the proteins' correct folding and integration into the compartments. In addition to protein synthesis, lipid synthesis is essential for membrane formation. Mitochondria synthesize a subset of lipids, including phosphatidylethanolamine (PE) and cardiolipin, that are crucial for the integrity and function of the IM[101]. Other membrane components, such as phosphatidylcholine (PC), phosphatidylserine (PS), and phosphatidylinositol (PI), are synthesized in the endoplasmic reticulum (ER). The lipids are then transported to the mitochondria via membrane contact sites or special lipid transfer proteins, where they are incorporated into the membrane[102].

1.4 Mitochondrial quality control

Mitochondria use a network of several quality control mechanisms, ranging from molecular proteostasis to the removal of entire organelles. These mechanisms interact chronologically and hierarchically to minimize damage and, if the initial levels of control fail, to selectively eliminate defective mitochondria[103]. On molecular level, antioxidant systems (e.g., glutathione/peroxiredoxin systems) limit oxidative damage to proteins, lipids, and mtDNA[104]. Furthermore, chaperones and mitoproteases such as LonP1 (Lon protease homolog) and ClpXP (Clp protease ATP-binding subunit clpX-like) within the matrix recognize misfolded or damaged proteins and undergo regulatory processing[105]. They serve as first intramitochondrial defense against proteotoxicity and are closely linked to higher levels of quality control. By controlling the processing of fusion factors like OPA1, YME1L and OMA1 also directly link protein damage to fragmentation or stabilization of the network[106]. Failure or overload of these quality control systems leads to the accumulation of misfolded proteins within mitochondria and triggers the mitochondrial unfolded protein response (UPR^{mt})[107]. This is a distinct stress-response form from the UPR^{ER} although both share the common goal of restoring proteostasis and partially use same signalling cascade[108]. In mammals, major stress signaling is driven by the processing of DAP3-binding cell death enhancer 1 (DELE1)[109]. Upon cellular or mitochondrial stress, DELE1 is cleaved by OMA1 during the import process, leading to its release back to the cytosol[110]. The accumulated c-terminal fragments bind to and activate the heme-regulated eIF2α kinase (HRI) which phosphorylates eIF2α, the eukaryotic initiation factor 2α. In basal conditions, eIF2α aids in the initiation of mRNA translation. The phosphorylated initiation factor shows reduced activity and thus inhibits global protein synthesis. At the same time, it specifically promotes the translation of the transcription factor ATF4 (activating transcription factor 4). ATF4 translocates to the cell nucleus, where it controls stress gene expression by inducing protective genes for amino acid biosynthesis, autophagy, and antioxidants. It works together with other transcription factors such as CHOP or ATF3 by forming homo- or heterodimers, which leads to various cellular effects[111]. The basal processing of DELE1 in the import process thus serves as a sensor to transmit the state of the mitochondria to the cytosol and the cell nucleus. However, overactivation of OMA1 can also lead to chronic ISR activity due to excessive cleavage of DELE1, which can result in pathological outcomes like neurodegenerative diseases, chronic inflammation, metabolic disorders, and cancer[112]. In general, ISR activation is

triggered by various stress stimuli such as ER stress, nutrient deprivation, viral signals, and iron and mitochondrial stress via four specialized eIF2α kinases (PERK, GCN2, PKR, and HRI), with only the latter being dependent on the OMA1-DELE1 axis[113,114].
For quality control on organelle level, mitochondria can form small compartments containing oxidized or misfolded components. These so-called mitochondria-derived vesicles (MDVs) are small, 70–150 nm in size, single- or double-membrane vesicles that bud off under mild mitochondrial stress. They selectively remove oxidized or misfolded proteins and damaged lipids from still functional mitochondria and degrade them via the endosomal-lysosomal or peroxisomal pathway[115]. The formation of these vesicles requires coordinated recognition of the damaged compartment by recruiting quality control and sorting factors such as the Parkinson's-associated proteins PINK1 and Parkin or β-barrel OM proteins like TOM20 (Translocase of outer mitochondrial membrane 20) or VDAC1 (voltage-dependent anion channel)[116]. MDVs are directed to late endosomes, lysosomes, or peroxisomes via a SNARE-based fusion. They represent an early, sub-organellar quality control route that precedes complete mitophagy and maintains the integrity of the mitochondrial network. The mitophagy pathway ensures the selective clearance of complete dysfunctional mitochondria, maintaining cellular health and mitochondrial quality[117,118]. It involves a complex interplay of sensors, ubiquitin ligases, adaptor proteins, and autophagy machinery that together regulate mitochondrial turnover and prevent cellular damage. Mitophagy is triggered by cellular stress or the loss of mitochondrial membrane potential. The most studied form of mitophagy is the PINK1-PARKIN mediated pathway, where PINK1 accumulates on the outer mitochondrial membrane, recruiting the E3 ubiquitin ligase Parkin[119]. The ligase tags outer membrane proteins with ubiquitin, marking the mitochondria for degradation. Adapter proteins such as p62/SQSTM1, OPTN, and NDP52 recognize these ubiquitin tags and link the damaged mitochondria to LC3 (microtubule-associated protein 1A/1B-light chain 3). During this process, LC3 undergoes conversion from LC3-I to its lipidated LC3-II form, which is incorporated into the autophagosome membrane. The autophagosome engulfs the damaged mitochondria and later fuses with lysosomes to enzymatically degrade the contents. OM proteins like BNIP3, NIX, FUNDC1, and BCL2L13 already possess LC3-interacting regions (LIRs) and can directly recruit autophagosomes without prior ubiquitination steps[120-122].

1.5 Gate keeper: Mitochondria as signaling platform

As an essential and abundant component of the cell, mitochondria act as central signaling hubs. They process signals such as the nutritional status, redox balance or proteostasis of the cell and transmit them, for example, by direct contact with other organelles. This enables the cell to control its metabolism, stress- and immune responses. The ISR and mitophagy are among those pathways, being part of the cell's stress and quality control. To adapt to energy and nutrient availability, mitochondria use metabolic signaling via AMPK, mTOR, and sirtuin 1 (SIRT1). As already mentioned, AMPK controls mitochondrial biogenesis, however it can also promote autophagy via the phosphorylation of ULK1 in order to recycle damaged cell components[123]. Via indirect interaction, AMPK can activate SIRT1 by increasing NAD^+ levels. SIRT1 is an NAD^+-dependent deacetylase whose activity also increases mitochondrial biogenesis and antioxidant capacity. Both enzymes indirectly inhibit mTOR[124]. mTOR is a central serine/threonine kinase that acts as a molecular sensor and regulator for cell growth, metabolism, and survival. It promotes anabolic processes and inhibits catabolic ones, allowing cells to grow and divide when energy supplies are adequate. mTOR consists of the complexes mTORC1, which activates protein biosynthesis and lipid synthesis and inhibits autophagy, and mTORC2, which is necessary for cytoskeletal engagement and cell proliferation[125].

ROS, which is generated in mitochondria, can act as a signaling molecule by activating the central NF-κB signaling pathway[126]. In its resting state, NF-κB is bound to an inhibitory protein called IκB in the cytoplasm. After stimulation by ROS and other mitochondria-derived stimuli, IκB is phosphorylated and subsequently ubiquitinated, leading to its proteasomal degradation. This releases NF-κB, allowing it to translocate to the cell nucleus, where it activates the transcription of target genes such as pro-inflammatory cytokines or anti-apoptotic proteins (Bcl-2 family). Furthermore, mitochondrial calcium buffering is an essential mechanism for regulating cellular energy production and signal transduction. Mitochondria primarily take up calcium ions (Ca^{2+}) via the mitochondrial calcium uniporter (MCU), stabilized by the adapter protein EMRE[127]. The uptake in turn influences the activity of enzymes in the citric acid cycle and increases ATP synthesis. Conversely, the release of Ca^{2+} is controlled by VDAC and mPTP (mitochondrial permeability transition pore), which can trigger apoptosis and other signals[128,129]. Calcium can be transferred directly from the ER to the mitochondria via so-called mito-ER contact sites mediated by MFN1 and MFN2[130].

Ca^{2+} release is regulated via IP3R in whereby the heat shock protein GRP75 connects IP3R with VDAC, facilitating the cation exchange[131].

Mitochondria can also initiate programmed cell death by releasing mitochondrial cytochrome c via BAX/BAK pores (Bcl-2 associated X protein/ Bcl-2 homologous killer) [132,133]. Cytochrome c binds to the adapter protein Apaf-1 and forms an apoptosome complex together with ATP. The apoptosome activates caspase-9, the initiator caspase, which in turn activates other effector caspases (caspase-3, -6, -7). These enzymes catalyze the degradation of cellular proteins and lead to the apoptosis of the cell. Together with ATP and ROS production and the generation of NAD^+, mitochondria can regulate whether the cell needs more organelles and energy, divides, or undergoes apoptosis.

Mitochondria also influence epigenetic programs, primarily by providing key metabolites that serve as substrates or cofactors for epigenetic enzymes directly affecting DNA methylation and histone modifications in the cell nucleus. Acetyl CoA, derived from glucose metabolism, fatty acid oxidation, and amino acid catabolism, is an obligate substrate for histone acetyltransferases[134]. Elevated acetyl CoA levels promote a more open chromatin structure and stimulate growth and differentiation, while limiting levels restricts histone acetylation and proliferation[135]. The metabolites α-ketoglutarate, succinate, and fumarate, products from the TCA cycle, are essential cofactors for dioxygenases (DNA demethylation) and histone demethylases. High α-ketoglutarate levels promote demethylation of DNA and histones, whereas succinate and fumarate compete with α-ketoglutarate and competitively inhibit these dioxygenases[135,136]. Modulation of mtDNA copy number or OXPHOS defects resulting in systematic changes in the metabolome (amino acids, NAD^+/NADH) are associated with changes in DNA methylation and histone marks even before severe bioenergetic deficits are measurable[137,138]. NAD^+ acts as a co-substrate of NAD^+-dependent deacetylases (sirtuins). The mitochondrial redox status modulates SIRT1/6 in the nucleus and SIRT3/4/5 in mitochondria and couples energy status to histone and non-histone deacetylation, leading to large-scale shifts in DNA methylation patterns and transcription programs[139]. All of these are examples of pathways in which mitochondria play a major role. There are many more, and certainly many that have not yet been discovered.

1.6 The innate immune response

The ISG response is a central component of the innate immune system and provides a rapid and effective defense mechanism against viral infections and other pathogens[140]. This response is initiated when pathogen-associated molecular patterns (PAMPs), such as viral nucleic acids, are recognized and bound in the cytosol by the cyclic GMP-AMP synthase (cGAS)[141] which binds cytosolic DNA and catalyses the production of the secondary messenger cGAMP (cyclic GMP-AMP). cGAMP subsequently activates the ER-associated receptor STING (Stimulator of interferon genes), triggering its translocation to the Golgi apparatus. At the Golgi, STING recruits and activates TANK-binding kinase 1 (TBK1), which phosphorylates the transcription factor IRF3 (Interferon regulatory factor 3). Phosphorylated IRF3 then translocates to the nucleus and induces the expression of type I interferons[142]. Secreted type I interferons bind to interferon receptors on the cell surface, thereby activating the JAK-STAT signalling pathway: The Janus kinases JAK1 and TYK2 phosphorylate STAT1 and STAT2 (Signal transducer and activator of transcription 1/2), which together with IRF9 form the ISGF3 complex[143]. These complexes bind to specific DNA sequences in the nucleus, which in turn leads to the expression of interferon-stimulated genes (ISGs). The functions of ISGs are diverse: They inhibit virus replication, block the translation of viral proteins, promote apoptosis of infected cells, activate adaptive immune responses, and modulate cell proliferation and cell architecture. The ISG response is a complex network of genes that work together to put the cell into an antiviral state and prevent the spread of infection. Its activation can also be triggered by the release of Damage-Associated Molecular Patterns (DAMPS). DAMPS include various mitochondria derived molecules like mtDNA, mtRNA, cardiolipin or ROS[144]. For example, when mtDNA from the matrix enters the cytosol, it is recognized by cGAS as pathogenic foreign DNA due to its fewer methylated sites and high concentration of CpG motifs (resembles bacterial DNA according to the endosymbiotic theory). Recognition as “non-self-DNA” triggers an immune reaction and activates the innate immune response.

1.6.1 mtDNA escape routes

Usually, mtDNA is isolated from the cytoplasm and kept from inducing ISG within the double membraned mitochondrion. However, under stress conditions, its release can

be triggered via different mechanisms. Depending on the type of stress, different factors are involved in the release. The mPTP/VDAC route is activated when calcium homeostasis is disturbed or oxidative stress increases, resulting in the opening of the mPTP in the IM and mtDNA diffusion into the IMS[128,145]. Next, oligomerized VDAC pores allow mtDNA fragments to escape into the cytosol. When apoptosis is initiated, BAX/BAK are recruited to the OM and can form large macropores, also known as mitochondrial outer membrane permeabilization (MOMP). The IM herniates through these macropores, releasing the matrix contents, including mtDNA, into the cytosol[146]. mtDNA can escape into the cytosol when mitochondrial genome maintenance or membrane integrity is compromised, particularly in the context of defective mitochondrial quality control. Disruption of mtDNA packaging represents one of those triggers: Loss of TFAM has been shown to result in unprotected and fragmented mtDNA, which can be recognized by cGAS in the cytosol[147]. A similar phenomenon can be observed in *MGME1*$^{-/-}$ and *YME1L*$^{-/-}$ models, which induce nucleotide imbalance[54] resulting in unstable mtDNA fragments as a source for mtDNA release, although the exact mechanism of release is not yet known[148,149]. Altered mitochondrial dynamics also contribute to the mtDNA escape. Depletion of MFN 1/2 and OPA1 result in increased mitochondrial fragmentation and mtDNA release[150,151].

An additional release mechanism is provided by MDVs[152]. They carry damaged material including mtDNA and transport them to the lysosomes or peroxisomes or for disposal or to the plasma membrane. The final destination depends on the cargo of the vesicle. It was proposed that sorting nexin 9 (SNX9)-dependent MDVs lead to a cytosolic release of mtDNA, although it is not yet clear how the nucleic acid crosses the membrane of the vesicle[153]. In general, the release of mtDNA must be strictly regulated, otherwise, a chronic inflammatory response can be triggered in the cell[154].

1.7 FAM210A- a key regulator of mitochondrial homeostasis

FAM proteins (FAM = Family with sequence similarity) represent a group of proteins that have been named based on their sequence similarity and play a role in various biological processes. They are involved in the regulation of the cell cycle, signal transduction, metabolism, and organelle quality control. Some FAM proteins are particularly crucial for the function and integrity of mitochondria. These include the protein FAM210A. The nuclear-encoded enzyme features an N-terminal mitochondrial

targeting signal, a transmembrane helix, a C-terminal DUF1279 domain, and a coiled coil region, which are important for protein-protein interactions [155,156]. FAM210A is an integral inner membrane protein, with predicted membrane-spanning domains whereby the N-terminus is located in the IMS and the C-terminus is facing towards the mitochondrial matrix[155]. The multicellular and organism-conserved protein is primarily expressed in energy-intensive organs like heart, skeletal muscle and brown adipose tissue, which indicates its function in energy homeostasis[157]. Functionally, FAM210A intervenes at several junctures of mitochondrial quality control and metabolism. In various tissue-specific knockout models (heart, skeletal muscle, brown fat), the loss of FAM210A leads to disrupted cristae architecture, reduced mitochondrial density and size, decreased respiration and ATP production, as well as compensatory activation of mitophagy and stress response (ISR response)[155,158,159]. At the dynamic level, FAM210A indirectly modulates the balance between fusion and fission via OPA1 as it interacts with YME1L and promotes the degradation of OMA1[155]. Consequently, excessive OMA1 activity and pathological OPA1 cleavage are limited. In the absence of FAM210A, OMA1-mediated OPA1 processing predominates, leading to increased fragmentation and cristae loosening, particularly evident under stress conditions such as cold exposure or increased metabolic stress. In addition, FAM210A functions as a gateway between mitochondrial and cytosolic translation. In cardiac and skeletal muscle cells, FAM210A has been shown to interact with mitochondrial translation factors such as EF-Tu and ATAD3A, thereby influencing the efficiency of mitochondrial protein translation.[151,156] In skeletal muscle knockouts, a shift in the TCA cycle toward reductive fluxes, accumulation of acetyl-CoA, and hyperacetylation of ribosomal proteins have been described, triggering ribosomal disassembly and global translation defects[158]. This positions FAM210A as an integrator that couples intramitochondrial organization (cristae, OPA1 status), respiratory chain capacity, and proteostasis with cellular protein synthesis. Overall, these findings make FAM210A an important mitochondrial key factor whose dysfunction can promote muscle atrophy, cardiac dysfunction, and presumably other mitochondrial pathologies.

1.8 Aims of the thesis

Proper functioning and regulation of mitochondrial plasticity is essential for cellular homeostasis. All players involved must be strictly coordinated and functioning to provide an effective response to cellular demands and stress factors. Opa1 processing is linked to many physiological conditions, however the physiological relevance is still unclear. Prevalent protease deficient models (like Yme1l or Oma1 depletion) are difficult to interpret due to pleiotropic effects. We decided to investigate the necessity of Opa1 processing without removing the proteases. We questioned the role of individual isoforms *in vivo* and the need for Opa1 alternative mRNA splicing and processing. Finally, our aim was to find out the active role s-Opa1. Since the sequence and structure of s-Opa1 are highly conserved and all functional domains are located in the protein, we wanted to understand the mode of action of the cleaved protein.

To achieve our aims, we have planned the following steps:

- Characterization of pre-generated knock-in mouse models via CRISPR-Cas9-mediated genome editing of the Opa1 locus. With the model called *Opa1v1* we allowed the exclusive full-body expression of the Opa1 variant 1 to investigate the consequences of absence of the isoforms 5,7 and 8. Additionally this mouse line lacks exons 4b and 5b and thus is missing the Yme1l S2 cleavage site. This provided us insight in the importance of the Yme1l-dependent Opa1 processing. The additional pre-generated model *Opa1v1Δ4* lacks four amino acids at the S1 cleavage site resulting is loss of Oma1 cleavage. This ensures depleted Opa1 processing without deactivating the proteases. Aim of this thesis was to analyze both mouse models in detail to understand the importance of alternative Opa1 processing and splicing under basal conditions.

- Challenging *Opa1v1* and *Opa1v1Δ4* mouse models with mild and severe stress. We planned to expose the animals to metabolic and thermal stress through a high-fat diet (HFD) and cold shock (4°C). Additionally, we analyzed the role of Opa1 isoforms and processing in mitochondrial dysfunction conditions. For this purpose, we crossed *Opa1v1* and *Opa1v1Δ4* lines with a cardiac and skeletal muscle–specific depletion of cytochrome c oxidase assembly factor heme A:farnesyltransferase (*Cox10*$^{-/-}$) and analyzed the resulting effects.

- *In vitro* studies using MEFs generated from the mouse models. To gain more mechanistic insights, we generated MEFs with the same genetic background as the mice to discover more about the regulation of Opa1 splicing and processing. Our main focus was to analyze mitochondrial morphology and dynamics and to gain insights into stress-induced pathways. We aimed to discover role of s-Opa1 by performing rescue experiments and analyzing the active environment of the protein.

2 Results

2.1 Opa1 processing is dispensable in mouse development but is protective in mitochondrial cardiomyopathy (published article)

Science Advances, 2024

Sofia Ahola†, Lilli A. Pazurek†, Fiona Mayer, Philipp Lampe, Steffen Hermans, Lore Becker, Oana V Amarie, Helmut Fuchs, Valerie Gailus-Durner, Martin Hrabe de Angelis, Dietmar Riedel, Hendrik Nolte, Thomas Langer †these authors contributed equally to this work.

Author's Contribution

This thesis includes several experiments investigating the role of Opa1 processing *in vitro* and *in vivo* which were mostly published in this paper. Experimental designs and procedures were collaborative projects. An overview of the contributors is presented in Table 1.

Table 1: Contributions for the experiments presented in this thesis.

Experiment	Study design	Data collection	Data analysis	Manuscript preparation	Figure in manuscript
Ageing study	**LPW**	**LPW**	**LPW**	**LPW**	1D,F ; 3A
Dynamics assay	**LPW**	**LPW**	**LPW**	**LPW**	2E,F
Morphology *in vitro*	**LPW**	**LPW**	**LPW**	**LPW**	2G S 1H
Electron microscopy *in vitro*	**LPW**	**DR**	**LPW**	**LPW**	2J-K
Confocal imaging	**LPW**	**LPW**	**LPW**	**LPW**	2L-M
Cristae analysis	FM	FM	FM, **LPW**	FM, **LPW**	3G,H
Thermogenesis *in vivo*	FM	FM, **LPW**	FM, **LPW**	FM, **LPW**	4H-M
Opa1 expression level	**LPW**	**LPW**	**LPW**	**LPW**	S 1C
German mouse clinic	FM	GMC	GMC	SA, **LPW**	Figure S2

The initials mark contributors for the different projects and phases within the project that are presented in this thesis.

Lilli Pazurek-Weber (LPW), Fiona Mayer (FM), Sofia Ahola (SA), Dietmar Riedel (DR), German mouse clinic (GMC)

SCIENCE ADVANCES | RESEARCH ARTICLE

MOLECULAR BIOLOGY

Opa1 processing is dispensable in mouse development but is protective in mitochondrial cardiomyopathy

Sofia Ahola[1]†, Lilli A. Pazurek[1]†, Fiona Mayer[1], Philipp Lampe[1], Steffen Hermans[1], Lore Becker[2], Oana V Amarie[2], Helmut Fuchs[2], Valerie Gailus-Durner[2], Martin Hrabe de Angelis[2,3,4], Dietmar Riedel[5], Hendrik Nolte[1], Thomas Langer[1,6]*

Mitochondrial fusion and fission accompany adaptive responses to stress and altered metabolic demands. Inner membrane fusion and cristae morphogenesis depends on optic atrophy 1 (Opa1), which is expressed in different isoforms and is cleaved from a membrane-bound, long to a soluble, short form. Here, we have analyzed the physiological role of Opa1 isoforms and Opa1 processing by generating mouse lines expressing only one cleavable Opa1 isoform or a non-cleavable variant thereof. Our results show that expression of a single cleavable or non-cleavable Opa1 isoform preserves embryonic development and the health of adult mice. Opa1 processing is dispensable under metabolic and thermal stress but prolongs life span and protects against mitochondrial cardiomyopathy in OXPHOS-deficient *Cox10*$^{-/-}$ mice. Mechanistically, loss of Opa1 processing disturbs the balance between mitochondrial biogenesis and mitophagy, suppressing cardiac hypertrophic growth in *Cox10*$^{-/-}$ hearts. Our results highlight the critical regulatory role of Opa1 processing, mitochondrial dynamics, and metabolism for cardiac hypertrophy.

INTRODUCTION

Mitochondria are highly dynamic organelles that constantly fuse and divide. This dynamic behavior of mitochondria ensures mitochondrial inheritance, distribution, and quality control; allows metabolic adaptation of cells; and has been linked to cell death pathways (*1*, *2*). Defects in the mitochondrial fusion or fission machinery are associated with many pathologies, including different encephalomyopathies, cardiomyopathies, and optic atrophies (*3*, *4*).

The dynamin-like guanosine triphosphatase (GTPase) dominant optic atrophy 1 (Opa1) regulates mitochondrial inner membrane (IM) fusion and cristae morphogenesis. *OPA1* mutations cause autosomal dominant optic atrophy (ADOA) in humans, which is associated with the selective loss of retinal ganglion cells and blindness (*5*, *6*). Missense mutations in *OPA1* lead to multisystem disorders with a wide range of clinical manifestations (*7*). Numerous studies in mice have demonstrated the critical role of Opa1 in mitochondrial function. Impaired fusion and cristae morphogenesis in *Opa1*$^{-/-}$ mice results in embryonic lethality, while tissue-specific knockout models in energy-demanding tissues such as the brain, heart, and skeletal muscle are associated with respiratory defects and cause organ dysfunction and animal death (*8*–*14*). In contrast, liver-specific loss of Opa1 impairs cristae morphogenesis but does not affect organ function due to a mitohormetic stress response (*15*), which protects against drug-induced liver injury and nonalcoholic fatty liver disease (*16*). On the other hand, a protective effect of mild overexpression of Opa1 has been observed in mouse models for oxidative phosphorylation (OXPHOS) dysfunction (*12*, *17*, *18*), demonstrating the importance of Opa1 levels for physiological functions.

Opa1 function is tightly regulated at the protein level. Following import of nuclear-encoded Opa1 into mitochondria and removal of the mitochondrial targeting sequence, the maintenance of normal mitochondrial morphology depends on the proteolytic processing of Opa1 and the balanced accumulation of membrane-bound, uncleaved (long, l-Opa1) and soluble, cleaved (short, s-Opa1) forms (*19*). The IM proteases overlapping activity with m-AAA protease 1 (Oma1) and Yeast mitochondrial escape protein 1-like (Yme1l) cleave l-Opa1 at neighboring proteolytic sites S1 and S2, respectively, to generate s-Opa1 forms (*20*–*25*). Yme1l also mediates Opa1 turnover, thereby limiting the overall Opa1 accumulation (*26*). Studies in cultured cells and reconstituted systems have shown that l-Opa1 is essential and, together with cardiolipin, sufficient to mediate membrane fusion (*20*, *27*, *28*), which, however, is further stimulated in the presence of s-Opa1 (*28*, *29*). Under basal conditions, both Yme1l and Oma1 mediate limited processing of Opa1 (*23*, *25*). Mitochondrial stress, such as dissipation of the membrane potential, oxidative, or thermal stress, further activates Oma1, which converts l-Opa1 into s-Opa1 and promotes mitochondrial fragmentation (*21*, *24*, *30*). Similar to l-Opa1, s-Opa1 is sufficient to maintain cristae morphogenesis and respiration when expressed in *Opa1*$^{-/-}$ mouse embryonic fibroblasts (MEFs) (*27*, *31*). s-Opa1 associates with the membrane, induces tubulation by forming helical assemblies, and compacts the membrane via dimerization of the GTPase domain upon guanosine 5′-triphosphate binding (*32*, *33*). Accordingly, l-Opa1 has been proposed to mark the sites for fusion, which may explain the increased fusion efficiency with balanced accumulation of l- and s-Opa1 (*29*, *32*).

Opa1 is expressed in eight different mRNA isoforms in humans and four in mice, which are produced by alternative splicing and which are differentially expressed in different organs (*34*). The *Opa1* isoforms differ only in the presence of exons 4, 4b, and 5b, the latter encoding the proteolytic processing site S2 for Yme1l (Fig. 1A). In contrast, all expressed human and mouse splice variants contain the

[1]Max Planck Institute for Biology of Ageing, Cologne, Germany. [2]Institute of Experimental Genetics, German Mouse Clinic, Helmholtz Zentrum München, German Research Center for Environmental Health (GmbH), Neuherberg, Germany. [3]Experimental Genetics, TUM School of Life Sciences, Technische Universität München, Freising, Germany. [4]German Center for Diabetes Research (DZD), 85764 Neuherberg. [5]Max Planck Institute for Multidisciplinary Sciences, Göttingen, Germany. [6]Cologne Excellence Cluster on Cellular Stress Responses in Aging-Associated Diseases (CECAD), University of Cologne, Cologne, Germany.
*Corresponding author. Email: tlanger@age.mpg.de
†These authors contributed equally to this work.

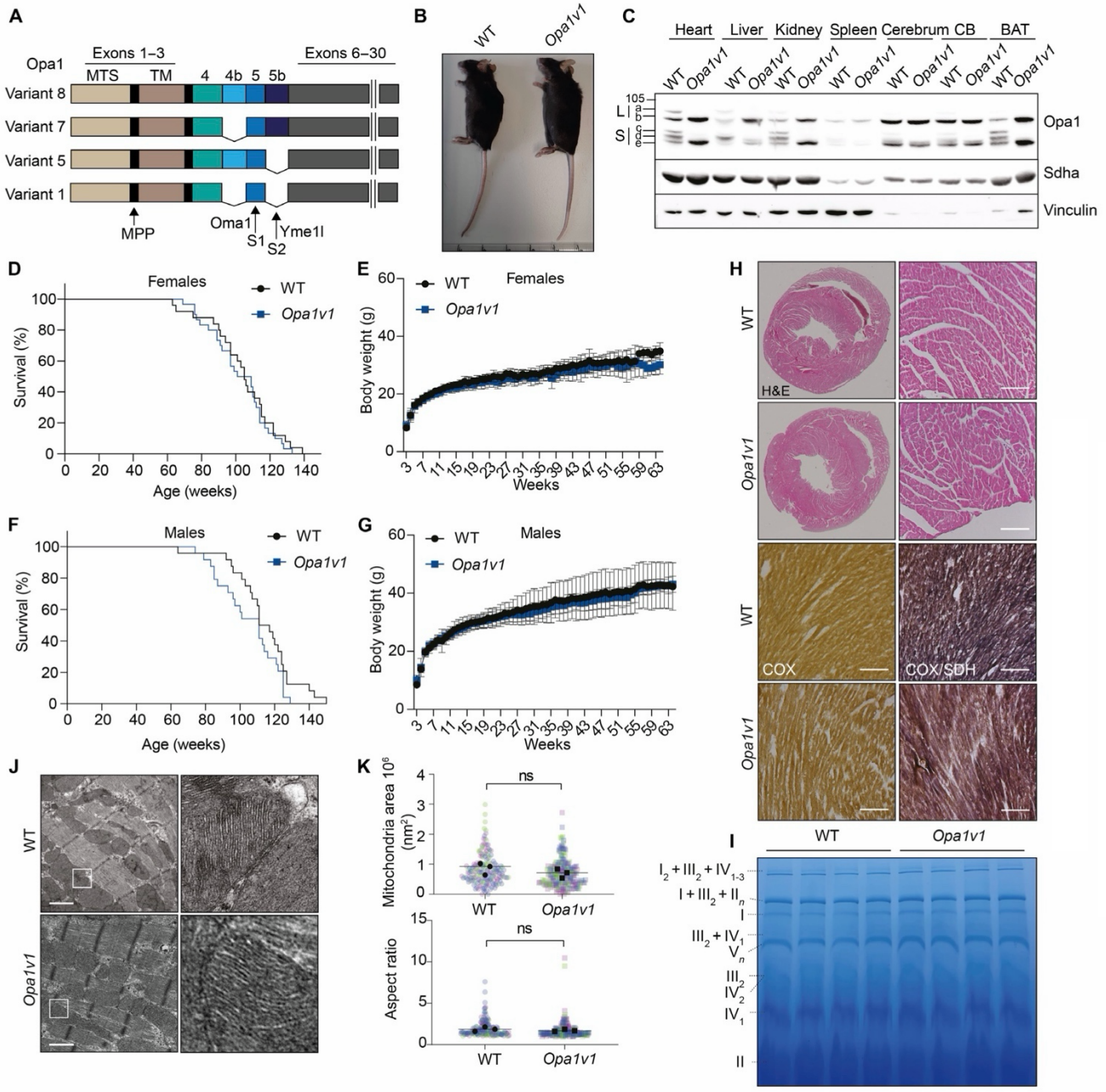

Fig. 1. Expression of only Opa1 V1 sustains mouse development and mitochondrial structure. (**A**) Illustration of *Opa1* gene variants showing all four isoforms expressed in mice. Positions of processing sites S1 and S2 for Oma1 and Yme1l proteases, respectively, are indicated. (**B**) Twelve-week-old knock-in mice expressing only *Opa1v1* develop normally and show no obvious phenotype. (**C**) V1 expression in tissues of wild-type (WT) and *Opa1v1* mice. (**D** to **G**) *Opa1v1* female and male mice have a normal life span (WT, male, $n = 26$; WT, female, $n = 25$; *Opa1v1*, male, $n = 25$; *Opa1v1*, female, $n = 30$) and show similar body weight gain as their WT littermates ($n = 10$). (**H**) Normal heart structure and normal COX/SDH activity in 12-week-old WT and *Opa1v1* mice, as shown by hematoxylin and eosin (H&E) or COX/SDH staining, respectively. Scale bar, 200 μm. (**I**) Blue native (BN)–polyacrylamide gel electrophoresis (PAGE) from 56-week-old WT and *Opa1v1* heart mitochondria showing RCC and super complexes ($n = 4$). (**J**) Representative transmission electron microscopy (TEM) images from 12-week-old WT and *Opa1v1* heart tissue showing normal mitochondrial morphology and cristae structure. Scale bars, 1 μm. (**K**) Mitochondrial area and aspect ratio in hearts ($n = 3$ mice; mitochondria WT, $n = 181$; and *Opa1v1*, $n = 231$ in total). MTS, mitochondrial targeting sequence; TM, transmembrane domain; MPP, Mitochondrial-processing peptidase processing site; CB, cerebellum; BAT, brown adipose tissue; ns, nonsignificant.

Oma1 processing site S1, pointing to important functions of Oma1-mediated Opa1 processing.

The role of Opa1 processing and s-Opa1 in vivo has been mainly studied using Oma1- or Yme1l-deficient mouse models (*35*–*39*). However, the identification of an increasing number of substrates of both peptidases in addition to Opa1 has complicated the interpretation of these models (*26*, *40*–*44*). The physiological role of the different splice variants in vivo is now unknown. Selective silencing of the three isoform-specific exons in HeLa cells revealed different effects on mitochondrial morphology and bioenergetics, suggesting isoform-specific functions (*45*). Similarly, only co-expression of two isoforms of Opa1 in *Opa1*$^{-/-}$ MEFs allowed complete recovery of the mitochondrial morphology (*31*).

To analyze the physiological role of Opa1 processing and different *Opa1* mRNA isoforms, we generated two knock-in mouse models by CRISPR-Cas9–mediated genome editing of the *Opa1* locus. One mouse line expresses exclusively Opa1 variant 1 (V1), which lacks exons 4b and 5b and thus only contains the Oma1 processing site S1 (*Opa1v1*). The second mouse line expresses a mutant form of Opa1 V1, which lacks four amino acids at the S1 cleavage site inhibiting Oma1 cleavage (*Opa1v1Δ4*). These *Opa1* mouse models provide insight into the role Opa1 splice variants and Opa1 processing in vivo.

RESULTS

Mouse embryonic development and viability are maintained by expression of only Opa1 V1

Four Opa1 isoforms are expressed in mice, which differ in the presence or absence of cleavage sites for Oma1 (S1 within exon 5) and for Yme1l (S2 within exon 5b) (Fig. 1A). To allow the analysis of Oma1-mediated Opa1 processing without the potential confounding effects of Yme1l cleavage, we used CRISPR-mediated genome editing to generate transgenic *Opa1* knock-in mice that exclusively express Opa1 V1 (fig. S1A and table S1). V1 harbors the Oma1 cleavage site S1 at arginine 194 but lacks exons 4b and 5b and the Yme1l cleavage sites S3 and S2, respectively (*46*). To exclude potential off-target effects on the phenotype, we bred two genetically independent lines from F_O heterozygous pups and backcrossed them for >10 generations. Targeted locus amplification (TLA) sequencing confirmed the integration of the repair nucleotide into the *Opa1* locus on chromosome 16 and did not reveal off-target integrations.

While deletion of *Opa1* in mice is embryonic lethal (*9*, *10*), homozygous *Opa1v1* mice were born healthy at the expected Mendelian ratio (fig. S1B) and showed no apparent phenotype (Fig. 1B). *Opa1v1* was ubiquitously expressed in various tissues of the mice. As expected, we detected only one l-Opa1 form (non-cleaved, mature V1) and one s-Opa1 form (corresponding to Opa1 form e generated by Oma1-mediated processing of V1) (Fig. 1C). Total Opa1 levels were similar in WT and *Opa1v1* hearts (fig. S1C). Opa1 form d generated by Yme1l cleavage was not produced in any tissue (Fig. 1C). Similar Opa1 forms accumulated in wild-type (WT) and *Opa1v1* brain tissues, which is consistent with the predominant expression of Opa1 isoform 1 in the mouse brain (*47*). However, different Opa1 forms accumulated in *Opa1v1* mice compared to those in WT mice in tissues that express several Opa1 isoforms, such as the heart, brown adipose tissue (BAT), and kidney (Fig. 1C). In the kidney and the brain, we detected low amounts of a small from of Opa1, which may represent an aberrant proteolytic cleavage in the absence of S2 and S3 or another posttranslational modification (Fig. 1C). Survival and body weight of both of the sexes were similar in WT and *Opa1v1* littermates (Fig. 1, D to G). Heart ultrastructure was unaffected in *Opa1v1* mice (Fig. 1H), and histological analysis of cardiac tissue did not reveal any OXPHOS deficiency (Fig. 1H). Blue native (BN)–polyacrylamide gel electrophoresis (PAGE) from cardiac mitochondria showed normal respiratory chain complex (RCC) assembly (Fig. 1I). We observed normal mitochondrial size and an unaltered cristae structure by transmission electron microscopy (TEM) (Fig. 1, J and K). These results demonstrate that the expression of V1 is sufficient for normal mouse development and maintains normal mitochondrial morphology and cristae morphogenesis in the heart in vivo.

Cleavage site mutations inhibit Oma1-mediated V1 processing

To investigate the physiological role of Opa1 processing in vivo, we aimed to generate mice expressing only a non-cleavable form of V1. To identify mutations in V1 that would disrupt Oma1 cleavage, we used a cell-free expression system to reconstitute Oma1 and proteolytically inactive Oma1^{E324Q}, which has a point mutation in the proteolytic site, in liposomes in vitro (Fig. 2A). After co-expression of V1, we observed cleavage of V1 to Opa1 form e by Oma1 but not by Oma1^{E324Q} (Fig. 2B). We then deleted 2, 4, or 10 amino acids at the Oma1 processing site between Arg^{194} and Ala^{195} of V1 and monitored its cleavage by Oma1 in vitro. Deletion of Arg^{194} and Ala^{195} was sufficient to completely inhibit V1 cleavage (Fig. 2C). Similarly, when expressed in WT or *Oma1*$^{-/-}$ MEFs, we did not observe specific proteolytic processing of V1 variants lacking two or more amino acids at S1 (fig. S1D). Deletion of only Arg^{194} alone did not inhibit Oma1-mediated cleavage of V1 (fig. S1D). As we observed unspecific degradation of V1 variants missing one or two amino acids in these experiments, we focused on V1 missing four amino acids (V1Δ4). V1Δ4 was protected from proteolytic processing by Oma1, even upon dissipation of the mitochondrial membrane potential ($\Delta\Psi_m$), which is known to activate Oma1 (Fig. 2D) (*21*). The steady-state level of V1Δ4 was decreased in depolarized mitochondria, likely reflecting increased turnover by Yme1l.

To test whether V1Δ4 is functional and mediates mitochondrial fusion, we used MEFs expressing the mitochondrially targeted photoconvertible red fluorescent protein mito-mEosEM561, V1, and V1Δ4 from the genomic *Opa1* locus. Mito-mEosEM561 was locally activated, and the distribution of activated mEosEM was monitored by time-lapse confocal imaging (Fig. 2E). We observed similar fusion rates in V1 and V1Δ4 expressing cells as in the WT, indicating that V1 as well as non-cleavable V1Δ4 preserves mitochondrial fusion (Fig. 2F). Consistently, V1Δ4 cells contained tubular mitochondria with largely normal cristae morphology, although mitochondria were more clustered around the nucleus (Fig. 2G). Depolarization of mitochondria caused mitochondrial fragmentation in WT and V1Δ4 cells (Fig. 2, H and I). To exclude that the mitochondrial clustering is caused by cell shrinkage, we analyzed the cell diameter by fluorescence activated cell sorting (FACS) and found similar sizes of WT and V1Δ4 cells (fig. S1H). V1Δ4 cells showed slightly enlarged mitochondria, when analyzing the mitochondrial ultrastructure by TEM (Fig. 2, J and K). These observations are consistent with previous studies demonstrating that l-Opa1 is sufficient to largely maintain mitochondrial fusion, which, however, can be stimulated by s-Opa1 (*28*, *29*). TEM images from V1Δ4

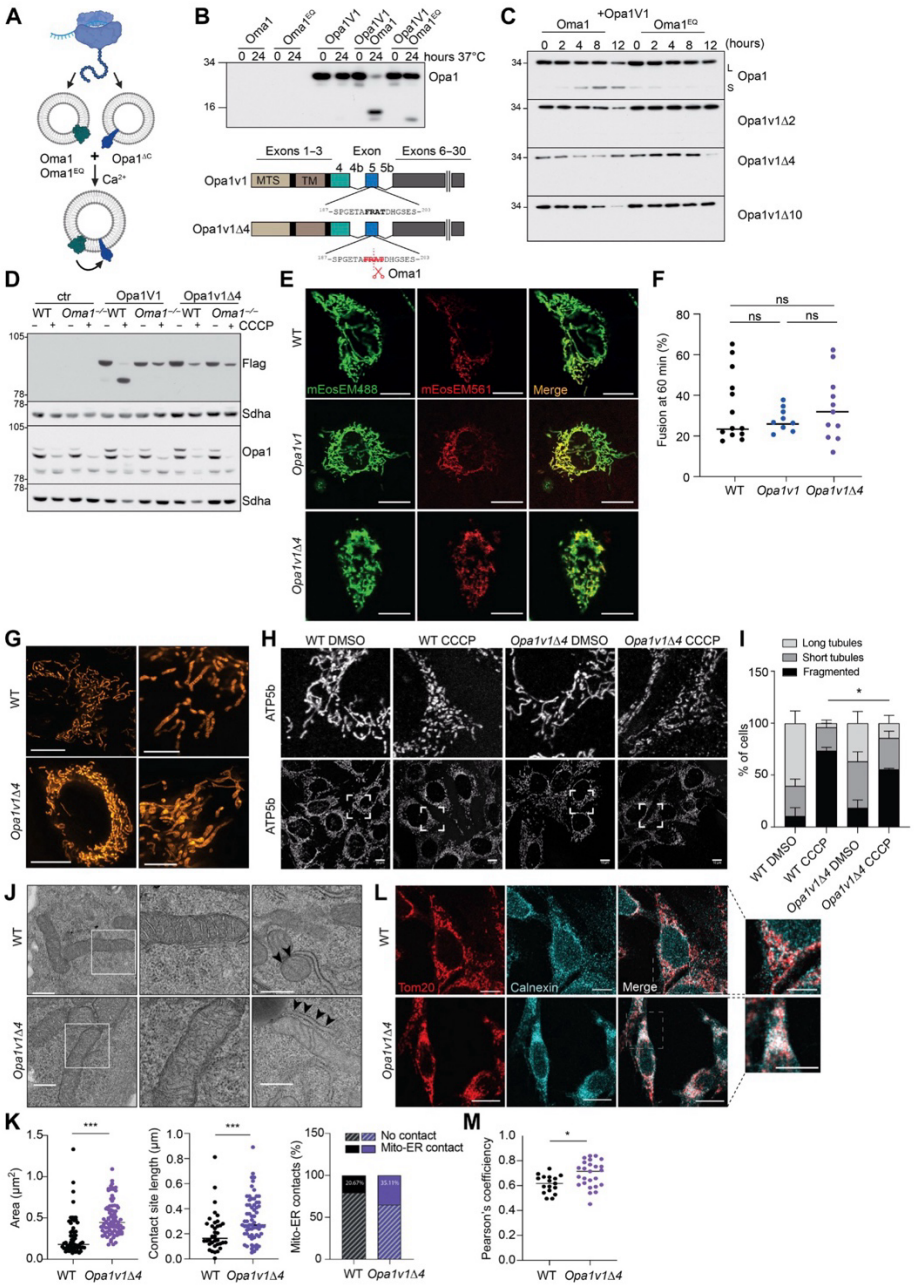

Fig. 2. Non-cleavable Opa1 V1 supports mitochondrial fusion in vitro. (**A**) Cell-free assay to monitor Opa1 cleavage by Oma1. Scheme was created with BioRender.com. (**B**) C-terminally truncated Opa1 variant V1 (V1ΔC), Oma1, or Oma1^{E324Q} was synthesized in a cell-free system with liposomes and monitored by SDS-PAGE. V1ΔC is processed by Oma1 but not Oma1^{E324Q} in vitro. (**C**) Deletion of 2 (Δ2), 4 (Δ4), or 10 (Δ10) amino acids at S1 from Opa1v1ΔC blocks Oma1-mediated processing. (**D**) Opa1 processing in WT and *Oma1*$^{-/-}$ MEFs transiently expressing Flag-tagged Opa1 variants ± CCCP (2 hours, 20 μM). (**E**) Representative images of WT, *Opa1v1*, and *Opa1v1Δ4* MEFs transiently expressing mito-mEosEM488 and mito-mEosEM561 60 min after photoactivation. Scale bars, 10 μm. (**F**) Quantification of fused mitochondrial area in WT ($n = 13$), *Opa1v1* ($n = 9$), and *Opa1v1Δ4* ($n = 11$) cells. (**G**) Mitochondrial morphology in WT and *Opa1v1Δ4* MEFs. Mitochondria stained with MitoOrange and analyzed by STED nanoscopy. Scale bars, 10 μm and (zoomed in) 5 μm. (**H** and **I**) Immunofluorescence analyses of WT and *Opa1v1Δ4* MEFs with ATP5b-specific antibodies ± CCCP (2 hours, 20 μM). Scale bars, 10 μm. Mitochondria of at least 100 cells were quantified per condition in $n = 3$ independent biological replicates and categorized in long tubules, short tubules, and fragmented. *$P < 0.05$ [two-way analysis of variance (ANOVA)]. (**J** and **K**) Mitochondrial ultrastructure in WT and *Opa1v1Δ4* MEFs analyzed by TEM. Scale bars, 500 nm. Mitochondrial size quantification (three independent experiments; mitochondria WT, $n = 122$; and *Opa1v1Δ4*, $n = 214$ in total) and mitochondria-ER contact sites (three independent experiments; WT, $n = 179$; and *Opa1v1Δ4*, $n = 188$ total contact sites), ***$P < 0.001$ (unpaired *t* test). (**L** and **M**) Immunofluorescence analyses of WT and *Opa1v1Δ4* MEFs with Tom20- and Calnexin-specific antibodies. Colocalization of ER and mitochondria indicated by white color is more prominent in *Opa1v1Δ4* MEFs (inset). Scale bars, 10 μm (inset, 20 μm). *$P < 0.05$.

expressing cells showed increased endoplasmic reticulum (ER)–mitochondrial contact sites (Fig. 2, J and K). ER has been shown to regulate mitochondrial dynamics by marking and possibly constricting the fission sites (*48*). Co-staining of mitochondria and ER showed increased co-localization in V1Δ4 cells compared to that in WT cells (Fig. 2, L and M). Together, loss of Opa1 processing mildly impairs mitochondrial distribution and prolongs ER-mitochondrial contact sites.

Opa1 processing is dispensable for normal mouse development and health

To analyze the role of Opa1 processing and s-Opa1 in vivo, we generated *Opa1v1Δ4* mice using a strategy similar to that used to generate *Opa1v1* mice but with a repair oligonucleotide encoding V1Δ4 (fig. S1F). We detected no off-target integration by TLA sequencing in an *Opa1v1Δ4* pup born after pronuclear injection of guide RNAs (gRNAs) and Cas9. Heterozygous intercrosses produced homozygous *Opa1v1Δ4* animals at the expected Mendelian ratio (fig. S1G). *Opa1v1Δ4* mice developed normally, had a normal life span, gained body weight as WT mice, and showed no apparent phenotype (Fig. 3, A to C). We next analyzed Opa1 processing in different tissues from 12-week-old WT and *Opa1v1Δ4* animals. Oma1-mediated Opa1 processing was severely impaired in all tissues and almost completely blunted in the heart, liver, and BAT, which normally express variants 1 and 7 that can be processed by Yme1l (Fig. 3D) (*47*). Low levels of a short form of Opa1 were detected in the brain and the kidney (Fig. 3D), which may reflect increased Oma1 activity in these tissues. Therefore, we focused our further experiments on the heart. Heart size and structure and mitochondrial OXPHOS function appeared normal in *Opa1v1Δ4* animals (Fig. 3, E and F, and fig. S1E). Analysis of heart tissue by TEM revealed normal mitochondrial size and ultrastructure in *Opa1v1Δ4* mice, with mild reduction in cristae number in *Opa1v1Δ4* hearts, suggesting that s-Opa1 accumulation is dispensable for cristae morphogenesis in the heart in vivo (Fig. 3, G and H). Consistent with this, we have previously observed normal mitochondrial ultrastructure in mice lacking the Opa1 processing peptidases Oma1 and Yme1l in cardiomyocytes (*35*). We conclude from these experiments that V1Δ4 is sufficient to maintain normal development and animal health and that mitochondrial function and cristae formation in the heart is largely unaffected by the loss of s-Opa1 in vivo.

Mutations in the *OPA1* gene in humans most commonly lead to ADOA with loss of vision combined with neuromuscular multisystemic dysfunctions such as ataxia and peripheral neuropathy (*5*, *6*). To investigate whether *Opa1v1* or *Opa1v1Δ4* animals show sensory defects, muscle weakness, or motor dysfunction, we performed grip strength, rotarod, and hotplate tests on 1-year-old mice. *Opa1v1* females and *Opa1v1Δ4* males showed mild reduction in four paw grip strength tests (fig. S2, A and B), but all the other analyses showed no differences between the genotypes (fig. S2, C and D). To investigate the occurrence of optic atrophy in our *Opa1v1* or *Opa1v1Δ4* animals, we assessed their visual capabilities by virtual drum tests and evaluated the thickness of the retina and examined the retinal fundus, alongside examining the primary blood vessels within the retina. Our findings revealed no signs of optic atrophy in either of the mouse lines (fig. S2, E to I). Together, *Opa1v1* or *Opa1v1Δ4* mice do not exhibit the mitochondrial dysfunction typically associated with *OPA1* mutations observed in human cases, indicating a lack of the characteristic mitochondrial disease manifestations.

Opa1 processing is not essential under metabolic stress conditions

Oma1$^{-/-}$ mice show increased diet-induced obesity and altered thermogenesis during cold stress (*39*). To investigate the effect of impaired Oma1-mediated Opa1 processing under metabolic stress, we treated 1-year-old WT and *Opa1v1Δ4* mice with a high-fat diet (HFD) for 10 weeks. HFD feeding did not induce Opa1 processing in tissues of WT or *Opa1v1Δ4* animals (Fig. 4A), which showed a similar increase in body weight (Fig. 4B). Analysis of the body composition of the mice showed no difference in the fat mass after HFD (Fig. 4C), and also the running performance was not altered between the mouse strains (Fig. 4D). HFD induced the expected metabolic shift toward fatty acid utilization in both WT and *Opa1v1Δ4* mice (fig. S2J), demonstrating that Opa1 processing is not essential for increased β-oxidation upon HFD feeding. Similarly, animal movement, estimated heat production, or food consumption was consistent between the genotypes (fig. S2, K to M). HFD can lead to hypertrophic cardiomyopathy and mitochondrial dysfunction. After 10 weeks of HFD, heart weight was unaffected and TEM analysis showed no apparent differences in mitochondrial ultrastructure between WT and *Opa1v1Δ4* animals (Fig. 4, E to G).

Cold exposure induces dynamic remodeling of mitochondria and Opa1 has been shown to be essential for the proper function of BAT (*12*, *39*, *49*). To investigate whether Opa1 processing is essential in thermogenic adaptation, we studied 12-week-old WT and *Opa1v1Δ4* mice under cold stress. We found no notable differences in body temperature or body weight between the genotypes (Fig. 4, H and I). Cold stress did not affect Opa1 levels in *Opa1v1Δ4* BAT, although there was a reduction in total Opa1 levels in WT BAT as observed previously (Fig. 4K) (*39*). To further analyze the thermogenic response, we measured mRNA levels of uncoupling protein 1 (*Ucp1*), which regulates mitochondrial heat production, and of the transcriptional co-activator Peroxisome proliferator-activated receptor gamma coactivator 1-alpha (*Pgc1α*) but did not observe significant differences between the mouse strains (Fig. 4L). Furthermore, cold-induced fatty acid depletion from the liver and BAT, as assessed by Oil Red O staining, was similar in WT and *Opa1v1Δ4* mice (Fig. 4M). We conclude from these experiments that balanced Opa1 processing is not essential under metabolic stress conditions such as HFD or cold stress.

Opa1 processing has a protective role under severe OXPHOS stress

Oma1-mediated DAP3 binding cell death enhancer 1 (Dele1) processing elicits the mitochondrial integrated stress response (ISR^{mt}) (*43*, *44*), which protects OXPHOS-deficient hearts against ferroptosis (*50*). As OXPHOS deficiency also induces Opa1 processing by Oma1 in vivo, we investigated the role of Opa1 processing in cardiomyopathy associated with OXPHOS dysfunction. We used cardiac and skeletal muscle–specific cytochrome c oxidase assembly factor heme A:farnesyltransferase (*Cox10*$^{-/-}$)–deficient mice as a model for mitochondrial cardiomyopathy. *Cox10* encodes a heme A–farnesyltransferase, which is required for the assembly of the cytochrome c oxidase complex (*51*). Accordingly, loss of Cox10 in the heart leads to OXPHOS deficiency and early-onset dilated cardiomyopathy (*50*). Breeding of *Cox10*$^{-/-}$ mice with *Opa1v1* and *Opa1v1Δ4* mice revealed marked differences in the life span of the mice: Whereas the life span of *Cox10*$^{-/-}$*Opa1v1* mice was identical to that of *Cox10*$^{-/-}$ animals (median, 32 days), *Cox10*$^{-/-}$*Opa1v1Δ4* mice had a strongly reduced life span (median,

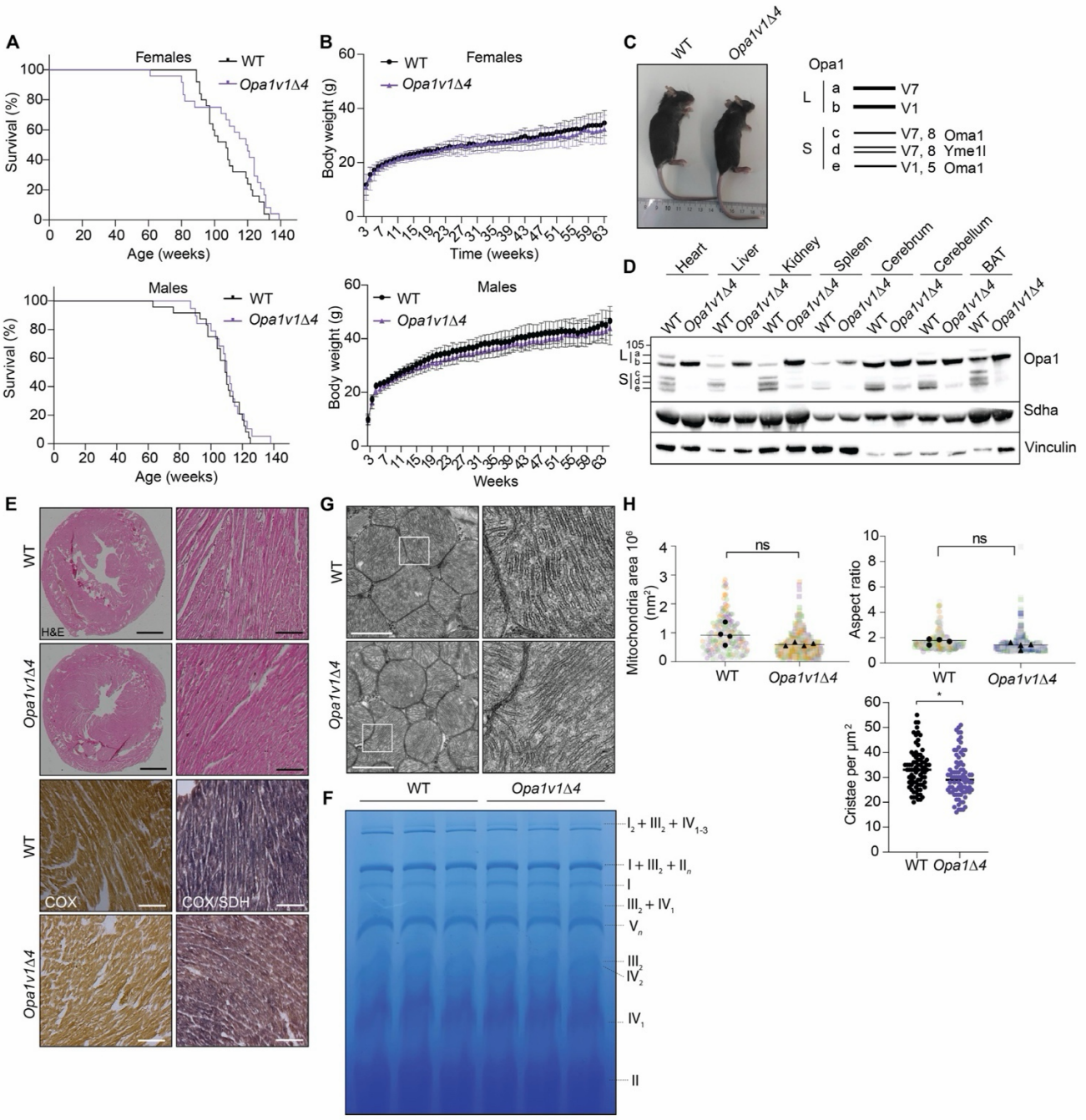

Fig. 3. Expression of V1Δ4 allows normal mouse development and preserves mitochondrial structure in vivo. (**A**) Life span of WT and *Opa1v1Δ4* mice (WT, male, $n = 25$; WT, female, $n = 30$; *Opa1v1Δ4*, male, $n = 24$; and *Opa1vΔ41*, female, $n = 30$). (**B**) Body weight gain of WT ($n = 10$) and *Opa1v1Δ4* mice ($n = 10$) mice. (**C**) Normal development of *Opa1v1Δ4* mice. (**D**) Opa1v1Δ4 is expressed throughout mouse tissues and mostly accumulates as mature, non-cleaved l-Opa1. Steady-state levels of succinate dehydrogenase (SDH) subunit A (Sdha) and vinculin were monitored as controls. (**E**) Normal heart structure and normal COX/SDH activity in 12-week-old WT and *Opa1v1Δ4* mice, as shown by H&E or COX/SDH staining, respectively. Scale bars, 200 µm. (**F**) BN-PAGE from 56-week-old WT and *Opa1v1Δ4* heart mitochondria showing RCC and respiratory supercomplexes ($n = 3$). (**G**) Representative TEM images from 12-week-old WT and *Opa1v1Δ4* heart tissue showing normal mitochondrial morphology and cristae structure. Scale bars, 100 nm. (**H**) Quantification of mitochondrial area and aspect ratio in hearts ($n = 3$ mice; mitochondria WT, $n = 247$; and *Opa1v1*, $n = 405$ in total; measurements from different mice are color-coded). Cristae density was calculated for 80 mitochondria from each $n = 3$ animals in WT and *Opa1v1Δ4*. The number of cristae was normalized to the mitochondrial area.

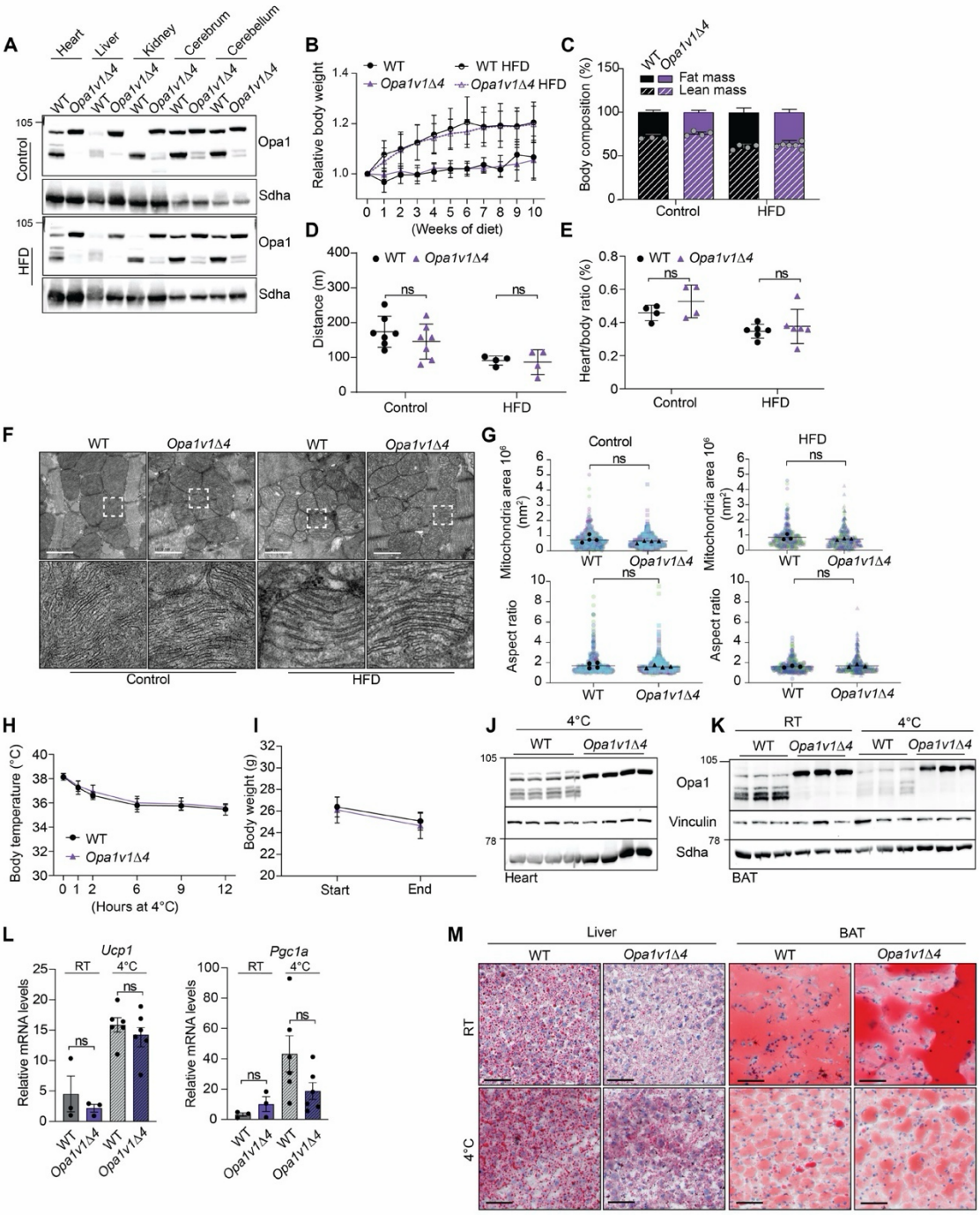

Fig. 4. Opa1 processing is not essential upon HFD feeding or cold exposure of mice. (**A**) Feeding of 54-week-old male mice for 10 weeks with a high-fat diet (HFD) did not induce Opa1 processing in various tissues. (**B**) HFD causes similar body weight gain in WT and *Opa1v1Δ4* mice (WT, $n = 6$; *Opa1v1Δ4*, $n = 6$; WT HFD, $n = 4$; and *Opa1v1Δ4* HFD, $n = 5$). (**C**) HFD increased fat mass similarly in WT and *Opa1v1Δ4* animals (male mice, $n = 3$ to 4 in the control diet and $n = 4$ to 6 in HFD). (**D**) WT and *Opa1v1Δ4* mice performed similarly in treadmill analysis (male mice, $n = 7$ in the control diet and $n = 4$ in HFD). (**E**) Heart/body weight ratio was similar in WT and *Opa1v1Δ4* mice on both diets (standard diet, $n = 4$; and HFD, $n = 6$). (**F** and **G**) HFD did not affect mitochondrial ultrastructure in the heart as shown by TEM analysis: Four mice were analyzed on control diet ($n = 529$ WT and $n = 658$ *Opa1v1Δ4* mitochondria); four WT mice on HFD ($n = 458$ mitochondria) and three *Opa1v1Δ4* mice on HFD ($n = 408$ mitochondria). Scale bars, 1 μm. (**H** and **I**). Rectal body temperature during 12 hours of cold exposure (4°C) for 12-week-old male mice and body weight before and after 12 hours at 4°C (WT, $n = 7$; and *Opa1v1Δ4*, $n = 5$). (**J** and **K**) Cold exposure did not increase Opa1 processing in the heart or BAT ($n = 3$ to 4). (**L**) Uncoupling protein 1 (*Ucp1*) and *Pgc1α* mRNA levels were similar in BAT of WT and *Opa1v1Δ4* mice ($n = 3$ to 6). (**M**) Oil Red O staining from the liver and BAT. Cold exposure decreased the fat deposits in BAT similarly in WT and *Opa1v1Δ4* mice ($n = 3$). Scale bars, 50 μm. RT, room temperature.

19 days) (Fig. 5, A and B). *Cox10*$^{-/-}$*Opa1v1Δ4* mice developed normally and were indistinguishable from their littermates until the age of ~2 weeks when pups became less active, had a hunched posture, and died suddenly within 24 hours. As previously reported (*50*), loss of Cox10 in cardiomyocytes induced Opa1 processing by Oma1 (Fig. 5C). Processing of variant 7 generates Opa1 form c, whereas Oma1-mediated cleavage of V1 leads to the formation of Opa1 form e. Accordingly, Opa1v1 mice accumulate only form b (corresponding to the non-cleaved form of V1) and form e generated by Oma1 (Fig. 5C). V1 processing and the level of Opa1 form e were increased in *Cox10*$^{-/-}$*Opa1v1* hearts. In contrast, V1Δ4 stably accumulated even in OXPHOS deficiency, although formation of minute amounts of s-Opa1 cannot be excluded (Fig. 5C). Opa1 protein levels were modestly decreased, suggesting increased degradation of V1Δ4 during OXPHOS stress. Similarly, Oma1 accumulated at lower levels in *Cox10*$^{-/-}$ hearts, likely reflecting autocatalytic turnover of Oma1 under OXPHOS stress (Fig. 5C) (*21*).

Loss of Cox10 in the heart results in cardiac hypertrophy (Fig. 5, D to F) (*50*). The heart/body weight ratio of *Cox10*$^{-/-}$*Opa1v1* mice was indistinguishable from that of *Cox10*$^{-/-}$ animals (Fig. 5D). However, the hypertrophic growth of *Cox10*$^{-/-}$*Opa1v1Δ4* hearts was significantly reduced when compared to those in *Cox10*$^{-/-}$ animals (Fig. 5, D to F). These observations indicate that V1 is functional and that Oma1-mediated Opa1 processing is required for cardiac hypertrophy induced by OXPHOS deficiency. Notably, impaired Opa1 processing did not affect Oma1- and Dele1-dependent ISR^{mt}, which protects OXPHOS-deficient cardiomyocytes from ferroptosis (*50*). We observed similar ISR^{mt} activation, similar levels of Gpx4, and a slight accumulation of lipid peroxides in *Cox10*$^{-/-}$ and *Cox10*$^{-/-}$*Opa1v1Δ4* hearts (fig. S3, A to E). Thus, the requirement of Oma1-mediated Opa1 processing for cardiac hypertrophy is independent of mitochondrial stress signaling.

Loss of Opa1 processing in *Cox10*$^{-/-}$ mice deregulates autophagy

Although cardiac hypertrophy was reduced, analysis of *Cox10*$^{-/-}$*Opa1v1Δ4* hearts by fluorescence and electron microscopy revealed severely disrupted cardiac tissue (Fig. 5, F and H, and fig. S3F) and enlarged mitochondria (Fig. 5G). We observed large vacuolar, possibly autolysosomal structures, reminiscent of our earlier observations in *Cox10*$^{-/-}$*Oma1*$^{-/-}$ hearts (Fig. 5, G and H) (*50*). OXPHOS deficiencies were previously found to impair lysosomal functions via diverse mechanisms (*52*–*54*), which may interfere with autophagy. Consistently, lipidated microtubule-associated protein 1A/1B light chain 3 (LC3II), which accumulates in lysosome-targeted membranes and drives the autophagosome maturation, was significantly increased in *Cox10*$^{-/-}$*Opa1v1Δ4* hearts (Fig. 5, I and J). We also observed accumulation of the autophagy receptor sequestosome 1 (p62) in heart lysates by immunoblotting (Fig. 5, I and J) and by immunohistochemical staining of *Cox10*$^{-/-}$ and *Cox10*$^{-/-}$*Opa1V1Δ4* hearts (fig. S3, G and H), pointing to an overall increased autophagic flux or stalled autophagy, which appeared further aggravated in *Cox10*$^{-/-}$*Opa1v1Δ4* hearts compared to that in *Cox10*$^{-/-}$ hearts. LC3 lipidation was similar in *Cox10*$^{-/-}$ and *Cox10*$^{-/-}$*Opa1V1* hearts, highlighting the role of the Opa1 processing (fig. S3I). In agreement with autophagy inhibition, phosphorylation of mTORC1 substrates, the ribosomal protein S6 and the eukaryotic initiation factor 4E binding protein 1 (4E-BP1), were increased in hearts lacking Cox10 (Fig. 5I). To assess how impaired Opa1 processing affects the autophagic flux, we isolated MEFs from WT, *Cox10*$^{-/-}$, *Opa1v1Δ4*, and *Cox10*$^{-/-}$*Opa1v1Δ4* mice. Similar to cardiomyocytes in vivo, loss of Cox10 induces Opa1 processing in MEFs, which was inhibited in cells harboring V1Δ4 (fig. S3J). Inhibition of autophagosome fusion with chloroquinone caused accumulation of LC3 in WT and *Cox10*$^{-/-}$ MEFs as expected (fig. S3K). In contrast, LC3 lipidation was inhibited in *Opa1v1Δ4* and *Cox10*$^{-/-}$*Opa1v1Δ4* MEFs (fig. S3K). These results indicate that suppression of Opa1 processing in Cox10-deficient cells expressing Opa1v1Δ4 impairs autophagy in vivo and in vitro, although inhibition of this process occurs apparently at an earlier stage in vitro. Thus, autophagic deficiencies may limit the removal of dysfunctional mitochondria and aggravate consequences of cardiac OXPHOS deficiency in *Cox10*$^{-/-}$*Opa1v1Δ4* mice.

Cox10$^{-/-}$ and *Cox10*$^{-/-}$*Opa1v1Δ4* hearts show hypertrophic gene expression

To better understand the absence of hypertrophic growth of *Cox10*$^{-/-}$*Opa1V1Δ4* hearts, we performed an RNA sequencing (RNA-seq) analysis and examined the expression of genes characteristic of cardiac hypertrophy (*55*). Notably, loss of Opa1 processing in *Cox10*$^{-/-}$ hearts did not significantly affect hypertrophic gene expression (Fig. 6A). Hypertrophic signature genes were up-regulated relative to WT in the hearts of both *Cox10*$^{-/-}$ and *Cox10*$^{-/-}$*Opa1v1Δ4* mice, although we did not observe cardiac hypertrophy in the latter mouse line (Fig. 5, D and E). Autophagy-related genes were similarly affected in *Cox10*$^{-/-}$ and *Cox10*$^{-/-}$*Opa1v1Δ4* mice (fig. S3L). Moreover, an ingenuity pathway analysis identified the up-regulation of similar cellular pathways and upstream regulatory genes, such as eukaryotic translation initiation factor 2 α kinase 3 (*Eif2ak3* encoding Dele1) (fig. S4, A and B). These data further corroborate that the ISR^{mt} does not depend on Opa1 processing (fig. S3, A and B). Comparison of gene expression profiles of *Cox10*$^{-/-}$*Opa1v1Δ4* and *Cox10*$^{-/-}$ hearts identified target genes of clustered mitochondria homolog (Cluh) as being most significantly down-regulated upon inhibition of Opa1 processing (fig. S4C). Cluh is an RNA-binding protein that stabilizes the mRNA of nuclear-encoded mitochondrial proteins and controls their translation (*56*). Loss of *Cluh* leads to down-regulation of catabolic pathways required under starvation and inhibition of OXPHOS (*57*), while a protective effect of Cluh overexpression has recently been observed in a model of cardiac hypertrophy (*58*).

Cox10$^{-/-}$*Opa1v1Δ4* hearts fail to maintain mitochondria

These observations prompted us to analyze the heart proteome of WT, *Cox10*$^{-/-}$, *Opa1v1Δ4*, and *Cox10*$^{-/-}$*Opa1v1Δ4* mice using a data-independent (DIA) mass spectrometry–based proteomics approach. In total, we were able to quantify 10,051 protein groups including 991 MitoCarta3.0 positive protein groups and statistical analysis [one-way analysis of variance (ANOVA), false discovery rate (FDR) < 0.05] revealed 3500 significantly changed proteins, out of which 562 were mitochondrial (table S2). The analysis of $\log_2$ fold change distributions of all proteins (relative to WT) against mitochondrial protein groups revealed overall decreased levels of mitochondrial proteins in *Cox10*$^{-/-}$ and *Cox10*$^{-/-}$*Opa1v1Δ4* hearts compared to those in WT hearts [according to MitoCarta3.0; (*59*)], which was even more pronounced in the absence of Opa1 processing (Fig. 6B).

We then performed a *K*-means clustering based on the *z*-score transformed $\log_2$ label-free quantification (LFQ) intensities of the significantly regulated mitochondrial (MitoCarta3.0) protein groups

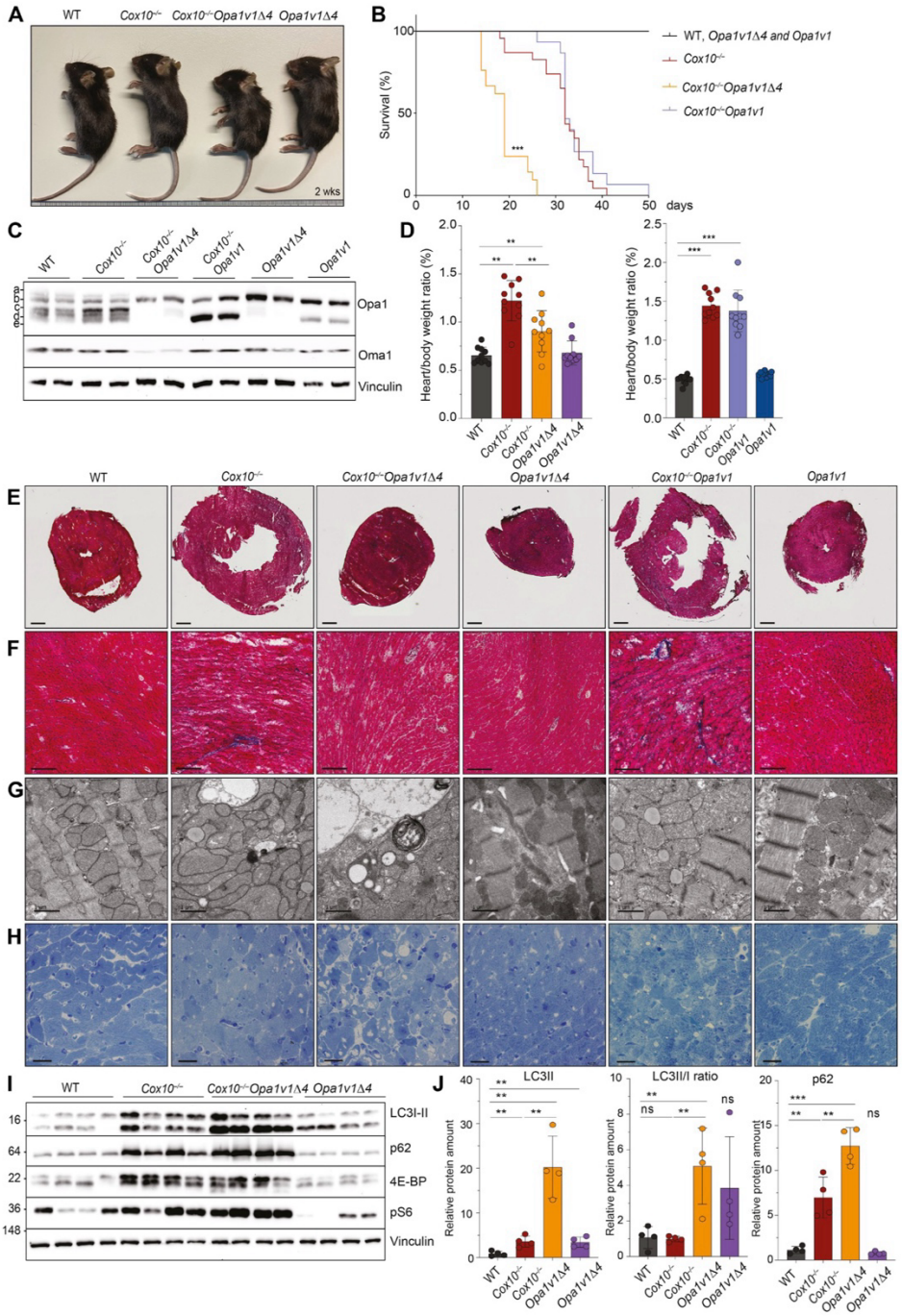

Fig. 5. Opa1 processing is protective in mitochondrial cardiomyopathy and supports hypertrophic growth. (**A** and **B**) *Opa1v1* and *Opa1v1Δ4* mice were crossed with cardiac and skeletal muscle–specific knockout mice of *Cox10*. Loss of Opa1 processing markedly reduced the life span of $Cox10^{-/-}$ mice, whereas V1 preserves the life span of $Cox10^{-/-}$ mice. (**C**) Increased Opa1 processing and s-Opa1 levels in $Cox10^{-/-}$ and $Cox10^{-/-}Opa1v1$ hearts indicating Oma1 activation. Opa1 processing is abolished in $Cox10^{-/-}Opa1v1\Delta4$ hearts. (**D**) $Cox10^{-/-}$ and $Cox10^{-/-}Opa1v1$ mice show an increased heart/body weight ratio, which is reduced in $Cox10^{-/-}Opa1v1\Delta4$ mice. Heart/body weight ratios were determined in age-matched mice and are from 2-week-old ($Cox10^{-/-}Opa1v1\Delta4$) and from 3.5-week-old $Cox10^{-/-}Opa1v1$ mice ($n = 10$; 5 females and 5 males). (**E**) Cross-sectional images from Masson's trichrome stained hearts showing hypertrophic growth of $Cox10^{-/-}$ and $Cox10^{-/-}Opa1v1$ hearts. Scale bars, 1 mm. (**F**) Close-up images (10×) of Masson's trichrome-stained hearts. (**G**) Representative TEM and (**H**) toluidine blue images from hearts, showing the accumulation of distorted mitochondria in $Cox10^{-/-}$, $Cox10^{-/-}Opa1v1$, and $Cox10^{-/-}Opa1v1\Delta4$ heart section and additionally accumulating vacuolar structures in $Cox10^{-/-}Opa1v1\Delta4$ heart sections. (G) Scale bars, 1 μm. (H) Scale bars, 20 μm. (**I** and **J**) Lipidated LC3II form and p62 accumulates in $Cox10^{-/-}$ and, at an even higher level, in $Cox10^{-/-}Opa1v1\Delta4$ hearts.

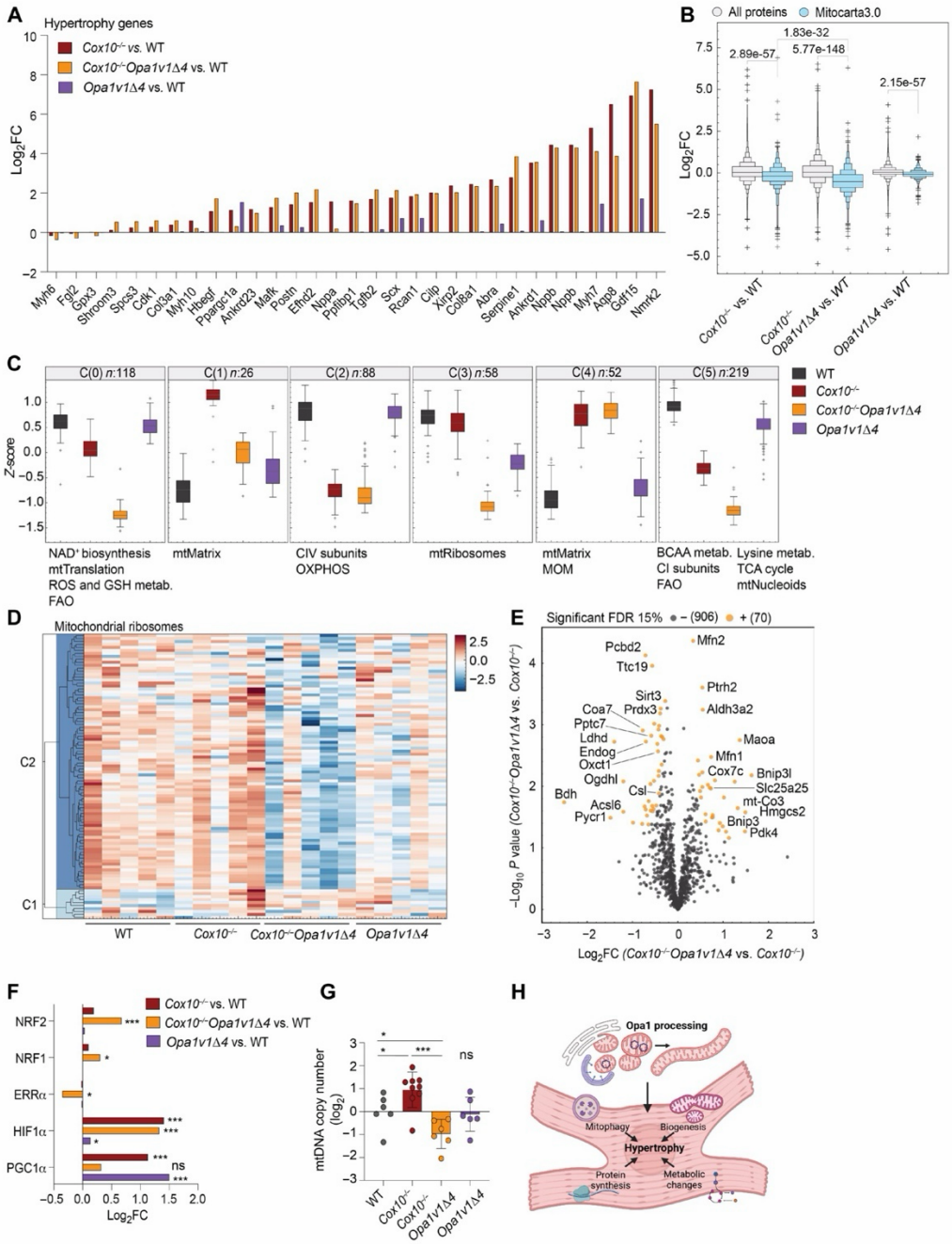

Fig. 6. Impaired mitochondrial biogenesis in *Cox10*$^{-/-}$*Opa1v1Δ4* hearts. (**A**) RNA-seq analysis of 2-week-old WT, *Cox10*$^{-/-}$, *Cox10*$^{-/-}$*Opa1v1Δ4*, and *Opa1v1Δ4* mice revealed increased expression of hypertrophic genes both in *Cox10*$^{-/-}$ and *Cox10*$^{-/-}$*Opa1v1Δ4* hearts. Hypertrophic genes were annotated according to (*55*). (**B**) Analysis of heart proteomes showed significant down-regulation of mitochondrial proteins (MitoCarta3.0) in *Cox10*$^{-/-}$ and *Opa1v1Δ4* hearts that was aggravated in *Cox10*$^{-/-}$*Opa1v1Δ4* hearts ($n = 5$). A Mann-Whitney *U* test was used to compare the $\log_2$ fold change ($\log_2$FC) distributions (**C**) *K*-means clustering result of the *z*-score–transformed LFQ intensities (six clusters). Significantly enriched Gene Ontology (GO)/MitoCarta3.0 pathways (FDR < 0.02, Fisher exact test) are listed below each cluster. The title indicates the cluster index and the number of proteins. ROS, reactive oxygen species; GSH, glutathione; FAO, fatty acid oxidation; BCAA, branched-chain amino acids; CI, complex I; CIV, complex IV; MOM, mitochondrial outer membrane; TCA, tricarboxylic acid cycle. (**D**) Heatmap of *z*-scores of transformed LFQ intensities of proteins annotated to the GO term "mitochondrial ribosome." (**E**) Volcano blot of mitochondrial proteins after normalization to mitochondrial mass in *Cox10*$^{-/-}$*Opa1v1Δ4* versus *Cox10*$^{-/-}$ hearts (Mitocarta3.0). (**F**) Relative expression (fold change) of selected transcription factors in mouse heart RNA-seq dataset (A) shown as $\log_2$FC. (**G**) Relative mtDNA levels in the heart of 2-week-old mice determined by qPCR for *cytB*. (**H**) Schematic presentation of the role of Opa1 processing in cardiac hypertrophy induced by OXPHOS dysfunction. Scheme was created with BioRender.com.

($N_{Cluster} = 6$) (Fig. 6C). This analysis revealed three distinct clusters (C0, C3, and C5) with a *Cox10*$^{-/-}$*Opa1v1Δ4*-dependent regulation. Gene Ontology/MitoCarta3.0 pathway enrichment revealed that several mitochondria-related metabolic pathways, such as nicotinamide adenine dinucleotide (oxidized form) (NAD^+) metabolism, branched-chain amino acid metabolism, fatty acid oxidation, mitochondrial fatty acid synthesis, or tricarboxylic acid cycle, were found at decreased levels in *Cox10*$^{-/-}$*Opa1v1Δ4* hearts compared to those in *Cox10*$^{-/-}$ hearts (cluster 0, $n = 118$, Fig. 6C). In addition, a down-regulation of mitochondrial ribosomes was observed (cluster 3, $n = 58$) (Fig. 6, C and D). Impaired Opa1 processing did affect neither the *Cox10* gene deletion–mediated loss of subunits of complex IV nor other OXPHOS complexes in cardiac mitochondria (cluster 2, $n = 88$, Fig. 6C and fig. S4D), which show impaired assembly and activity of cytochrome c oxidase (COX) complexes (fig. S4, E and F). Similarly, we observed the accumulation of cytoplasmic ribosomes both in *Cox10*$^{-/-}$ and *Cox10*$^{-/-}$*Opa1v1Δ4* hearts, likely reflecting a compensatory response to OXPHOS deficiency (fig. S4G). We conclude from these studies that *Cox10*$^{-/-}$*Opa1v1Δ4* hearts fail to maintain mitochondrial metabolic functions. Because cardiac hypertrophy is caused by an increase in myocyte size, which depends on mitochondrial proliferation, the reduced mitochondrial mass in *Cox10*$^{-/-}$*Opa1v1Δ4* hearts may limit hypertrophic cell growth.

To identify proteins whose steady-state levels specifically changed in response to impaired Opa1 processing, we normalized our proteomic data to mitochondrial mass, which was overall reduced in *Cox10*$^{-/-}$*Opa1v1Δ4* hearts (Fig. 6B). This analysis showed that the mitophagy receptors Bcl2-interacting protein 3 (Bnip3) and Bnip3-like (Bnip3l and Nix) as well as mitofusins Mfn1 and Mfn2 accumulated in *Cox10*$^{-/-}$*Opa1v1Δ4* heart when compared to those in *Cox10*$^{-/-}$ heart (two-sided *t* test, permutations 500; FDR < 15%). The accumulation of mitophagy receptors and decreased levels of the mitochondrial protein phosphatase targeting COQ7 (Pptc7), which has been shown to regulate mitophagy receptor stability (*60*, *61*), further supports our hypothesis of deregulated mitophagy in *Cox10*$^{-/-}$*Opa1v1Δ4* heart. However, our results do not exclude that alterations in the biogenesis of mitochondria contribute to the decreased mitochondrial mass in the heart of these mice. The mRNA levels of the key transcriptional coactivator Pgc1α were similar in WT and *Cox10*$^{-/-}$*Opa1v1Δ4* hearts but increased in *Cox10*$^{-/-}$ hearts (Fig. 6F). On the other hand, *Cox10*$^{-/-}$*Opa1v1Δ4* showed increased levels of the nuclear respiratory factors Nrf1 and Nrf2 and down-regulation of estrogen related receptor, alpha (ERRα), indicating dysregulation of mitochondrial biogenesis (Fig. 6F). Consistently, loss of Opa1 processing strongly reduced mtDNA levels in *Cox10*$^{-/-}$*Opa1v1Δ4* mitochondria, while *Cox10*$^{-/-}$ hearts showed increased mtDNA levels (Fig. 6G). Together, our proteome and transcriptome analysis of *Cox10*$^{-/-}$ and *Cox10*$^{-/-}$*Opa1v1Δ4* hearts suggests that disbalanced mitochondrial biogenesis and mitophagy limit cardiac hypertrophy (Fig. 6H), which is primarily a compensatory reaction to physiological stress, but almost inevitably leads to decompensation if stress persists, resulting eventually in cardiac failure.

DISCUSSION

Increased Opa1 processing promotes mitochondrial fragmentation under various stress conditions. The establishment of knock-in mouse models expressing exclusively a cleavable or non-cleavable Opa1 variant 1 (V1, V1Δ4) allowed the analysis of the physiological role of different Opa1 splice variants and of stress-induced Opa1 processing without confounding effects of the loss of pleiotropic processing peptidases. Our analysis shows that the expression of different Opa1 isoforms and Opa1 cleavage by Oma1 and Yme1l are dispensable for normal mouse development and health. In contrast, Oma1-mediated Opa1 processing limits mitochondrial cardiomyopathy in OXPHOS-deficient hearts, highlighting the importance of Opa1 cleavage and of s-Opa1 in mitochondrial heart disease.

Although four different splice variants of Opa1 are expressed in mice, *Opa1v1* mice expressing only V1 are healthy and develop normally. *Opa1v1* mice show normal metabolic parameters and visual functions compared to WT mice. While isoform-specific Opa1 functions may exist (*31*, *45*), they do not appear to contribute to the functional deficits observed in the absence of Opa1 in vivo. Similarly, because V1 lacks Yme1l processing sites, Yme1l-mediated processing is not required under normal physiological conditions or under metabolic stress of HFD feeding or cold stress. It is conceivable that Yme1l regulates Opa1 cleavage or overall Opa1 protein levels only in some cells or under specific stress conditions, such as in starvation and hypoxia, when Yme1l-mediated proteolysis limits the accumulation of Opa1 (*26*).

Increased cleavage of Opa1 by the stress-activated peptidase Oma1 drives mitochondrial fragmentation and contributes to mitochondrial quality control (*62*). Unexpectedly, however, abrogation of Oma1-mediated Opa1 cleavage by deletion of four amino acids at S1 did not disrupt normal mouse development. We observed a strong impairment of Opa1 processing in all tissues in *Opa1v1Δ4* mice, which was completely blocked in tissues, such as the heart, liver, and BAT. The absence of any phenotypes reminiscent of patients with ADOA with *OPA1* mutations in *Opa1v1Δ4* mice suggests that deficiencies in OPA1 processing and the absence of s-Opa1 do not contribute to the pathology of the disease. In addition, *Opa1v1Δ4* mice did not show increased diet-induced obesity or altered thermogenesis during cold stress, as has been observed in *Oma1*$^{-/-}$ mice (*39*). Therefore, these phenotypes appear to be unrelated to impaired Opa1 processing and may reflect defects in mitochondrial stress signaling or other metabolic functions in the absence of Oma1 (*40*, *43*, *44*, *50*).

The lack of gross phenotypes in *Opa1v1Δ4* mice contrasts with the severe consequences of mitochondrial fusion and fission defects (*63*). Our results are consistent with in vitro studies, showing that l-Opa1 is sufficient to promote mitochondrial fusion (*20*, *27*, *28*), although the presence of s-Opa1 further stimulates membrane fusion activity (*28*, *29*). This is remarkable considering the boost of mitochondrial dynamics during the development of some tissues such as the heart (*64*). Accumulation of l-Opa1 in the heart of *Opa1v1Δ4* mice preserved OXPHOS activity and mitochondrial ultrastructure, consistent with observations in mice lacking both Yme1l and Oma1 in cardiomyocytes (*35*). We only observed mild changes in cristae density in cardiac mitochondria using TEM. This is in agreement with a recent cryo–electron tomographic analysis of mitochondrial cristae shapes in cells accumulating only l-Opa1 (*65*). It should be noted, however, that our in vivo analysis did not distinguish between lamellar and tubular cristae, the ratio of which has been shown to be affected by Opa1 and Opa1 cleavage (*65*, *66*).

While dispensable for normal mouse development, inhibition of Opa1 processing aggravated the mitochondrial cardiomyopathy caused by the loss of Cox10 in cardiomyocytes. We observed a

shortened life span of Cox10-deficient mice in the presence of V1Δ4 but not V1, demonstrating that Opa1 processing and s-Opa1 formation exert a protective function in the OXPHOS-deficient heart. Notably, inhibition of Opa1 processing does not interfere with Oma1-mediated Dele1 processing and the induction of the ISR^{mt}, showing that Oma1 confers protection to the heart by the concerted regulation of both mitochondrial stress signaling and mitochondrial dynamics. The deleterious effect of impaired Opa1 processing in the OXPHOS-deficient heart may be explained by the limited fusion capacity of l-Opa1 in the absence of s-Opa1, although fusion (and fission) events are very rare in adult cardiac myocytes (*63*). Furthermore, we observed deregulated autophagic processes in Cox10-deficient hearts when Opa1 processing is impaired. Consistent with stalled mitophagy, we observed accumulation of lipidated LC3, of the autophagy receptor p62, and of the mitophagy receptors Bnip3l and Bnip3, as well as perinuclear clustering of mitochondria and prolonged interactions of mitochondria with the ER. Balanced Opa1 processing ensures mitochondrial dynamics. It is conceivable that the accumulation of l-Opa1, which promotes fusion, might limit mitophagy. However, we cannot exclude other mechanisms, such as prolonged ER-mitochondria contact sites. Damaged mitochondria may, therefore, exacerbate mitochondrial cardiomyopathy, but additional defects that are associated with the loss of Opa1 processing appear to contribute.

It should be noted that defects caused by the impaired Opa1 processing in Cox10-deficient hearts differ from previous mouse models lacking mitochondrial dynamic components in the heart, which may be explained by the detrimental effect of an OXPHOS deficiency on lysosomal functions (*52*–*54*). Inhibition of fission by deletion of dynamin-related protein 1 (*Drp1*) increases mitophagy and caused a loss of mitochondria in the heart (*67*). On the other hand, cardiac *Mfn2* ablation interrupts the autophagic removal of mitochondria from cardiomyocytes and leads to the accumulation of mitochondria without increasing mitophagy (*63*, *67*). These studies revealed that mitochondrial dynamics factors orchestrate mitochondrial biogenesis and mitophagy, the balance of which is critical for cardiac function (*68*). Consistently, our proteomic analysis showed decreased rather than increased mitochondrial protein levels in hearts lacking Cox10 and Opa1 cleavage despite impaired mitophagy, suggesting deficiencies in mitochondrial biogenesis. Cardiac hypertrophy is associated with increased myocyte growth, which depends on various mitochondrial functions (*69*–*71*). Reduced mitochondrial biogenesis could, therefore, explain why the loss of Opa1 processing impairs the hypertrophic growth of Cox10-deficient hearts, despite the induction of the hypertrophic gene expression programme. How the cleavage of Opa1 and the accumulation of s-Opa1 affect mitochondrial biogenesis remains to be elucidated. Regardless, our results reveal an intriguing regulatory circuit linking Opa1 processing to cardiac hypertrophy and highlight the role of Oma1 as a stress-protective protease in heart disease (*35*, *50*, *72*).

MATERIALS AND METHODS

Animal studies

All animal work was approved by local authorities (Landesamt für Natur, Umwelt und Verbraucherschutz Nordrhein-Westfalen, Germany), and animal procedures were carried out in accordance with European, national, and institutional guidelines and according to good practice of animal handling. Mice were maintained at the specific pathogen–free animal facility of the Max Planck Institute for Biology of Ageing with 12-hour light cycle and regular chow diet. *Opa1v1* and *Opa1v1Δ4* mice were created with the CRISPR-Cas9 system by electroporation of mouse zygotes with a NEPA21 Electroporator (CUY501P1-1.5 electrode) and the IDT Alt-R CRISPR-Cas9 System (Integrated DNA Technologies Inc.) with gRNAs and repair oligonucleotides listed in table S1. The Ckmm-Cre-$Cox10^{fl/fl}$ mice expressing cardiac and skeletal muscle–specific knockout of *Cox10* in the C57BL/6N background were previously published by us (*50*). Groups included male and female animals. Samples for protein and RNA extraction were taken after cervical dislocation and snap-frozen in liquid nitrogen. We used age-matched mice for protein, metabolome, and RNA analysis as well as histological analysis. For the cold-stress study, we used 12-week-old mice and kept them in 4°C for 12 hours with a rectal body temperate monitoring after 1, 2, 6, 9, and 12 hours. HFD (ssniff D12492) was applied to 54-week-old mice with a duration of 10 weeks. The diet consisted of 60 kJ% of fat (lard and soybean oil), 20 kJ% of proteins, and 20 kJ% of carbohydrates. HFD-fed and control animals were analyzed in a Phenomaster for respiratory exchange ratio (RER), food consumption, movement, and estimated heat production for a duration of 48 hours. At the German Mouse Clinic, mice were maintained in individually ventilated cages (IVC) with water and standard mouse chow according to the directive 2010/63/EU, German laws, and German Mouse Clinic (GMC) housing conditions (www.mouseclinic.de). All tests were approved by the responsible authority of the district government of Upper Bavaria. A cohort of 21 Opa1v1 mice (12 males/9 females) with corresponding controls (9 males/13 females) and 29 Opa1v1delta4 mice (15 males/14 females) with corresponding controls (14 males/14 females) entered the phenotypic pipeline at 68 weeks of age. Animal numbers may vary depending on the test performed, as indicated in the respective figure or table. The phenotypic tests were part of the GMC screening pipeline and performed according to standardized protocols as described before (*73*–*75*).

Histology

Animals were euthanized, tissues were rinsed in ice-cold phosphate-buffered saline (PBS) and fixed in 4% paraformaldehyde at 4°C for 72 hours. Paraffin-embedded tissues were cut into 5-μm sections deparaffinized in xylol, rehydrated and stained with hematoxylin and eosin or with Masson's trichrome, and imaged using 10× dry objective at Eclipse Ci histology microscope (Nikon Eclipse).

Hearts were snap-frozen in isopentane chilled with liquid nitrogen, cut into 10-μm sections with a cryostat, and stained for COX and/or succinate dehydrogenase (SDH) activity. Heart sections were incubated in standard COX solution for 12 min at room temperature (RT) and/or incubated in SDH solution for 5 min at 37°C. Oil Red O staining was performed for frozen sections after fixing the sections with a formalin-Ca^{2+} solution and stained in Oil Red O for 10 min. Nuclei were stained with Mayer's hematoxylin, and sections were mounted with aqueous mounting medium. For immunofluorescence staining, frozen sections were cut into 8-μm sections, blocked with 5% horse serum for 1 hour, and incubated overnight at 4°C in 2% bovine serum albumin (BSA) with selected antibodies: malondialdehyde (Abcam, ab243066) and p62 (Abnova, H00008878).

SDS-PAGE, BN, and immunoblot analysis

Mouse heart tissue was homogenized with Precellys 24 tissue homogenizer (Bertin Instruments) two times for 20 s at 6000 rpm in protein lysis buffer [50 mM tris-HCl (pH 7.5), 150 mM NaCl, 5 mM $MgCl_2$, 1 mM dithiothreitol, 10% glycerol, 2% SDS, and 1% Triton X-100] containing protease inhibitor cocktail (Roche) and phosphatase inhibitor cocktail (PhosSTOP, Roche). Protein concentration was determined with bicinchoninic acid (BCA) protein assay (Pierce). For protein extraction from MEFs, cells were washed with cold PBS and resuspended in ice-cold radioimmunoprecipitation assay buffer [50 mM tris-HCl (pH 7.4), 150 mM NaCl, 1% Triton X-100, 0.1% SDS, 0.05% sodium deoxycholate, and 1 mM EDTA] containing protease inhibitor cocktail (Roche) and phosphatase inhibitor cocktail (PhosSTOP, Roche). Samples were boiled before SDS-PAGE in 95°C for 5 min except in a case of OXPHOS subunit analysis. Total proteins from tissue or cells (25 to 50 μg) were separated using SDS-PAGE, followed by transfer to nitrocellulose membranes and immunoblotting with the following antibodies: Opa1 (BD Biosciences, 612607), Oma1 (Santa Cruz Biotechnology, sc-515788) SdhA (Abcam, ab14715), vinculin [Cell Signaling Technology (CST), no. 4650], tubulin (Sigma-Aldrich, T6074), p62 (Abnova, H00008878), P-4E-BP (CST, 2855), P-S6 (CST, no. 2211 L), Atf4 (CST, no. 11815), Chop/Ddit3 (CST, no. 2895), P-eIF2alpha (Abcam, ab32157), Mthfd2 (Proteintech, 12270-1-AP), Gpx4 (Abcam, ab105066), LC3I-II (CST, no. 2775S), and Atg5 (CST, no. 2630). Western blot images were acquired with Intas ChemoStar ECL Imager HR 6.0 and ChemoStar TS software (Intas).

For BN electrophoresis analysis, we isolated mitochondria from heart tissue with incubating in 2.5% trypsin for 10 min and then homogenized in homogenization buffer [225 mM sucrose, 1 mM EGTA, 0.2% BSA, 20 mM tris-HCl (pH 7.2), and protease inhibitor cocktail (Roche)] with 10 strokes using a glass Teflon homogenizer at 1000 rpm on ice. The homogenates were centrifuged at 1000*g* for 10 min at 4°C, and the supernatant was collected. Homogenization was repeated twice. Mitochondrial fraction was isolated with centrifugation at 8000*g* for 10 min at 4°C. Protein concentration was determined using a Bradford assay. Mitochondria were solubilized with digitonin (6 g/g), and proteins were separated by native PAGE using 3 to 12% gradient gels (Invitrogen) and incubated with COX activity buffer [0.05 M phosphate buffer (pH 7.4) with diaminobenzidine (0.5 mg/ml), catalase (20 μg/ml), cytochrome c (1 mg/ml), and 220 mM sucrose] and afterward with complex I activity reagents [2 mM tris-HCl (pH 7.4) with reduced form of NAD^+ (0.1 mg/ml) and Nitro blue tetrazolium chloride (2.5 mg/ml)].

Electron microscopy

One- to 2-mm piece from heart tissue was fixed in 2% formaldehyde/2% glutaraldehyde in 0.1 M cacodylic acid at least 48 hours at 4°C. Samples were then washed four times for 15 min in 0.1 M cacodylic acid and fixed with 2% osmiumtetroxid (Science Services) in 0.1 M cacodylic acid and washed again four times for 15 min in 0.1 M cacodylic acid. After changes in ethanol 50 to 100%, a mixture ethanol/propyleneoxid and 100% propyleneoxid the tissue was embedded in Epon fixative. Fixed tissue was cut in 70-nm sections on the ultramicrotome (UC6, Leica) on a grid and contrasted with 1.5% uranylacetate aqueous solution for 15 min at 37°C. Cuts were washed five times in water, incubated 4 min in lead citrate, and washed again five times in water and dried on a filter paper. Images were acquired with a transmission electron microscope (JEM 2100 Plus, JEOL), a OneView 4K camera (Gatan) with DigitalMicrograph software at 80 kV at room temperature.

WT and *Opa1v1Δ4* MEFs were grown on ACLAR–Fluoropolymer fil (Plano) and fixed by immersion using 2% glutaraldehyde in 0.1 M cacodylate buffer at pH 7.4. After postfixation using 1% osmiumtetroxid (Science Services) in 0.1 M cacodylic acid and preembedding staining with 1% uranylacetate (aqueous), tissue samples were dehydrated and embedded in Agar 100. Ultrathin sections (80 nm) were counterstained using 1% uranyl acetate (aqueous) and examined using a Talos L120C (Thermo Fisher Scientific). The area and mitochondria-ER contact sites were analyzed using Fiji.

Protein digestion for proteomics

Heart samples were lysed in 4% SDS in 100 mM Hepes-KOH (pH 8.5) using the Precellys tissue homogenizer for mechanical disruption of the tissue (according to the manufacturer's instructions). Protein (10 μg) was subjected for tryptic digestion. Proteins were reduced [10 mM tris(2-carboxyethyl)phosphine (TCEP)] and alkylated [20 mM chloarcetamide (CAA)] in the dark for 45 min at 45°C. Samples were subjected to SP3-based digestion protocol (*76*). Washed SP3 beads [Sera-Mag magnetic carboxylate modified particles (hydrophobic and hydrophilic) from Thermo Fisher Scientific] were mixed equally, and 3 μl of bead slurry was added to each sample. Acetonitrile was added to a final concentration of 50% and washed twice using 70% ethanol ($V = 200$ μl) on an in-house–made magnet. After an additional acetonitrile wash ($V = 200$ μl), 5 μl of digestion solution [10 mM Hepes-KOH (pH 8.5) containing 0.5 μg of trypsin (Sigma-Aldrich) and 0.5 μg of LysC (Wako)] was added to each sample and incubated overnight at 37°C. Peptides were desalted on a magnet using 2× 200 μl of acetonitrile and eluted using 5% dimethyl sulfoxide (DMSO) before 60 μl of 0.1% formic acid was added. Then, the peptides were further subjected to the StageTip technique (*77*) using SDB-RP [Styrenedivinylbenzene–Reversed Phase Sulfonate (Affinisep, France)] material.

Liquid chromatography and mass spectrometry for heart proteomics

Instrumentation consisted of an nLC-1200 (Thermo Fisher Scientific) coupled via the IonFlex electrospray source to an Exploris 480 mass spectrometer. For peptide separation, an Aurora (50 cm, 1.7-μm C18 bead size) was used at a column temperature of 55°C and a binary buffer (A) 0.1% formic acid and (B) 0.1% formic acid in 80% acetonitrile. The gradient was applied at a flow rate of 185 nl/min as follows: The content of buffer B was linearly raised from 5% to 32% in 100 min, followed by an increase to 50% within 10 min and then to 65% within 4 min. The column was washed at 70% B for 6 min.

The mass spectrometer operated in a data-independent mode and the FAIMS (high field asymmetric waveform ion mobility spectrometry) interface was attached and operated at a compensation voltage of −45. The inner electrode temperate was set to 100°C and the outer electrode was heated to 90°C. The total carrier flow was set to 3.5 liter/min. MS1 spectra were recorded in a range of 450 to 850 mass/charge ratio (m/z) using a resolution of 30,000 at 200 m/z. The radio frequence (RF) lens was set to 45%, and the spectra were recorded in profile mode. The MS2 spectra were recorded in a range of 500 to 740 m/z using an isolation window of 7 m/z and a window overlap of 1 m/z, resulting in a total number of scans of 34. The first mass was fixed to 200 m/z, and the resolution was set to 30,000 at 200 m/z. The automatic gain control (AGC) target was set to 700%,

and the maximum injection time was set to "auto." The data were acquired in centroid mode.

Analysis of proteomic data

DIA-NN (1.8.0) (Data independent acquisition–neuronal network) (*78*) was used to analyze data-independent raw files. The spectral library was created using the uniport reference *Mus musculus* protein proteome (one sequence per gene, UniProt, number of sequences: 21,984, UP000000589, downloaded June 2022) with the "Deep learning-based spectra and RTs prediction" turned on. Protease was set to trypsin, and a maximum of one missed cleavage was allowed. N-terminal methionine excision was set as a variable modification, and carbamidomethylation at cysteine residues was set as a fixed modification. The peptide length was set to 7 to 30 amino acids and the precursor m/z range was defined as 400 to 800 m/z. The option "Quantitative matrices" was enabled.

The FDR was set to 1%, and the mass accuracy (MS2 and MS1) as well as the scan window was set to 0 (automatic inference via DIA-NN). Match between runs was enabled. The neuronal network classifier worked in "double pass mode" and protein interference was set to "Isoform IDs." The quantification strategy was set to "robust LC (high accuracy)," and cross-run normalization was defined as "RT-dependent."

The "pg" (protein group) output (MaxLFQ intensities) (*79*) was further processed using Instant Clue (v.12.2) (*80*). In detail, pairwise comparisons were calculated using a two-sided t test using the $\log_2$-transformed LFQ intensities, and the FDR was controlled using a permutation-based approach [Statistical analysis of micro array (SAM); #permutations, 500; FDR < 5%; s0, 0.1]. In addition, a one-way ANOVA was used to identify significantly different abundant proteins in any group of the four genotypes (#permutations, 500; FDR < 5%; s0, 0.1). MitoCarta3.0 proteins were annotated, and a k-means clustering (z-score–transformed) was performed after filtering for ANOVA significance and MitoCarta3.0 protein groups (FDR < 0.05) using a total number of six clusters (determined by the "elbow" method) using Instant Clue (*80*). Pathway enrichment (MitoCarta Mito Pathways and Gene Ontologies) was assessed using a Fisher exact test followed by Benjamini-Hochberg FDR adjustments (FDR < 2%). Log_2-transformed LFQ intensities were normalized using the z-score (unit variance) and visualized in a heatmap using Euclidean distance and the complete method for the row-wise clustering.

Cell culture, transfection, and RNA interference

SV40-immortalized monoclonal MEFs from WT, *Opa1v1*, and *Opa1v1*Δ*4* mice were maintained in Dulbecco's modified Eagle's medium (DMEM)–GlutaMAX (Gibco) containing glucose (4.5 gliter^{-1}) supplemented with 10% fetal bovine serum (Sigma-Aldrich). *Oma1*$^{-/-}$ and corresponding WT MEFs were previously described (*20*). Cell lines were maintained at 37°C and 5% CO_2 and were routinely tested for *Mycoplasma* contamination. To create *Cox10*$^{-/-}$ *Opa1v1*Δ*4* MEFs, we transfected *Opa1v1*Δ*4* MEFs with an all-in-one GeneCRISPR gRNA construct (GeneScript). MEFs expressing active Cas9 with an anchored green fluorescent protein tag were sorted via FACS. After monoclonal selection, the *Cox10* deletion was verified via immunoblot and proteomics analysis. Cell numbers were monitored by Trypan blue exclusion and cell counting using the countess automated cell counter (Thermo Fisher Scientific). Cells were seeded at equal densities and grown to confluency for 72 hours without medium changes unless stated otherwise.

Human and mouse Opa1 was cloned in p3xFLAG CMV10 vector and used to create *Opa1v1*Δ*1*, *Opa1v1*Δ*2*, *Opa1v1*Δ*4*, and *Opa1v1*Δ*10* mutations by site-directed mutagenesis. WT and *Oma1*$^{-/-}$ MEFs were transiently transfected with Opa1-Flag for 48 hours, after which cells were treated with 20 μM Carbonyl cyanide m-chlorophenyl hydrazone (CCCP) or DMSO for 2 hours. Cell-free expression was done as in (*81*). Shortly, mouse Oma1 harboring a C-terminal hexahistidine tag together with C-terminally truncated and Myc-tagged human Opa1V1 with *Opa1v1*Δ*2*, *Opa1v1*Δ*4*, and *Opa1v1*Δ*10* mutations was expressed in a bacterial lysate–based, continuous-exchange cell-free expression system using pIVEX2.3d vector in the presence of liposomes. Proteins in Western blot analysis were detected with Myc antibody (CST, no. 2276).

RNA-seq and qPCR with reverse transcription

Heart tissue was homogenized with Precellys 24 tissue homogenizer (Bertin Instruments) two times for 10 s at 6000 rpm keeping samples on ice in between the cycles. Total RNA was extracted from mouse heart tissue samples using a NucleoSpin RNA kit (Macherey-Nagel), and RNA-seq was performed as in (*50*).

For reverse transcription polymerase chain reaction (PCR), cDNA was synthesized using the GoScript Reverse Transcription Mix (Promega). RNA concentrations were measured with Nanodrop ONE (Thermo Fisher Scientific). Reverse transcription–quantitative PCR (qPCR) was performed using the PowerSYBR Green PCR Master Mix (Applied Biosystems) and QuantStudio 5 and QuantStudio 6 Flex analyzers (Applied Biosystems) with QuantStudio Design & Analysis software (Applied Biosystems). For each independent sample, reverse transcription–qPCR was performed in technical duplicates.

Imaging

To label mitochondria with mEosEM, 1 μg of the plasmid encoding the protein was introduced into WT and *Opa1v1*Δ*4* MEFs via Gene juice transfection. Mito-mEosEM was a gift from P. Xu (Addgene, plasmid no. 132706). Cells were seeded on live-cell imaging glass bottom dishes (ibidi, μ-dish, 35-mm high). After 48 hours of incubation, mEosEM photoconversion was activated with a 405-nm laser pulse for 3 min (10% laser power). The mitochondrial network (10 μm^2) was photoconverted, and the activated mitochondrial area after 3 min was set as point zero. The activated signal was followed for 60 min using the excitation lasers at 488 and 561 nm, and the signal area was determined. Normalization to the zero value revealed the percentual area increase. The cells were imaged in DMEM buffered by Hepes at 37°C.

For mitochondrial morphology analysis, WT and *Opa1v1*Δ*4* MEFs were incubated with 20 μM CCCP or DMSO for 2 hours. Mitochondria were immunostained with Atp5ß (Invitrogen, A21351) and labeled with Alexa Fluor 488–conjugated antibody against mouse immunoglobulin G (IgG) (1:500). At least 100 cells from $n = 3$ independent replicates and treatments were analyzed for their mitochondrial length. Mitochondrial populations were classified into tubules, short tubules, and fragmented. Co-localization between mitochondria and ER was analyzed using immunocytochemistry, followed by colocalization analysis (JaCop Analysis, Fiji Plug-In). WT and *Opa1v1*Δ*4* MEFs were seeded on cover slips and harvested 24 hours after seeding. The cells were washed with PBS and fixed with 4% (v/v) paraformaldehyde. After fixation, cells were stained with Tom20 (Proteintech, 66777-1-lg) and Calnexin (Calbiochem, 208880/D19364)

primary antibodies. The signals were detected with an Alexa Fluor 488–conjugated antibody against mouse IgG (1:2000) and Alexa Fluor 546–conjugated antibody against rabbit IgG (1:2000).

For confocal imaging, we used the Leica Sp8-X confocal microscope equipped with a 40× oil/numerical aperture (NA) 1.45 objective. For super-resolution analysis, WT and *Opa1v1Δ4* MEFs were stained with DMEM supplemented with 250 nM PK mtOrange (GenVivo) for 20 min at 37°C as in (*82*). To remove unbound dye, cells were washed twice with DMEM and imaged 2 hours after staining at 37°C. PK mtOrange was excited at 561-nm wavelength, and stimulated emission depletion microscopy (STED) was performed using a pulsed depletion laser at 775-nm wavelength with 7× line accumulations. Pixel sizes of 20 nm were used for STED nanoscopy and a dwell time of 10 µs. The pinhole was set to 1.0 Airy Units (AU). For image deconvolution, the Huygens software was used. The cells were recorded using a Facility Line microscope (Abberior Instruments) equipped with an Olympus UPLXAPO 60× oil/NA 1.4 objective.

FACS analysis

Analysis was performed using a Cytek Amnis ImageStreamX Mk II (Cytek Corporation). Cells were selected on the basis of their scatter properties in the bright-field channel; 4′,6-diamidino-2-phenylindole was used for dead cell exclusion, excited by the 355-nm laser; and emission was detected using a 457/45-nm bandpass filter. Only cells with a gradient root mean square value above 55 in channel 1 were recorded. Samples were acquired with a low flow rate at ×40 magnification. Using the IDEAS Image Analysis Software (Cytek Corporation), the features area and diameter were created with an object mask, eroded by 1 pixel {Erode[Object(M01, Ch01, Tight), 1]}.

Statistics and reproducibility

Sample size was chosen according to our previous experience and common standards. Power analysis was used to predetermine sample size for mouse experiments. The sample size included at least three independent cell culture wells or mice where statistical evaluation was performed. Experiments were repeated as detailed in the figure legends. Error bars represent SD. Mice were assigned to experimental groups on the basis of genotypes available. Analyses were not blinded because experiments were performed and analyzed by the same researcher except for microscopy imaging where samples were numbered. The *n* number for all MEF cell experiments represents independent experimental cell cultures. Data analysis was performed with Prism GraphPad 9 and Instant Clue. Images were processed with ImageJ, and schematics were created with Adobe Illustrator 26.0.2 and BioRender.com. Data that were generated by the German Mouse Clinic were analyzed using R. Tests for genotype effects were made by using Wilcoxon rank sum test or linear models depending on the assumed distribution of the parameter and the questions addressed to the data. A P value $ < $0.05 has been used as level of significance; a correction for multiple testing has not been performed.

Supplementary Materials

The PDF file includes:
Figs. S1 to S4
Table S1
Legend for table S2

Other Supplementary Material for this manuscript includes the following:
Table S2

REFERENCES AND NOTES

1. M. Giacomello, A. Pyakurel, C. Glytsou, L. Scorrano, The cell biology of mitochondrial membrane dynamics. *Nat. Rev. Mol. Cell Biol.* **21**, 204–224 (2020).
2. R. Quintana-Cabrera, L. Scorrano, Determinants and outcomes of mitochondrial dynamics. *Mol. Cell* **83**, 857–876 (2023).
3. D. C. Chan, Mitochondrial dynamics and its involvement in disease. *Annu. Rev. Pathol.* **15**, 235–259 (2020).
4. N. M. B. Yapa, V. Lisnyak, B. Reljic, M. T. Ryan, Mitochondrial dynamics in health and disease. *FEBS Lett.* **595**, 1184–1204 (2021).
5. C. Alexander, M. Votruba, U. E. A. Pesch, D. L. Thiselton, S. Mayer, A. Moore, M. Rodriguez, U. Kellner, B. Leo-Kottler, G. Auburger, S. S. Bhattacharya, B. Wissinger, *OPA1*, encoding a dynamin-related GTPase, is mutated in autosomal dominant optic atrophy linked to chromosome 3q28. *Nat. Genet.* **26**, 211–215 (2000).
6. C. Delettre, G. Lenaers, J. M. Griffoin, N. Gigarel, C. Lorenzo, P. Belenguer, L. Pelloquin, J. Grosgeorge, C. Turc-Carel, E. Perret, C. Astarie-Dequeker, L. Lasquellec, B. Arnaud, B. Ducommun, J. Kaplan, C. P. Hamel, Nuclear gene *OPA1*, encoding a mitochondrial dynamin-related protein, is mutated in dominant optic atrophy. *Nat. Genet.* **26**, 207–210 (2000).
7. J. M. Chao de la Barca, D. Prunier-Mirebeau, P. Amati-Bonneau, M. Ferré, E. Sarzi, C. Bris, S. Leruez, A. Chevrollier, V. Desquiret-Dumas, N. Gueguen, C. Verny, C. Hamel, D. Miléa, V. Procaccio, D. Bonneau, G. Lenaers, P. Reynier, *OPA1*-related disorders: Diversity of clinical expression, modes of inheritance and pathophysiology. *Neurobiol. Dis.* **90**, 20–26 (2016).
8. J. J. Rahn, K. D. Stackley, S. S. Chan, Opa1 is required for proper mitochondrial metabolism in early development. *PLOS ONE* **8**, e59218 (2013).
9. M. V. Alavi, S. Bette, S. Schimpf, F. Schuettauf, U. Schraermeyer, H. F. Wehrl, L. Ruttiger, S. C. Beck, F. Tonagel, B. J. Pichler, M. Knipper, T. Peters, J. Laufs, B. Wissinger, A splice site mutation in the murine *Opa1* gene features pathology of autosomal dominant optic atrophy. *Brain* **130**, 1029–1042 (2007).
10. V. J. Davies, A. J. Hollins, M. J. Piechota, W. Yip, J. R. Davies, K. E. White, P. P. Nicols, M. E. Boulton, M. Votruba, Opa1 deficiency in a mouse model of autosomal dominant optic atrophy impairs mitochondrial morphology, optic nerve structure and visual function. *Hum. Mol. Genet.* **16**, 1307–1318 (2007).
11. Z. Zhang, N. Wakabayashi, J. Wakabayashi, Y. Tamura, W. J. Song, S. Sereda, P. Clerc, B. M. Polster, S. M. Aja, M. V. Pletnikov, T. W. Kensler, O. S. Shirihai, M. Iijima, M. A. Hussain, H. Sesaki, The dynamin-related GTPase Opa1 is required for glucose-stimulated ATP production in pancreatic beta cells. *Mol. Biol. Cell* **22**, 2235–2245 (2011).
12. C. Bean, M. Audano, T. Varanita, F. Favaretto, M. Medaglia, M. Gerdol, L. Pernas, F. Stasi, M. Giacomello, S. Herkenne, M. Muniandy, S. Heinonen, E. Cazaly, M. Ollikainen, G. Milan, A. Pallavicini, K. H. Pietiläinen, R. Vettor, N. Mitro, L. Scorrano, The mitochondrial protein Opa1 promotes adipocyte browning that is dependent on urea cycle metabolites. *Nat. Metab.* **3**, 1633–1647 (2021).
13. A. G. Gomez-Valades, M. Pozo, L. Varela, M. B. Boudjadja, S. Ramírez, I. Chivite, E. Eyre, R. Haddad-Tóvolli, A. Obri, M. Milà-Guasch, J. Altirriba, M. Schneeberger, M. Imbernón, A. R. Garcia-Rendueles, P. Gama-Perez, J. Rojo-Ruiz, B. Rácz, M. T. Alonso, R. Gomis, A. Zorzano, G. D'Agostino, C. V. Alvarez, R. Nogueiras, P. M. Garcia-Roves, T. L. Horvath, M. Claret, Mitochondrial cristae-remodeling protein OPA1 in POMC neurons couples Ca^{2+} homeostasis with adipose tissue lipolysis. *Cell Metab.* **33**, 1820–1835.e9 (2021).
14. C. Tezze, V. Romanello, M. A. Desbats, G. P. Fadini, M. Albiero, G. Favaro, S. Ciciliot, M. E. Soriano, V. Morbidoni, C. Cerqua, S. Loefler, H. Kern, C. Franceschi, S. Salvioli, M. Conte, B. Blaauw, S. Zampieri, L. Salviati, L. Scorrano, M. Sandri, Age-associated loss of OPA1 in muscle impacts muscle mass, metabolic homeostasis, systemic inflammation, and epithelial senescence. *Cell Metab.* **25**, 1374–1389.e6 (2017).
15. H. Lee, T. J. Lee, C. A. Galloway, W. Zhi, W. Xiao, K. L. de Mesy Bentley, A. Sharma, Y. Teng, H. Sesaki, Y. Yoon, The mitochondrial fusion protein OPA1 is dispensable in the liver and its absence induces mitohormesis to protect liver from drug-induced injury. *Nat. Commun.* **14**, 6721 (2023).
16. T. Yamada, D. Murata, Y. Adachi, K. Itoh, S. Kameoka, A. Igarashi, T. Kato, Y. Araki, R. L. Huganir, T. M. Dawson, T. Yanagawa, K. Okamoto, M. Iijima, H. Sesaki, Mitochondrial stasis reveals p62-mediated ubiquitination in parkin-independent mitophagy and mitigates nonalcoholic fatty liver disease. *Cell Metab.* **28**, 588–604.e5 (2018).
17. G. Civiletto, T. Varanita, R. Cerutti, T. Gorletta, S. Barbaro, S. Marchet, C. Lamperti, C. Viscomi, L. Scorrano, M. Zeviani, Opa1 overexpression ameliorates the phenotype of two mitochondrial disease mouse models. *Cell Metab.* **21**, 845–854 (2015).
18. T. Varanita, M. E. Soriano, V. Romanello, T. Zaglia, R. Quintana-Cabrera, M. Semenzato, R. Menabò, V. Costa, G. Civiletto, P. Pesce, C. Viscomi, M. Zeviani, F. di Lisa, M. Mongillo, M. Sandri, L. Scorrano, The OPA1-dependent mitochondrial cristae remodeling pathway controls atrophic, apoptotic, and ischemic tissue damage. *Cell Metab.* **21**, 834–844 (2015).
19. N. Ishihara, Y. Fujita, T. Oka, K. Mihara, Regulation of mitochondrial morphology through proteolytic cleavage of OPA1. *EMBO J.* **25**, 2966–2977 (2006).

20. R. Anand, T. Wai, M. J. Baker, N. Kladt, A. C. Schauss, E. Rugarli, T. Langer, The *i*-AAA protease YME1L and OMA1 cleave OPA1 to balance mitochondrial fusion and fission. *J. Cell Biol.* **204**, 919–929 (2014).
21. M. J. Baker, P. A. Lampe, D. Stojanovski, A. Korwitz, R. Anand, T. Tatsuta, T. Langer, Stress-induced OMA1 activation and autocatalytic turnover regulate OPA1-dependent mitochondrial dynamics. *EMBO J.* **33**, 578–593 (2014).
22. S. Ehses, I. Raschke, G. Mancuso, A. Bernacchia, S. Geimer, D. Tondera, J. C. Martinou, B. Westermann, E. I. Rugarli, T. Langer, Regulation of OPA1 processing and mitochondrial fusion by m-AAA protease isoenzymes and OMA1. *J. Cell Biol.* **187**, 1023–1036 (2009).
23. L. Griparic, T. Kanazawa, A. M. van der Bliek, Regulation of the mitochondrial dynamin-like protein Opa1 by proteolytic cleavage. *J. Cell Biol.* **178**, 757–764 (2007).
24. B. Head, L. Griparic, M. Amiri, S. Gandre-Babbe, A. M. van der Bliek, Inducible proteolytic inactivation of OPA1 mediated by the OMA1 protease in mammalian cells. *J. Cell Biol.* **187**, 959–966 (2009).
25. Z. Song, H. Chen, M. Fiket, C. Alexander, D. C. Chan, OPA1 processing controls mitochondrial fusion and is regulated by mRNA splicing, membrane potential, and Yme1L. *J. Cell Biol.* **178**, 749–755 (2007).
26. T. MacVicar, Y. Ohba, H. Nolte, F. C. Mayer, T. Tatsuta, H. G. Sprenger, B. Lindner, Y. Zhao, J. Li, C. Bruns, M. Krüger, M. Habich, J. Riemer, R. Schwarzer, M. Pasparakis, S. Henschke, J. C. Brüning, N. Zamboni, T. Langer, Lipid signalling drives proteolytic rewiring of mitochondria by YME1L. *Nature* **575**, 361–365 (2019).
27. H. Lee, S. B. Smith, Y. Yoon, The short variant of the mitochondrial dynamin OPA1 maintains mitochondrial energetics and cristae structure. *J. Biol. Chem.* **292**, 7115–7130 (2017).
28. T. Ban, T. Ishihara, H. Kohno, S. Saita, A. Ichimura, K. Maenaka, T. Oka, K. Mihara, N. Ishihara, Molecular basis of selective mitochondrial fusion by heterotypic action between OPA1 and cardiolipin. *Nat. Cell Biol.* **19**, 856–863 (2017).
29. Y. Ge, X. Shi, S. Boopathy, J. McDonald, A. W. Smith, L. H. Chao, Two forms of Opa1 cooperate to complete fusion of the mitochondrial inner-membrane. *eLife* **9**, e50973 (2020).
30. O. Guillery, F. Malka, T. Landes, E. Guillou, C. Blackstone, A. Lombès, P. Belenguer, D. Arnoult, M. Rojo, Metalloprotease-mediated OPA1 processing is modulated by the mitochondrial membrane potential. *Biol. Cell* **100**, 315–325 (2008).
31. V. del Dotto, P. Mishra, S. Vidoni, M. Fogazza, A. Maresca, L. Caporali, J. M. McCaffery, M. Cappelletti, E. Baruffini, G. Lenaers, D. Chan, M. Rugolo, V. Carelli, C. Zanna, OPA1 isoforms in the hierarchical organization of mitochondrial functions. *Cell Rep.* **19**, 2557–2571 (2017).
32. S. B. Nyenhuis, X. Wu, M. P. Strub, Y. I. Yim, A. E. Stanton, V. Baena, Z. A. Syed, B. Canagarajah, J. A. Hammer, J. E. Hinshaw, OPA1 helical structures give perspective to mitochondrial dysfunction. *Nature* **620**, 1109–1116 (2023).
33. A. von der Malsburg, G. M. Sapp, K. E. Zuccaro, A. von Appen, F. R. Moss III, R. Kalia, J. A. Bennett, L. A. Abriata, M. Dal Peraro, M. van der Laan, A. Frost, H. Aydin, Structural mechanism of mitochondrial membrane remodelling by human OPA1. *Nature* **620**, 1101–1108 (2023).
34. C. Delettre, J. M. Griffoin, J. Kaplan, H. Dollfus, B. Lorenz, L. Faivre, G. Lenaers, P. Belenguer, C. P. Hamel, Mutation spectrum and splicing variants in the OPA1 gene. *Hum. Genet.* **109**, 584–591 (2001).
35. T. Wai, J. García-Prieto, M. J. Baker, C. Merkwirth, P. Benit, P. Rustin, F. J. Rupérez, C. Barbas, B. Ibañez, T. Langer, Imbalanced OPA1 processing and mitochondrial fragmentation cause heart failure in mice. *Science* **350**, aad0116 (2015).
36. A. Korwitz, C. Merkwirth, R. Richter-Dennerlein, S. E. Tröder, H. G. Sprenger, P. M. Quirós, C. López-Otín, E. I. Rugarli, T. Langer, Loss of OMA1 delays neurodegeneration by preventing stress-induced OPA1 processing in mitochondria. *J. Cell Biol.* **212**, 157–166 (2016).
37. H. G. Sprenger, G. Wani, A. Hesseling, T. König, M. Patron, T. MacVicar, S. Ahola, T. Wai, E. Barth, E. I. Rugarli, M. Bergami, T. Langer, Loss of the mitochondrial *i*-AAA protease YME1L leads to ocular dysfunction and spinal axonopathy. *EMBO Mol. Med.* **11**, e9288 (2019).
38. X. Xiao, Y. Hu, P. M. Quirós, Q. Wei, C. López-Otín, Z. Dong, OMA1 mediates OPA1 proteolysis and mitochondrial fragmentation in experimental models of ischemic kidney injury. *Am. J. Physiol. Renal Physiol.* **306**, F1318–F1326 (2014).
39. P. M. Quiros, A. J. Ramsay, D. Sala, E. Fernández-Vizarra, F. Rodríguez, J. R. Peinado, M. S. Fernández-García, J. A. Vega, J. A. Enríquez, A. Zorzano, C. López-Otín, Loss of mitochondrial protease OMA1 alters processing of the GTPase OPA1 and causes obesity and defective thermogenesis in mice. *EMBO J.* **31**, 2117–2133 (2012).
40. P. Rivera-Mejias, Á. J. Narbona-Pérez, L. Hasberg, L. Kroczek, A. Bahat, S. Lawo, K. Folz-Donahue, A.-L. Schumacher, S. Ahola, F. C. Mayer, P. Giavalisco, H. Nolte, S. Lavandero, T. Langer, The mitochondrial protease OMA1 acts as a metabolic safeguard upon nuclear DNA damage. *Cell Rep.* **42**, 112332 (2023).
41. M. P. Viana, R. M. Levytskyy, R. Anand, A. S. Reichert, O. Khalimonchuk, Protease OMA1 modulates mitochondrial bioenergetics and ultrastructure through dynamic association with MICOS complex. *iScience* **24**, 102119 (2021).
42. Z. Wu, M. Zuo, L. Zeng, K. Cui, B. Liu, C. Yan, L. Chen, J. Dong, F. Shangguan, W. Hu, H. He, B. Lu, Z. Song, OMA1 reprograms metabolism under hypoxia to promote colorectal cancer development. *EMBO Rep.* **22**, e50827 (2021).
43. X. Guo, G. Aviles, Y. Liu, R. Tian, B. A. Unger, Y. H. T. Lin, A. P. Wiita, K. Xu, M. A. Correia, M. Kampmann, Mitochondrial stress is relayed to the cytosol by an OMA1-DELE1-HRI pathway. *Nature* **579**, 427–432 (2020).
44. E. Fessler, E. M. Eckl, S. Schmitt, I. A. Mancilla, M. F. Meyer-Bender, M. Hanf, J. Philippou-Massier, S. Krebs, H. Zischka, L. T. Jae, A pathway coordinated by DELE1 relays mitochondrial stress to the cytosol. *Nature* **579**, 433–437 (2020).
45. A. Olichon, G. ElAchouri, L. Baricault, C. Delettre, P. Belenguer, G. Lenaers, OPA1 alternate splicing uncouples an evolutionary conserved function in mitochondrial fusion from a vertebrate restricted function in apoptosis. *Cell Death Differ.* **14**, 682–692 (2007).
46. R. Wang, P. Mishra, S. D. Garbis, A. Moradian, M. J. Sweredoski, D. C. Chan, Identification of new OPA1 cleavage site reveals that short isoforms regulate mitochondrial fusion. *Mol. Biol. Cell* **32**, 157–168 (2021).
47. V. R. Akepati, E. C. Müller, A. Otto, H. M. Strauss, M. Portwich, C. Alexander, Characterization of OPA1 isoforms isolated from mouse tissues. *J. Neurochem.* **106**, 372–383 (2008).
48. J. R. Friedman, L. L. Lackner, M. West, J. R. DiBenedetto, J. Nunnari, G. K. Voeltz, ER tubules mark sites of mitochondrial division. *Science* **334**, 358–362 (2011).
49. J. Qiu, F. Yue, P. Zhu, J. Chen, F. Xu, L. Zhang, K. H. Kim, M. M. Snyder, N. Luo, H. W. Xu, F. Huang, W. A. Tao, S. Kuang, FAM210A is essential for cold-induced mitochondrial remodeling in brown adipocytes. *Nat. Commun.* **14**, 6344 (2023).
50. S. Ahola, P. Rivera Mejías, S. Hermans, S. Chandragiri, P. Giavalisco, H. Nolte, T. Langer, OMA1-mediated integrated stress response protects against ferroptosis in mitochondrial cardiomyopathy. *Cell Metab.* **34**, 1875–1891.e7 (2022).
51. M. P. Nobrega, F. G. Nobrega, A. Tzagoloff, COX10 codes for a protein homologous to the ORF1 product of Paracoccus denitrificans and is required for the synthesis of yeast cytochrome oxidase. *J. Biol. Chem.* **265**, 14220–14226 (1990).
52. F. Baixauli, R. Acín-Pérez, C. Villarroya-Beltrí, C. Mazzeo, N. Nuñez-Andrade, E. Gabandé-Rodriguez, M. D. Ledesma, A. Blázquez, M. A. Martin, J. M. Falcón-Pérez, J. M. Redondo, J. A. Enríquez, M. Mittelbrunn, Mitochondrial respiration controls lysosomal function during inflammatory T cell responses. *Cell Metab.* **22**, 485–498 (2015).
53. J. Demers-Lamarche, G. Guillebaud, M. Tlili, K. Todkar, N. Bélanger, M. Grondin, A. P. Nguyen, J. Michel, M. Germain, Loss of mitochondrial function impairs lysosomes. *J. Biol. Chem.* **291**, 10263–10276 (2016).
54. L. Fernandez-Mosquera, K. F. Yambire, R. Couto, L. Pereyra, K. Pabis, A. H. Ponsford, C. V. Diogo, M. Stagi, I. Milosevic, N. Raimundo, Mitochondrial respiratory chain deficiency inhibits lysosomal hydrolysis. *Autophagy* **15**, 1572–1591 (2019).
55. M. Vigil-Garcia, C. J. Demkes, J. E. C. Eding, D. Versteeg, H. de Ruiter, I. Perini, L. Kooijman, M. M. Gladka, F. W. Asselbergs, A. Vink, M. Harakalova, A. Bossu, T. A. B. van Veen, C. J. Boogerd, E. van Rooij, Gene expression profiling of hypertrophic cardiomyocytes identifies new players in pathological remodelling. *Cardiovasc. Res.* **117**, 1532–1545 (2021).
56. J. Gao, D. Schatton, P. Martinelli, H. Hansen, D. Pla-Martin, E. Barth, C. Becker, J. Altmueller, P. Frommolt, M. Sardiello, E. I. Rugarli, CLUH regulates mitochondrial biogenesis by binding mRNAs of nuclear-encoded mitochondrial proteins. *J. Cell Biol.* **207**, 213–223 (2014).
57. D. Schatton, D. Pla-Martin, M. C. Marx, H. Hansen, A. Mourier, I. Nemazanyy, A. Pessia, P. Zentis, T. Corona, V. Kondylis, E. Barth, A. C. Schauss, V. Velagapudi, E. I. Rugarli, CLUH regulates mitochondrial metabolism by controlling translation and decay of target mRNAs. *J. Cell Biol.* **216**, 675–693 (2017).
58. S. Singh, A. Gaur, R. K. Sharma, R. Kumari, S. Prakash, S. Kumari, A. D. Chaudhary, P. Prasun, P. Pant, H. Hunkler, T. Thum, K. Jagavelu, P. Bharati, K. Hanif, P. Chitkara, S. Kumar, K. Mitra, S. K. Gupta, Musashi-2 causes cardiac hypertrophy and heart failure by inducing mitochondrial dysfunction through destabilizing Cluh and Smyd1 mRNA. *Basic Res. Cardiol.* **118**, 46 (2023).
59. S. Rath, R. Sharma, R. Gupta, T. Ast, C. Chan, T. J. Durham, R. P. Goodman, Z. Grabarek, M. E. Haas, W. H. W. Hung, P. R. Joshi, A. A. Jourdain, S. H. Kim, A. V. Kotrys, S. S. Lam, J. G. McCoy, J. D. Meisel, M. Miranda, A. Panda, A. Patgiri, R. Rogers, S. Sadre, H. Shah, O. S. Skinner, T. L. To, M. A. Walker, H. Wang, P. S. Ward, J. Wengrod, C. C. Yuan, S. E. Calvo, V. K. Mootha, MitoCarta3.0: An updated mitochondrial proteome now with sub-organelle localization and pathway annotations. *Nucleic Acids Res.* **49**, D1541–D1547 (2021).
60. N. M. Niemi, L. R. Serrano, L. K. Muehlbauer, C. E. Balnis, L. Wei, A. J. Smith, K. L. Kozul, M. Forny, O. M. Connor, E. H. Rashan, E. Shishkova, K. L. Schueler, M. P. Keller, A. D. Attie, J. R. Friedman, J. K. Pagan, J. J. Coon, D. J. Pagliarini, PPTC7 maintains mitochondrial protein content by suppressing receptor-mediated mitophagy. *Nat. Commun.* **14**, 6431 (2023).
61. Y. Sun, Y. Cao, H. Wan, A. Memetimin, Y. Cao, L. Li, C. Wu, M. Wang, S. Chen, Q. Li, Y. Ma, M. Dong, H. Jiang, A mitophagy sensor PPTC7 controls BNIP3 and NIX degradation to regulate mitochondrial mass. *Mol. Cell* **84**, 327–344.e9 (2024).

62. J. M. Winter, T. Yadav, J. Rutter, Stressed to death: Mitochondrial stress responses connect respiration and apoptosis in cancer. *Mol. Cell* **82**, 3321–3332 (2022).
63. G. Gong, M. Song, G. Csordas, D. P. Kelly, S. J. Matkovich, G. W. Dorn II, Parkin-mediated mitophagy directs perinatal cardiac metabolic maturation in mice. *Science* **350**, aad2459 (2015).
64. G. W. Dorn II, R. B. Vega, D. P. Kelly, Mitochondrial biogenesis and dynamics in the developing and diseased heart. *Genes Dev.* **29**, 1981–1991 (2015).
65. M. Y. Fry, P. P. Navarro, P. Hakim, V. Y. Ananda, X. Qin, J. C. Landoni, S. Rath, Z. Inde, C. M. Lugo, B. E. Luce, Y. Ge, J. L. McDonald, I. Ali, L. L. Ha, B. P. Kleinstiver, D. C. Chan, K. A. Sarosiek, L. H. Chao, In situ architecture of Opa1-dependent mitochondrial cristae remodeling. *EMBO J.* **43**, 391–413 (2024).
66. S. Suga, K. Nakamura, Y. Nakanishi, B. M. Humbel, H. Kawai, Y. Hirabayashi, An interactive deep learning-based approach reveals mitochondrial cristae topologies. *PLoS Biol.* **21**, e3002246 (2023).
67. M. Song, K. Mihara, Y. Chen, L. Scorrano, G. W. Dorn II, Mitochondrial fission and fusion factors reciprocally orchestrate mitophagic culling in mouse hearts and cultured fibroblasts. *Cell Metab.* **21**, 273–286 (2015).
68. M. Song, A. Franco, J. A. Fleischer, L. Zhang, G. W. Dorn II, Abrogating mitochondrial dynamics in mouse hearts accelerates mitochondrial senescence. *Cell Metab.* **26**, 872–883.e5 (2017).
69. M. Nakamura, J. Sadoshima, Mechanisms of physiological and pathological cardiac hypertrophy. *Nat. Rev. Cardiol.* **15**, 387–407 (2018).
70. J. Ritterhoff, R. Tian, Metabolic mechanisms in physiological and pathological cardiac hypertrophy: New paradigms and challenges. *Nat. Rev. Cardiol.* **20**, 812–829 (2023).
71. D. Yang, H.-Q. Liu, F.-Y. Liu, Z. Guo, P. An, M.-Y. Wang, Z. Yang, D. Fan, Q.-Z. Tang, Mitochondria in pathological cardiac hypertrophy research and therapy. *Front. Cardiovasc. Med.* **8**, 822969 (2022).
72. R. Acin-Perez, A. V. Lechuga-Vieco, M. del Mar Muñoz, R. Nieto-Arellano, C. Torroja, F. Sánchez-Cabo, C. Jiménez, A. González-Guerra, I. Carrascoso, C. Benincá, P. M. Quiros, C. López-Otín, J. M. Castellano, J. Ruíz-Cabello, L. J. Jiménez-Borreguero, J. A. Enríquez, Ablation of the stress protease OMA1 protects against heart failure in mice. *Sci. Transl. Med.* **10**, eaan4935 (2018).
73. H. Fuchs, V. Gailus-Durner, T. Adler, J. A. Aguilar-Pimentel, L. Becker, J. Calzada-Wack, P. da Silva-Buttkus, F. Neff, A. Götz, W. Hans, S. M. Hölter, M. Horsch, G. Kastenmüller, E. Kemter, C. Lengger, H. Maier, M. Matloka, G. Möller, B. Naton, C. Prehn, O. Puk, I. Rácz, B. Rathkolb, W. Römisch-Margl, J. Rozman, R. Wang-Sattler, A. Schrewe, C. Stöger, M. Tost, J. Adamski, B. Aigner, J. Beckers, H. Behrendt, D. H. Busch, I. Esposito, J. Graw, T. Illig, B. Ivandic, M. Klingenspor, T. Klopstock, E. Kremmer, M. Mempel, S. Neschen, M. Ollert, H. Schulz, K. Suhre, E. Wolf, W. Wurst, A. Zimmer, M. Hrabě de Angelis, Mouse phenotyping. *Methods* **53**, 120–135 (2011).
74. D. Pawliczek, C. Dalke, H. Fuchs, V. Gailus-Durner, M. Hrabě de Angelis, J. Graw, O. V. Amarie, Spectral domain - Optical coherence tomography (SD-OCT) as a monitoring tool for alterations in mouse lenses. *Exp. Eye Res.* **190**, 107871 (2020).
75. B. Benkner, M. Mutter, G. Ecke, T. A. Münch, Characterizing visual performance in mice: An objective and automated system based on the optokinetic reflex. *Behav. Neurosci.* **127**, 788–796 (2013).
76. C. S. Hughes, S. Foehr, D. A. Garfield, E. E. Furlong, L. M. Steinmetz, J. Krijgsveld, Ultrasensitive proteome analysis using paramagnetic bead technology. *Mol. Syst. Biol.* **10**, 757 (2014).
77. Y. Ishihama, J. Rappsilber, M. Mann, Modular stop and go extraction tips with stacked disks for parallel and multidimensional Peptide fractionation in proteomics. *J. Proteome Res.* **5**, 988–994 (2006).
78. V. Demichev, C. B. Messner, S. I. Vernardis, K. S. Lilley, M. Ralser, DIA-NN: Neural networks and interference correction enable deep proteome coverage in high throughput. *Nat. Methods* **17**, 41–44 (2020).
79. J. Cox, M. Y. Hein, C. A. Luber, I. Paron, N. Nagaraj, M. Mann, Accurate proteome-wide label-free quantification by delayed normalization and maximal peptide ratio extraction, termed MaxLFQ. *Mol. Cell. Proteomics* **13**, 2513–2526 (2014).
80. H. Nolte, T. D. MacVicar, F. Tellkamp, M. Krüger, Instant clue: A software suite for interactive data visualization and analysis. *Sci. Rep.* **8**, 12648 (2018).
81. S. Saita, T. Tatsuta, P. A. Lampe, T. König, Y. Ohba, T. Langer, PARL partitions the lipid transfer protein STARD7 between the cytosol and mitochondria. *EMBO J.* **37**, e97909 (2018).
82. T. Liu, T. Stephan, P. Chen, J. Keller-Findeisen, J. Chen, D. Riedel, Z. Yang, S. Jakobs, Z. Chen, Multi-color live-cell STED nanoscopy of mitochondria with a gentle inner membrane stain. *Proc. Natl. Acad. Sci. U.S.A.* **119**, e2215799119 (2022).

Acknowledgments: We thank the FACS & Imaging Core Facility at the Max Planck Institute for Biology of Ageing and the CECAD Imaging Facility from where we especially would like to acknowledge C. Jüngst for the for the support in the STED recordings and the mito-mEosEM experimental setup. RNA-seq was performed in the Cologne Centre for Genomics, and bioinformatic analysis for RNA-seq data was performed in the Bioinformatics Core Facility at the MPI Ageing. Animal housing and treatment experiments were performed in the Comparative Biology Core Facility at the MPI Ageing with valuable help from the Phenotyping Core Facility (MPI Ageing) where we especially want to acknowledge A. Mesaros and M. Purrio. We wish to thank D. Diehl for excellent technical help in proteomic analysis and C. Lienkamp and P. Wollek for valuable help with animal work and permits. **Funding:** This work was support by grants from the Deutsche Forschungsgemeinschaft (DFG; German Research Foundation) - SFB 1218–Projektnummer 269925409) to T.L. The German Mouse Clinic receives funding from the German Federal Ministry of Education and Research (Infrafrontier grant 01KX1012 to M.H.d.A.) and German Center for Diabetes Research (DZD) (M.H.d.A.). **Author contributions:** Conceptualization: F.M., S.A., and T.L. Methodology and formal analysis: H.N. and D.R. Investigation: S.A., L.A.P., F.M, P.L, S.H. S.C., L.B, O.V.A., and D.R. Writing: S.A. and T.L. Conceptualization of the phenotypic tests at the German Mouse Clinic: M.H.d.A. Project administration: H.F, V.G.-D., and T.L. **Competing interests:** The authors declare that they have no competing interests. **Data and materials availability:** All data needed to evaluate the conclusions in the paper are present in the paper and/or the Supplementary Materials. Data and materials can be provided by T.L.'s pending scientific review and a completed material transfer agreement. Proteomics data have been deposited to the PRIDE Ensembl server under the identifier PXD048804. Transcriptomics data are available in Gene Expression Omnibus (GEO; https://www.ncbi.nlm.nih.gov/geo/) archives. RNA-seq data have been downloaded to NIH Sequence Read Archive (SRA) with BioProjectID: PRJNA1079536 and are publicly available.

Submitted 4 March 2024
Accepted 28 June 2024
Published 2 August 2024
10.1126/sciadv.adp0443

2.2 Additional data highlighting the role of s-Opa1 (unpublished)

Mitochondrial dysfunction is one of the hallmarks of ageing, increasing mitochondrial stress and the need for quality control mechanisms. Opa1 levels decrease with age[160] which might contribute to age-associated deficiencies. Here we investigated the role of Opa1 processing in aged mice by documenting *Opa1v1* and *Opa1v1Δ4* mice until their natural death. We collected insights in the mitochondrial morphology and protein state in different tissues and analyzed the role and importance of the short form of Opa1 in more detail in MEFs isolated from these mice.

2.2.1 Depletion of Opa1 isoforms and inhibition of Opa1 processing sustains mitochondrial morphology but affects healthy ageing

To investigate the mitochondrial morphology in individual tissues of *Opa1v1* and *Opa1v1Δ4* mice, we crossed them with a reporter mouse with β-actin cre activated expression of YFP targeted to the mitochondrial matrix[161]. Perfused organs from 64-week-old mice were conserved in paraffin sections and further analyzed by confocal microscopy. *Opa1v1* mice only express the Opa1 isoform 1 which harbors the cleavage site for Oma1 (S1) but lacks the Yme1l cleavage site (S2). Figure 7A reveals that the absence of isoforms 3, 5, and 7 in *Opa1v1* mice results in normal mitochondrial morphology in heart, soleus muscle, brain, and liver. The same observations were made for the *Opa1v1Δ4* mice. In the absence of the short form of Opa1, no detectable differences in the mitochondrial network were apparent in the individual tissues. This data supports the previous findings of WT like mitochondrial morphology in these mice. To investigate the role of Opa1 processing in lifespan and age-associated diseases, we monitored the mice until humane endpoint and assessed the possible causes of death. We documented abnormalities and disease characteristics and plotted them for the corresponding genotype (Figure 1H). Up to 50 % of the mice developed recognizable tumors whereas a slightly higher tendency is detected in *Opa1v1 and Opa1v1Δ4* mice. Also, ulcerative dermatitis/hair loss and neurological disorders were more apparent in the Opa1-deficient mouse mutants. Additionally, we observed greater occurrence of ocular abnormalities in *Opa1v1* and *Opa1v1Δ4*. Since the protein is closely related to optic atrophy, a connection may exist. However, it must be noted that optic atrophy does not involve superficial change on the eye, but is only recognizable on the optic nerve itself. This area was not documented in our study.

Enlarged spleens were frequently found in WT and to almost never appear in the isoform and processing mutants. Splenomegaly typically develops when the hematopoietic or immune system is under chronic stress. The connection between this observation and Opa1 requires further analysis. Furthermore, signs of ascites and liver cirrhosis were found in our study. However, no direct correlation between the genotypes was observed in these cases (Figure S 5A). In addition to the lifespan (data published, Figure 1D,F and 3A), we also analyzed the heart/body weight ratio in very old age but detected no significant changes in males nor females (Figure 7C and D). Opa1 processing and protein abundance were assessed in heart tissue, comparing 12-week-old mice with animals at the end of their natural lifespan. In WT, there is a clear trend showing that Opa1 levels decrease with age (Figure 7E-H). However, due to the high standard deviation, the results are inconclusive, and more animals would be needed to refine the result. In the transgenic mice, decrease in Opa1 levels is less noticeable. Still, low molecular smears are prevalent in old animals clearly showing that the degradation is age associated and is potentially even enhanced in *Opa1v1Δ4* tissues. Nevertheless, this does not seem to have detectable physiological effects to the transgenic mice, since there is no significant difference in lifespan.

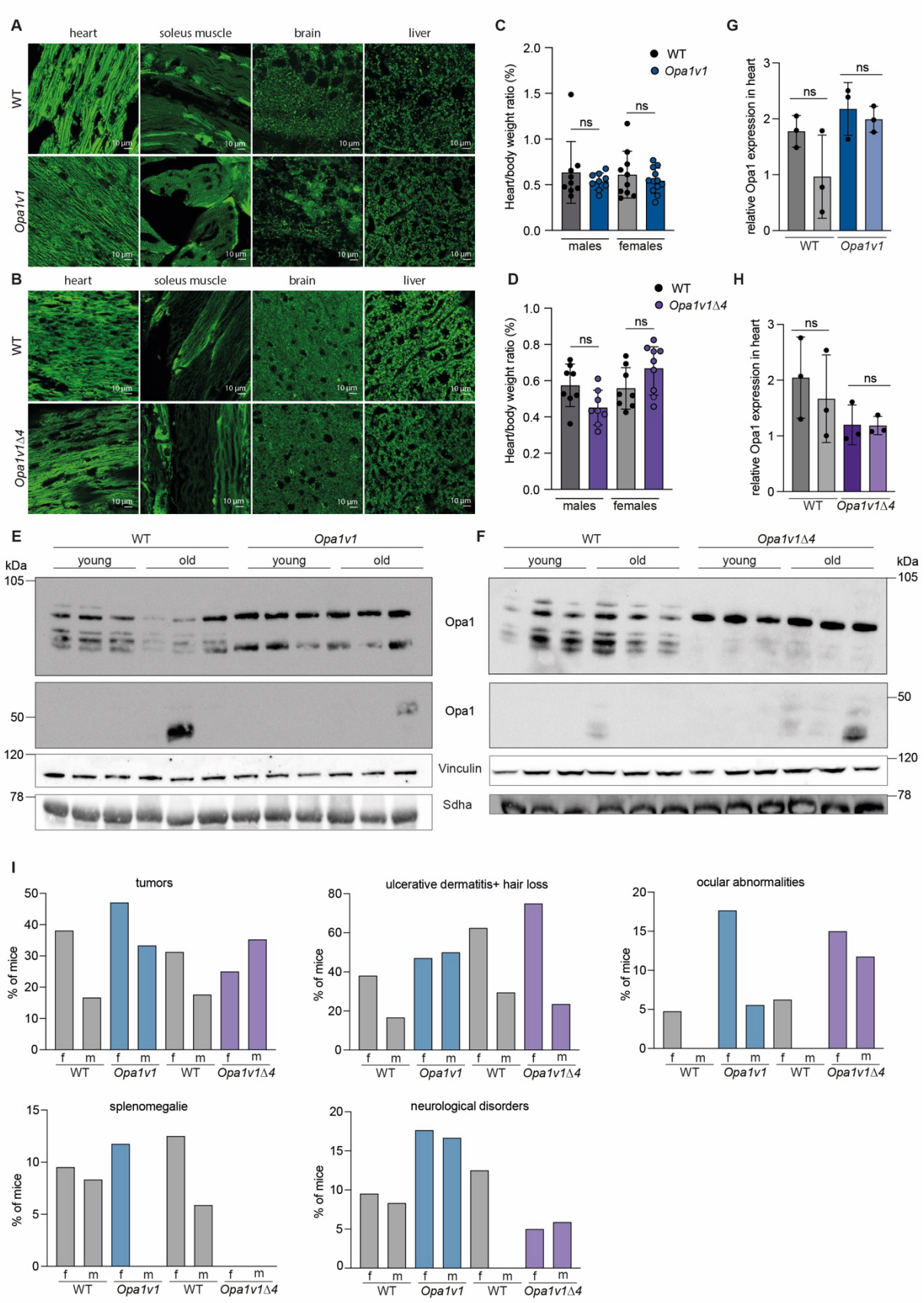

Figure 7: *Opa1v1* and *Opa1v1Δ4* show no detectable phenotype in different tissues but different disease associations in very old age. (A,B): Confocal images of endogenous mitoYFP-tissues in WT, *Opa1v1* and *Opa1v1Δ4* mice. 64-weeks old mice of each genotype (n=3) were perfused and the heart, soleus muscle, brain and liver were conserved in paraffin sections. Scale bar 10 µm. **(C,D)**: *Opa1v1* and

Opa1v1Δ4 mice show similar body weight gain as their WT littermates in very old age (natural death, C: males n=9, females WT n=10, *Opa1v1* n=12, D: males and WT females n=8, *Opa1v1Δ4* females n=9). **(E,F)**: Opa1 expression in heart tissues of WT, *Opa1v1* and *Opa1v1Δ4* in 12-weeks old mice and after natural death (n=3) and **(G,H)** bar-diagram representation of the relative Opa1 expression in heart normalized to vinculin. **(I)** Bar diagrams of observed age and disease-associated abnormalities in very old mice in WT^{Opa1v1} (female (f) n=21, male (m)=12, grey), *Opa1v1* (female (f) n=17, male (m)=18, light blue), $WT^{Opa1v1\Delta4}$ (female (f) n=16, male (m)=17, grey) and *Opa1v1Δ4* (female (f) n=20, male (m)=17, light violet).

2.2.2 Absence of Opa1 processing results in reduced respiration, OXPHOS complex and mtDNA levels

To investigate the role of s-Opa1 in mitochondrial function, we used WT, *Cox10*$^{-/-}$, *Cox10*$^{-/-}$*Opa1v1Δ4* and *Opa1v1Δ4* MEFs. All cell lines were derived from WT and *Opa1v1Δ4* mouse breeding. To obtain cre-independent *Cox10*$^{-/-}$ lines, we used CRISPR/Cas9-mediated gene editing. The WT and *Cox10*$^{-/-}$ cells show a normal Opa1 processing pattern, whereas only l-Opa1 accumulates in *Cox10*$^{-/-}$*Opa1v1Δ4* and *Opa1v1Δ4* MFEs (Figure 8A). Thus, expression of V1Δ4 results in efficient depletion of Opa1 processing *in vitro* and consequently to the absence of s-Opa1. First, we analyzed the levels of individual OXPHOS subunits by SDS-PAGE. As expected, a reduced level of the complex IV subunit CoxI was detected in *Cox10*$^{-/-}$ and *Cox10*$^{-/-}$*Opa1v1Δ4* MEFs. Mitochondrial respiration was accordingly drastically reduced in both mutants compared to the WT (Figure 8C). Interestingly, *Opa1v1Δ4* MEFs also showed reduced respiration providing first evidence that Opa1 processing supports functional respiration and the abundance of the OXPHOS subunits. Next, we analyzed the mitochondrial morphology. While WT and *Cox10*$^{-/-}$ exhibit an elongated network in PKmito ORANGE staining, *Cox10*$^{-/-}$*Opa1v1Δ4* and *Opa1v1Δ4* cells have a condensed structure with short-tubules that clusters around the nucleus (Figure 2G, Figure 8D and E). Furthermore, qPCR experiments revealed that loss of Opa1 processing in *Opa1v1Δ4* expressing heart results in reduced mtDNA (Figure 6G). However, only a tendency towards reduced mtDNA copy number could be observed in *Cox10*$^{-/-}$*Opa1v1Δ4* and *Opa1v1Δ4* MEFs (Figure 8H). Hence, mtDNA levels varied between the experiments, probably due to differences in the culture condition, leading to inconclusive results. We additionally stained the mtDNA with picogreen and counted the mtDNA foci in merged z-stack projection (Figure 8D and G). *Cox10*$^{-/-}$*Opa1v1Δ4* and *Opa1v1Δ4* both showed a clear reduction in mtDNA foci counts. Since Opa1 has been shown to co-localize with mtDNA and has been suggested to coordinate their replication[162] , we studied the mtDNA localization as a response to altered Opa1

processing. *Lewis et al*. (2016)[163] demonstrated that efficient replication of mtDNA occurs in regions of mitochondrial division that are in close proximity to the ER. Notably, mito-ER contact sites are altered in the *Opa1v1Δ4* background (Figure 2J-M). In addition, the localization of mtDNA is shifted towards the middle and tip of the mitochondria compared to WT (Figure 8 F). This implies that lack of processed Opa1 results in altered mtDNA replication. To further support this hypothesis, we performed an mtDNA repopulation assay. First, mtDNA was depleted to a minimum with ddC, with an additional recovery phase if 4 days. WT and *Cox10*$^{-/-}$ MEFs replenished their mtDNA levels to their starting levels in the short recovery period, whereas *Cox10*$^{-/-}$*Opa1v1Δ4* and *Opa1v1Δ4* MEFs struggle to replicate their mtDNA and fail to reach the initial level in the given time (Figure 8 I). This provides further evidence that processing of Opa1 or the presence of s-Opa1 is necessary for functional mtDNA maintenance.

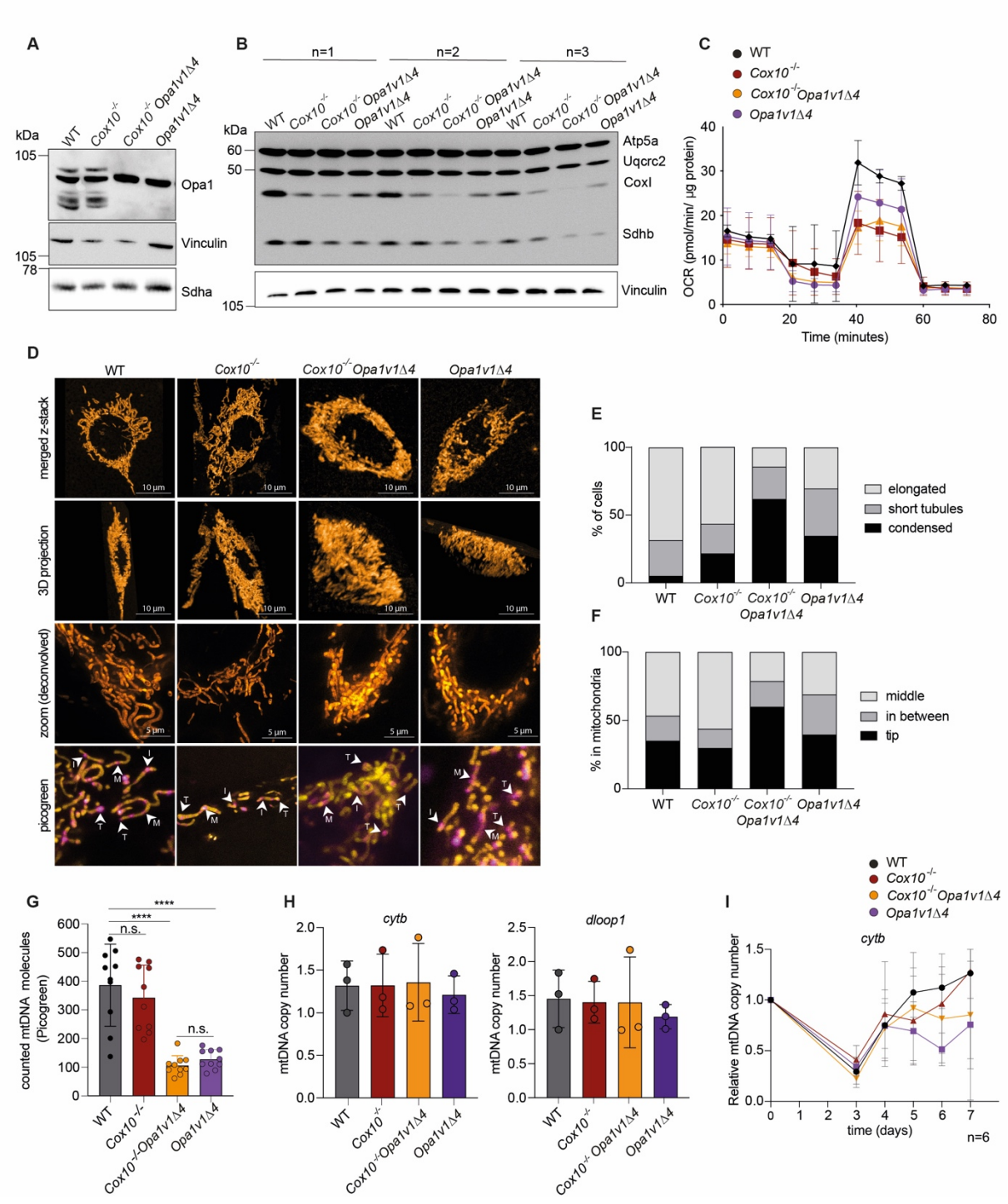

Figure 8: *Opa1v1Δ4* MEFs have lower respiration and altered mtDNA maintenance with a disturbed mitochondrial network. **(A)**: Opa1 processing pattern in WT, *Cox10*$^{-/-}$, *Cox10*$^{-/-}$*Opa1v1Δ4* and *Opa1v1Δ4* MEFs. **(B)**: Abundance of OXPHOS subunits in WT, *Cox10*$^{-/-}$, *Cox10*$^{-/-}$*Opa1v1Δ4* and *Opa1v1Δ4* (n=3). **(C)**: Oxygen consumption rate normalized to protein level in WT (black), *Cox10*$^{-/-}$(red), *Cox10*$^{-/-}$*Opa1v1Δ4* (yellow) and *Opa1v1Δ4* (purple). **(D)**: PKmito ORANGE staining of WT, *Cox10*$^{-/-}$, *Cox10*$^{-/-}$*Opa1v1Δ4* and *Opa1v1Δ4* MEFs in STED microscopy (scale bar 10 nm) with deconvolved zoom-in (scale bar 5µm) and picogreen staining. Location of mtDNA foci labeled with T=tip, M=middle, I=in between. **(E)**: Bar-diagram representation of morphology of WT (n=19), *Cox10*$^{-/-}$ (n=23), *Cox10*$^{-/-}$*Opa1v1Δ4* (n=23) and *Opa1v1Δ4* (n=42) MEFs in the subgroups elongated, short tubules and condensed. **(F)**: Bar-diagram representation of mtDNA location of WT, *Cox10*$^{-/-}$, *Cox10*$^{-/-}$*Opa1v1Δ4* and *Opa1v1Δ4* MEFs in the subgroups middle, in between and tip (n=10). **(G,H)**: Bar-diagram of counted picogreen stained mtDNA (n=10) molecules and mtDNA copy numbers (n=3) in WT (grey), *Cox10*$^{-/-}$ (red), *Cox10*$^{-/-}$*Opa1v1Δ4* (yellow) and *Opa1v1Δ4* (purple). Statistical significance was analyzed using

one-way ANOVA. **(I)**: Relative mtDNA copy number of 3 days ddC treated WT (grey), *Cox10*$^{-/-}$ (red), *Cox10*$^{-/-}$*Opa1v1Δ4* (yellow) and *Opa1v1Δ4* (purple) MEFs (n=6). Repopulation was allowed for 4 days after treatment.

2.2.3 Complementation with Opa1v5 rescues the mitochondrial network and increases the OXPHOS complex abundance and ISG response

In 2020, *Lee et al*.[164] published that cells which are unable to generate s-Opa1 are more sensitive to oxidative stress (e.g. H_2O_2). Cells expressing only l-Opa1 generate more superoxide and are less protected against cellular stress. To test this in the processing mutant condition of *Opa1v1Δ4,* we treated the MEFs with 500 µM H_2O_2 and monitored the cell death process. Contrary to the published results[164], l-Opa1-only cells (*Opa1v1Δ4* and *Cox10*$^{-/-}$*Opa1v1Δ4)* did not exhibit elevated cell death (Figure 9A). Rather, *Opa1v1Δ4* appeared transiently more protected (Figure 9B). In line with these results, when measuring cellular ROS production using mitoSOX dye, *Opa1v1Δ4* cells had similar ROS levels than WT cells, regardless whether they were growing in glucose- or galactose-containing DMEM (Figure 9C). These results clearly challenge the notion that s-Opa1 is essential in cell stress protection. Preliminary experiments from our lab identified Oma1 as an important player in mitochondrial innate immunity. We further investigated if these effects are mediated by Opa1 processing. In the *Opa1v1Δ4* background we observed a significant downregulation of different ISG-dependent genes. The genes *Ups18*, *Isg15* and *Ifi44* are among the most common ISG response genes upregulated in the cell[165-167]. However, in *Cox10*$^{-/-}$*Opa1v1Δ4* and *Opa1v1Δ4* MEFs we observed a strong downregulation of those genes already on a basal level (Figure 9D). To confirm these results, we cross-referenced selected ISG-dependent proteins in our whole proteome data set and were able to recapitulate the same pattern (Figure S 5B). Compared to WT, 14 identified proteins in the proteomics dataset were significantly downregulated in *Opa1v1Δ4* (in comparison, only 4 proteins are upregulated). To follow up on the previously generated results, we re-expressed Opa1 variant 5 in the *Opa1v1Δ4* MEFs via the stable cumate inducible gene expression systems. Figure 9F shows the successful integration of *Opa1v5* in *Opa1v1Δ4* MEFs and the dose-dependent expression of Opa1v5. It has been demonstrated that Opa1v5 is constantly cleaved by Oma1 and is thereby only present as short variant in mitochondria. The reason is not fully understood, but it has been assumed that the exon 4b encoded sequence is making the protein highly susceptible

to proteolytic cleavage[168]. Recent findings have shown that exon 4b harbors another alternative cleavage site, called S3, which can be recognized by Yme1l creating an intermediate band d' (Figure 9E)[168]. The western blot resolution in 9F is not enough to determine the exact band size and resolve whether we are looking at the band e resulting from the Oma1 cleavage or d' by Yme1l. Further evidence is needed to clarify the role of S2 and S3 processing in this case.

To study the role of s-Opa1 in regulating mitochondrial fitness, we checked on the morphology of the newly created cell lines. In z-stack images of PKmito ORANGE staining, both WT and *Opa1v1Δ4+v5* showed an elongated-flat mitochondrial network (Figure 9G). The perinuclear clustering of mitochondria in *Opa1v1Δ4* MEFs can therefore be rescued by re-expression of s-Opa1 (Figure S5D), an important indication that s-Opa1 plays an essential role in mitochondrial network organization. Similarly, the re-introduction of s-Opa1 partially restored subunit levels of the OXPHOS complexes I, III and IV (Figure 9H, S 5E). However, the maximum respiration capacity was not restored in *Opa1v1Δ4+v5* and *Opa1v1Δ4+v5* cells with 1x cumate.

We investigated in further experiments how re-expression of s-Opa1 affects the ISG response in *Opa1v1Δ4* cells. We added 5-FU (5-fluorouracil, nucleotide imbalance trigger) and monitored the ISG response. The treatment results in an upregulation of the known ISG marker genes and the phosphorylation of Stat1 (Y701P), an upstream mediator of the interferon gamma signalling pathway[169]. Nanostring results show that the WT cells actively respond to the 5-FU treatment whereas the basal levels and induced ISG response is reduced in *Opa1v1Δ4* MEFs (Figure 9K). The *Opa1v5*-complemented cells, show a partial rescue of the basal ISG response and a higher response to the 5-FU treatment in the Nanostring panel. Additionally, western blot confirmed the clear increase of p^{Y701}-Stat1 levels upon 5-FU treatment in WT cells (Figure 9J) but a blunted phosphorylation in *Opa1v1Δ4*. By reintegrating the variant 5 in those cells basal phosphorylation was rescued as well as the increase upon 5-FU treatment. This suggests that the mitochondrial dependent ISG response can be partially rescued by the addition of s-Opa1. Further experiments are required to understand how the presence of s-Opa1 contributes to the mechanism of the ISG response.

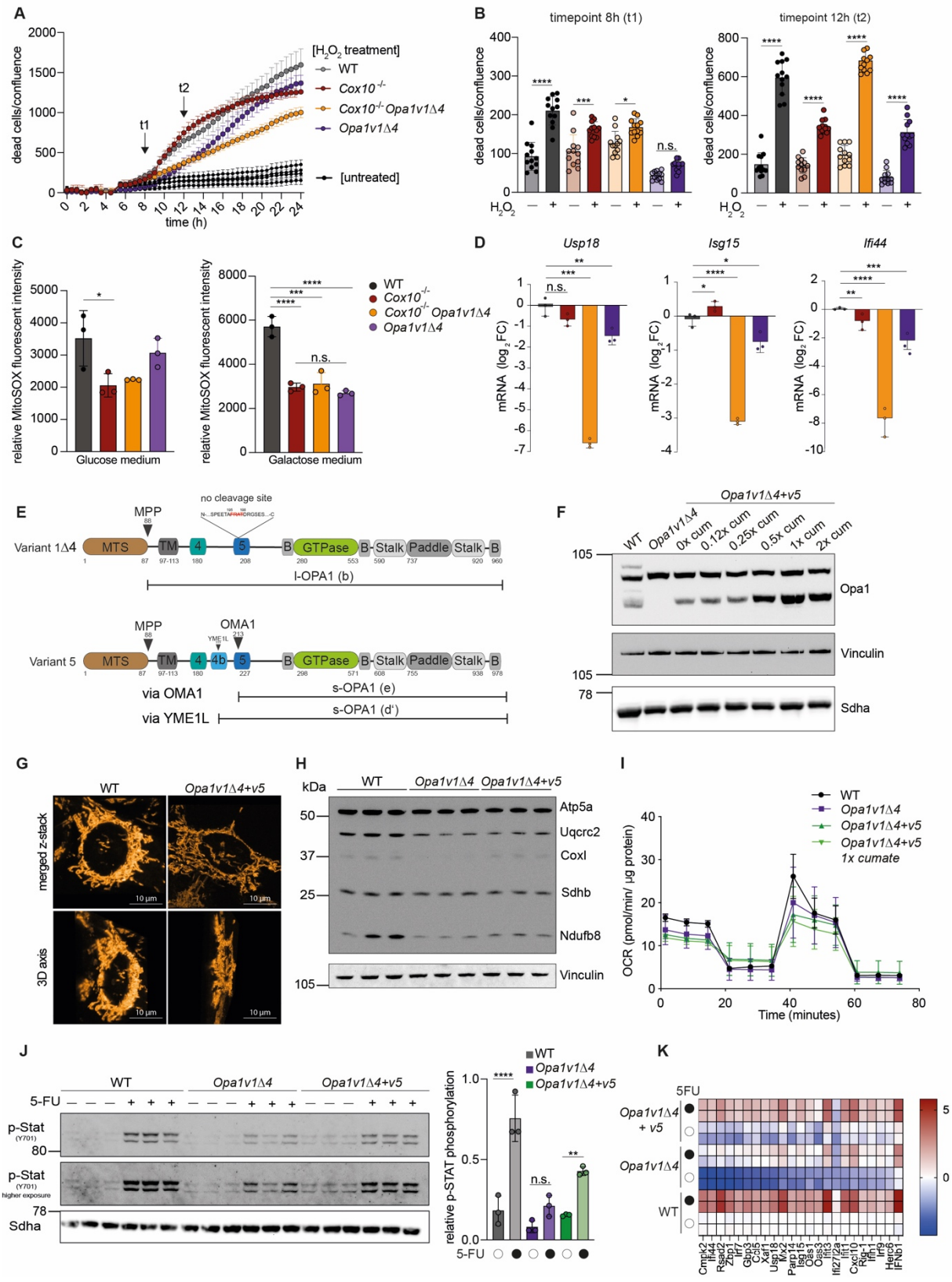

Figure 9: s-Opa1 has an effect on basal ISG response and is needed for a spread mitochondrial network and the OXPHOS subunit abundance. (A,B): WT (black), *Cox10*$^{-/-}$(red), *Cox10*$^{-/-}$*Opa1v1Δ4* (yellow) and *Opa1v1Δ4* (purple) MEFs were treated with 500 µM H_2O_2 and cell death was documented for 24 h. Bar-diagram presentation of the timepoints 8 h and 12 h after treatment. Statistical significance was analyzed using one-way ANOVA. **(C)**: Measurement of the relative MitoSOX fluorescent intensity in the used MEF set in glucose and galactose medium. **(D)**: Measurement of the basal ISG levels in WT (black), *Cox10*$^{-/-}$(red), *Cox10*$^{-/-}$ *Opa1v1Δ4* (yellow) and *Opa1v1Δ4* (purple) of n=3. Statistical significance

was analyzed using one-way ANOVA. **(E)**: Illustration of the domain structure of *Opa1v1Δ4* and *Opa1v5* and the respective cleavage sites of Yme1l and Oma1. **(F)**: Opa1 levels in WT, *Opa1v1Δ4* and *Opa1v1Δ4+v5* with cumate addition from 0x-2x. **(G)**: Z-stack projection of WT and *Opa1v1Δ4+v5* mitochondrial morphology in PKmito ORANGE staining imaged in STED microscopy. **(H)**: Abundance of OXPHOS subunits in WT, *Opa1v1Δ4* and *Opa1v1Δ4+v5* (n=3). **(I)**: Oxygen consumption rate normalized to protein level in WT (black), *Opa1v1Δ4* (purple) and *Opa1v1Δ4+v5* without and with 1x cumate (green). **(J)**: Levels of phosphorylated Stat-1 (Y701) in WT, *Opa1v1Δ4* and *Opa1v1Δ4+v5* with 16 h DMSO or 5 µM 5-FU treatment (n=3) normalized to Sdha. Statistical significance was analyzed using one-way ANOVA. **(K)**: Nanostring heatmap of ISG upregulated genes in WT, *Opa1v1Δ4* and *Opa1v1Δ4+v5* with16 h DMSO or 5 µM 5-FU treatment (n=2).

2.2.4 Proximity proteomics analysis reveals FAM210A as a potential specific interactor of s-OPA1

Although the cells engineered with the *Opa1v1Δ4* variant served as a powerful loss-of-function tool of s-Opa1, we next sought to directly assess the functions of s-Opa1 itself. Hence, we decided to investigate the close environment of the protein through APEX2-based proximity labeling proteomics. For this purpose, we took HEK293 cells which express MICU1-sOPA1-FLAG-APEX2 or the catalytically inactive protein MICU1-sOPA1^{K301A}-FLAG-APEX2 upon addition of tetracycline. After successful expression and APEX2-biotin-phenol oxidation, we performed immunoprecipitation experiments using antibodies directed against the FLAG-epitope and identified the potential interaction partners of s-OPA1 by mass spectrometry (Figure 10 A). A total number of 188 significantly enriched proteins were found in MICU1-sOPA1^{K301A}-FLAG-APEX2 vs. APEX2 and 240 potential interactors for the active s-OPA1 protein vs. APEX2 (Figure 10 B). Based on the documented interaction partners of OPA1 from the BioGRID database (https://thebiogrid.org/111024/summary/homo-sapiens/opa1.html), we highlighted these proteins in dark purple in the volcano plot analysis. Out of 229 potential interactors from the database, we found 169 in our dataset from which 41 are significantly upregulated hits which are likely to be s-Opa1 interacting partners. Figure 10C gives an overview (blue= significant in both, green= significant in MICU1-sOPA1-FLAG-APEX2, yellow= MICU1-sOPA1^{K301A}-FLAG-APEX2) of the potential candidates for s-Opa interaction partners. We were particularly intrigued by the protein FAM210A which came up as an interactor protein hit, with a log2FC of 7.44 exclusively in MICU1-sOPA1-FLAG-APEX2 (colored orange). FAM210A has known roles in cristae organization, mitochondrial biogenesis and interaction with Yme1l[155]. We deleted the *Fam210a* gene in WT MEFs using CRISPR/Cas9 to compare the phenotypes with those derived the *Opa1v1Δ4* MEFs (Figure 10F). Fam210a levels in WT, *Opa1v1Δ4* and *Opa1v1Δ4+v5* don't seem to different under basal conditions

(Figure S 5C). Conversely, the loss of Fam210a does not affect Opa1 levels or OPA1 processing, however a slight reduction of CoxI and Sdhb levels was detected. This goes along with other studies where it was shown that *in vivo, Fam210a*$^{-/-}$ reduces mitochondrial-encoded subunit complex levels[158] causing from impaired mitochondrial mRNA translation and proteostasis. Nevertheless, mtDNA levels are not affected by the loss of Fam210a (Figure S5G).

In a next step, we analyzed the morphology of the mitochondrial network in STED microscopy using PKmito ORANGE staining. Interestingly, *Fam210a*$^{-/-}$ partially mimicked the perinuclear clustering detected in *Opa1v1Δ4* cells (Figure 10D). In comparison to WT cells, 30 % more condensed mitochondria were found in *Fam210a*$^{-/-}$ MEFs (Figure 10E). This might suggest that Fam210a presence is also needed for maintaining the mitochondrial network. Lastly, we investigated the influence of Fam210a on the basal and active ISG response. Both untreated and after 16 h of 5-FU treatment showed no significant changes compared to WT MEFs. Fam210a is therefore not required for the ISG response. Further testing is needed to understand the physiological role of the interaction between Opa1 and Fam210a proteins and whether one protein is essential for the active role of the other.

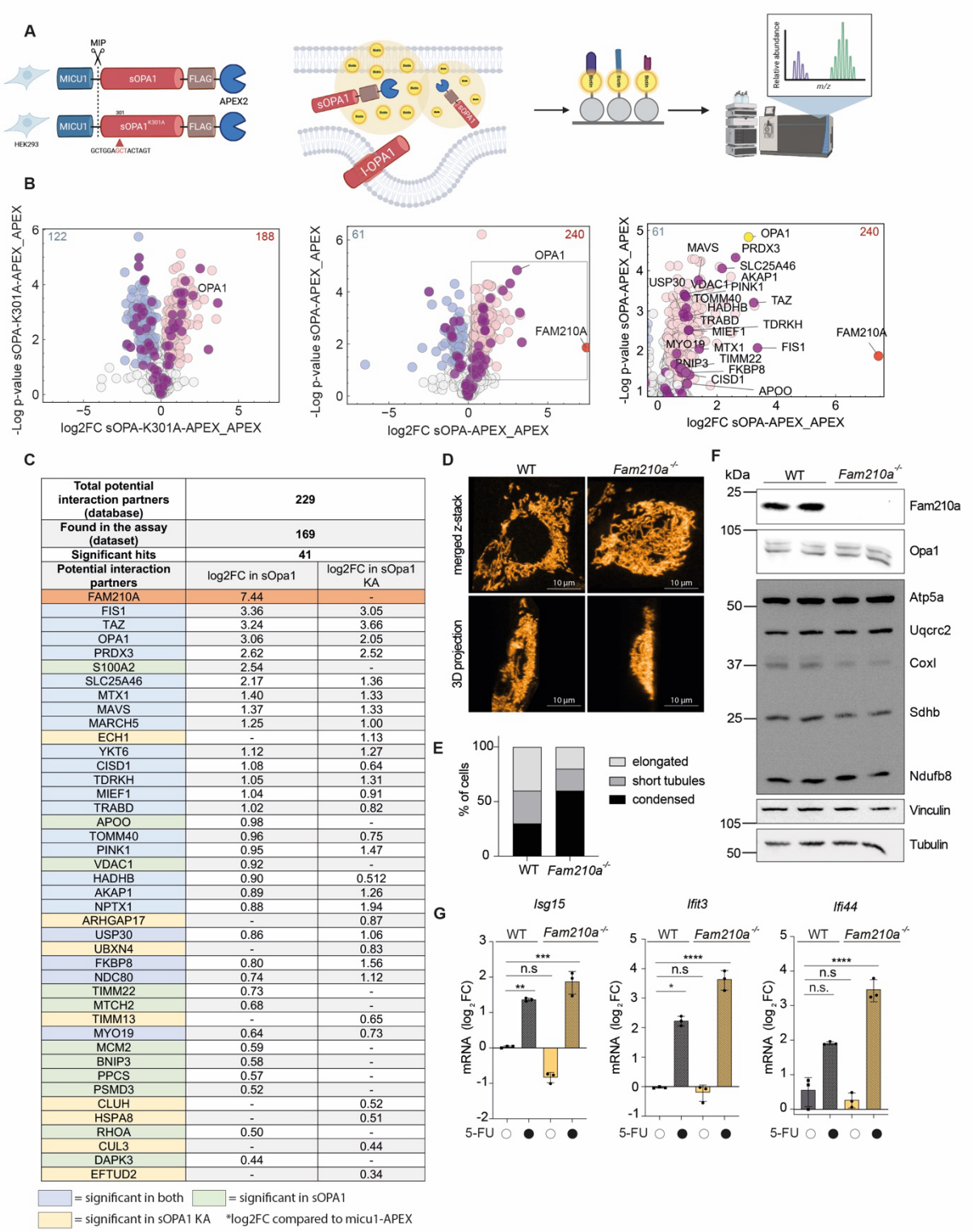

Total potential interaction partners (database)	229	
Found in the assay (dataset)	169	
Significant hits	41	
Potential interaction partners	log2FC in sOpa1	log2FC in sOpa1 KA
FAM210A	7.44	-
FIS1	3.36	3.05
TAZ	3.24	3.66
OPA1	3.06	2.05
PRDX3	2.62	2.52
S100A2	2.54	-
SLC25A46	2.17	1.36
MTX1	1.40	1.33
MAVS	1.37	1.33
MARCH5	1.25	1.00
ECH1	-	1.13
YKT6	1.12	1.27
CISD1	1.08	0.64
TDRKH	1.05	1.31
MIEF1	1.04	0.91
TRABD	1.02	0.82
APOO	0.98	-
TOMM40	0.96	0.75
PINK1	0.95	1.47
VDAC1	0.92	-
HADHB	0.90	0.512
AKAP1	0.89	1.26
NPTX1	0.88	1.94
ARHGAP17	-	0.87
USP30	0.86	1.06
UBXN4	-	0.83
FKBP8	0.80	1.56
NDC80	0.74	1.12
TIMM22	0.73	-
MTCH2	0.68	-
TIMM13	-	0.65
MYO19	0.64	0.73
MCM2	0.59	-
BNIP3	0.58	-
PPCS	0.57	-
PSMD3	0.52	-
CLUH	-	0.52
HSPA8	-	0.51
RHOA	0.50	-
CUL3	-	0.44
DAPK3	0.44	-
EFTUD2	-	0.34

= significant in both = significant in sOPA1
= significant in sOPA1 KA *log2FC compared to micu1-APEX

Figure 10: Proximity proteomics revels a potential interaction of s-OPA1 with FAM210A. (A): Illustration of the working model for the s-OPA1 proximity proteomics approach with biotinylating via the APEX2 protein. **(B)**: Volcano plot of the mass spectrometry data of MICU1-sOPA1^{K301A}-FLAG-APEX2 vs. APEX2 and MICU1-sOPA1-FLAG-APEX2 vs. APEX2 with indicated significant downregulated (blue) and upregulated (pink) proteins. Potential s-OPA1 interactors are marked in purple. **(C)**: List of potential interaction partners of s-OPA1 based on the entries of the database BioGRID which are found in the proteomics dataset (blue= significant in both, green= significant in MICU1-sOPA1-FLAG-APEX2, yellow= significant in MICU1-sOPA1^{K301A}-FLAG-APEX2). **(D):** Z-stack projection of WT and *Fam210a*$^{-/-}$ mitochondrial morphology in PKmito ORANGE staining imaged in STED microscopy. **(E)**: Bar-diagram representation of morphology of WT and *Fam210a*$^{-/-}$ MEFs in the subgroups elongated, short tubules

and condensed (n=10). **(F)**: Western blot analysis of Fam210a, Opa1, OXPHOS cocktail, Vinculin and Tubulin levels in WT and *Fam210a*$^{-/-}$ MEFs (n=2) **(G)**: Measurement of the basal and induced ISG levels via 5 µM 5-FU treatment (16 h) in WT (grey) and *Fam210a*$^{-/-}$ (yellow) MEFs (n=3). Statistical significance was analyzed using one-way ANOVA.

3 Discussion

The successful generation of *Opa1v1* and *Opa1v1Δ4* mice provided us a valuable tool to better understand the role of *in vivo* regulated proteolytic Opa1 processing. In combination with cultured MEFs isolated from these mouse lines, we gained insights into the basal and stress-induced functions of Opa1 splicing and processing. We were able to decouple some phenotypes previously associated with reduced or absent Opa1 processing in Oma1- or Yme1l-deficient models by manipulating the substrate rather than the proteases. We demonstrate that Opa1 processing is not essential for embryonic and adult development, but it plays a crucial role in mitochondrial quality control and adaptation to stress. Mechanistically, s-Opa1 formation is essential for maintaining OXPHOS subunit levels, mitochondrial network structure, mtDNA stability, and cellular stress response, including the ISG response. Nevertheless, *in vivo*, reduction of these functions only showed an effect under severe mitochondrial stress. The short variant is located at the cristae as an adjustable GTPase-tuner, thereby controlling adaptation mechanisms at the IM. In *Cox10*$^{-/-}$ mice, the lack of proteolytic regulation of Opa1 leads to an adaptation defect under severe OXPHOS deficiency. Cardiac hypertrophy in skeletal muscle and heart-specific *Cox10*$^{-/-}$ mice is blocked by inhibition of Opa1 processing, and lifespan is reduced by more than 2 weeks suggesting a protective effect of hypertrophic growth. Due to the loss of Opa1 cleavage, mitochondrial proliferation fails in myocytes as the balance between mitophagy and biogenesis is disrupted. We found further evidence that the absence of Opa1 variants and processing leads to unhealthy ageing. In old age, when mitochondrial dysfunction pressure increases, tumors as well as skin and neurological diseases tend to accumulate in *Opa1v1* and *Opa1v1Δ4* mice. This suggests that the individual isoforms play a role in specific tissues and that quality control suffers from a lack of Opa1 processing, resulting in pathological consequences.

Opa1 processing is dispensable in mouse development but is protective in mitochondrial cardiomyopathy

To understand the role of individual Opa1 variants and their processing in a physiological context, we generated a mouse model that express only the V1 isoform throughout the body via CRISPR/Cas9 genome editing (Figure 1). Due to the absence

of exon 5b, V1 lacks the cleavage site for Yme1l. Additional deletion of four amino acids (Phe^{193}-Thr^{197}) in the so-called “FRAT” region in exon 5 further impaired the Oma1-mediated processing of Opa1 in cultured MEFs (Figures 2B-D, 3). The block of processing was complete in the heart and liver as well as in BAT. However, in tissues such as the kidney and brain, Opa1 processing could not be completely inhibited (Figure 3D). Therefore, it is possible that potential phenotypes are suppressed and are not detectable with our models. We focused on the heart as cleavage inhibition was clearly visible and the energy-demanding tissue is highly dependent on functional mitochondria. Overall, the *in vivo* models revealed that that embryonic and adult development is not affected by the absence of multiple Opa1 isoforms and processing (Figure 1B-G, 2A-C). This fact is very interesting in itself, as tissues with a high sustained demand on OXPHOS normally use a finely tuned l/s-Opa1 ratio to ensure both efficient fusion and precise cristae organization. Notably, all mouse and human Opa1 isoforms possess exon 5, which harbors the cleavage site for Oma1 (Introduction Figure 3F). The conservation of this cleavage site during evolutions suggests important functions of Oma1-mediated proteolysis of the variants. In the mouse heart and skeletal muscle, isoforms 1 and 7 are highly expressed[170]. However, the loss of isoform 7 (harboring S1 and S2 cleavage sites) showed no effect in our mouse models, suggesting that Opa1 cleavage at S1 is sufficient to preserve functionality. *Opa1v1* or *Opa1v1Δ4* mice showed no phenotype associated with mitochondrial dysfunction based on defective Opa1 until one year of age (Figure S2). Similarly, impaired Opa1 processing did not cause additional phenotypes upon increased β-oxidation (in HFD) or under cold stress for 12 h (Figure 4). This contrasts *Oma1*$^{-/-}$ mice or mice lacking of Fam210a in the BAT, where the Oma1-stress axis or Fam210a-dependent cristae remodeling is defective and global metabolic flexibility is lost[66,155]. Although the phenotypes were attributed to missing or defective Opa1 processing in both models, our analysis shows that metabolic adaptation and cold-induced cristae remodeling do not depend on Opa1 processing, suggesting that impaired Opa1 processing is largely tolerable under mild stress conditions. In contrast, our analysis reveals a protective effect of Opa1-processing in cases of severe OXPHOS defects. The tissue-specific loss of Cox10, the heme A:farnesyl transferase assembly factor of cytochrome C oxidase[171], in cardiac and skeletal muscles leads to the disassembly of CIV and OXPHOS deficiency in cardiomyocytes.

Cox10$^{-/-}$ mice develop early-onset dilated mitochondrial cardiomyopathy with a lifespan of approximately 32 days[68]. Crossbreeding with *Opa1v1* results in the same pathological picture, demonstrating that the individual isoforms do not play a further role in OXPHOS-deficient cardiomyocytes (Figure 5B, D, E). *Cox10*$^{-/-}$*Opa1v1Δ4* mice, on the other hand, develop normally for the first two weeks but are visibly smaller, until they abruptly become less active and die shortly thereafter (Figure 5A, B). *Cox10*$^{-/-}$ stress leads to accelerated Opa1 processing by Oma1. It appears that l-Opa1 cleavage or the accumulation of s-Opa1 is crucial for undergoing the adaptive process of hypertrophy as age-matched *Cox10*$^{-/-}$ vs. *Cox10*$^{-/-}$*Opa1v1Δ4* hearts exposed reduced heart mass upon depleted processing. Regardless, RNA sequencing results revealed that hypertrophic signature genes are upregulated in both mice (Figure 5C-E, 6A). *Cox10*$^{-/-}$*Oma*$^{-/-}$ mice also show a worsening of the phenotype, however they were able to develop hypertrophic growth. Here, the cause of premature death lies in the lack of the Oma1-Dele1 axis, which is essential for ISR^{mt} activation[68]. *Ahola et al*.[68] identified that *Cox10*$^{-/-}$*Dele*$^{-/-}$ mice exhibit the same phenotype as *Cox10*$^{-/-}$*Oma*$^{-/-}$ mice, confirming the link that impaired ISR^{mt} activation increases the ferroptotic vulnerability, which ultimately leads to their rapid death. The ISR^{mt} response, however, is functional and active in *Cox10*$^{-/-}$*Opa1v1Δ4*, as ISR regulated marker genes and lipid peroxides are similar to those in *Cox10*$^{-/-}$ (Figure S3A-D). We found evidence that the lack of mitochondrial proliferation in *Cox10*$^{-/-}$*Opa1v1Δ4* myocytes is based on a disturbed balance of mitophagy and mitochondrial biogenesis. We detected autosomal structures and lipidated LC3 accumulation, which marks autosomal maturation (Figure 5G-J). In addition, the autophagy receptor p62 accumulates in heart lysates, indicating stalled mitophagy. In heart proteome analysis, we found overall decreased levels of mitochondrial proteins in *Cox10*$^{-/-}$ and *Cox10*$^{-/-}$*Opa1v1Δ4* hearts compared to WT, which were even more pronounced in the processing mutant (Figure 6B). Reduced mitochondrial mass already indicates limited hypertrophic cell growth. Bnip3 and Bnip3l mitophagy receptors accumulate while the mitochondrial phosphatase Pptc7, regulating mitophagy receptor stabilization, is reduced (Figure 6E). These findings further support a deregulation of mitophagy in *Cox10*$^{-/-}$*Opa1v1Δ4* hearts. In addition, we identified *Opa1v1Δ4*-dependent decreased levels of the nuclear respiratory factors Nrf1 and Nrf2 and of the estrogen-related receptor alpha (ERRα), as well as reduced mtDNA levels in *Cox10*$^{-/-}$*Opa1v1Δ4* hearts (Figure 6F,G). Taken together, these findings indicate additional dysregulation of mitochondrial biogenesis. Furthermore, in

ingenuity pathway analysis based on RNA-seq data, Cluh is most downregulated in *Cox10*$^{-/-}$*Opa1v1Δ4 vs. Cox10*$^{-/-}$ (Figure S4A). In doing so, the cell further shuts down post-transcriptional mitochondrial mRNA support, meaning that fewer mRNAs can be transported locally to the mitochondrial surface and translated efficiently. This intensifies the breakdown of mitochondrial proteins and the inability to supply new mitochondria (biogenesis block), as well as the failure to meet hypertrophic demand. These findings indicate additional dysregulation of mitochondrial biogenesis. Consistently, gene ontology enrichment analyses of *Cox10*$^{-/-}$ vs. *Cox10*$^{-/-}$*Opa1v1Δ4* heart proteome further revealed that nicotinamide adenine dinucleotide (NAD^+) metabolism, branched-chain amino acid (BCAA) metabolism, fatty acid oxidation, and mitochondrial ribosomes levels are reduced due to the lack of Opa1 processing (Figure 6C, D). Since BCAA metabolism and oxidation pathways are considered an essential source of energy in hypertrophic hearts, this indicates that *Cox10*$^{-/-}$*Opa1v1Δ4* hearts cannot manage the metabolic switch to hypertrophy, preventing hypertrophy and increased energy metabolism in myocytes under OXPHOS deficiency.

Loss of Opa1 isoforms and processing is vulnerable in severe stress and in very high age

Our analyses show that Opa1 processing in the heart is critical for the adaptation to cellular demands under severe stress, such as OXPHOS deficiency. Notably, we could find evidence for functional deficiencies or defective quality control and stress adaptation of *Opa1v1* and *Opa1v1Δ4* in very old age. Although our basic study until the age of 64 weeks found no effect, the extended aging study showed that although the mice all age similarly, they do so with varying degrees of health (Figure 7I). Our long-term studies with mice starting at around 100 weeks of age show a pronounced vulnerability for developing diseases and irritations. Initially, we observed age-related degradation of Opa1 in the heart[172], which was particularly prominent in the mice expressing V1Δ4 (Figure 7E-H). However, overall Opa1 levels are only reduced in aged WT, which still suggests a more unstable Opa1v1Δ4 protein although the expression levels are not affected in old age. The increased incidence of tumors, ulcerative dermatitis, ocular abnormalities and evidence of neurological dysfunction in old Opa1 mutants also might illustrate that the role of Opa1 cleavage extends beyond the described cardiac effects in *Cox10*$^{-/-}$ background. However, the effects are rather

mild and relate to a small cohort (n = 12–21), so the statements should be considered with caution. Skin irritations are often a sign of chronic inflammation, based on the fact that keratinocytes can no longer cope with the stress[173]. Similarly, splenomegaly associated with mitochondrial diseases often correlates with chronically elevated type I IFN and ISG activity[174]. Interestingly, this disease occurred only sporadically in *Opa1v1* and was absent in *Opa1v1Δ4* (Figure 7I) indicating a dampened systemic IFN signature. Without sustained IFN/NFκB drive, the classic myeloproliferative and inflammatory stimuli that lead to splenomegaly in old age are absent. This observation suggests that the effects of missing Opa1 isoforms and their processing in old age may occur in a tissue-specific manner. In conclusion, our findings suggest that loss of Opa1 isoforms and of Opa1 processing cause functional impairments with age. Considering that mitochondrial diseases usually manifest after a certain threshold has been exceeded, it is possible that the Opa1-dependent effects either manifest under direct severe stress, such as Cox10 depletion, or only after accumulation in very old age. In order to draw specific conclusions, the individual tissues requires closer investigation in future experiments.

S-Opa1 guarantees efficient IM communication for mitochondrial network distribution

Several reports show that l-Opa1 is essential for the actual fusion reaction at the IM, while s-Opa1 modulates l-Opa1 and fine-tunes the network morphology. Nevertheless, the expression of all individual human isoforms in *Opa1*$^{-/-}$ MEFs restores cristae morphogenesis and mtDNA levels[82]. In contrast, the human Opa1 variants which harbor exon 4b (Opa1 variants 3, 5, 6, 8) showing quantitative l-Opa1 cleavage and s-Opa1 accumulation, do not restore the fragmented mitochondrial network (Introduction Figure 3D,F)[82]. Consistent with the requirement of l-Opa1 for mitochondrial fusion[75], we show that mitochondrial fusion is not significantly impaired in *Opa1v1* and *Opa1v1Δ4* cells, which lack other Opa1 isoforms and additionally the Oma1 cleavage site (Figure 2E,F). Furthermore, we did not observe any impairment of cristae formation and density in hearts of the corresponding mouse lines nor in MEFs isolated from these mice, indicating that only the long Opa1 variant 1 is sufficient to maintain them (Figure 1J,K, Figure 2J, Figure 3G,H). The fact that the cleaved isoforms also restore the cristae shows that this is a general Opa1 function and processing does not

play a role. However, our TEM analysis does not distinguish between tubular and lamellar cristae in our studies. It has been shown that the coexistence of l- and s-Opa1 is essential for normal cristae morphology[93,175], as tubular cristae are decreased in l-Opa1-dominant cells and less dynamic remodeling takes place. We thus have to assume that the cleavage of Opa1 still finetunes cristae formation.

Exclusive expression of V1Δ4 result in a compromised mitochondrial network in MEFs (Figure 8D,E), consistent with a moderately decreased fusion rate in the absence of s-Opa1[75]. By re-expressing V5 we were able to rescue the perinuclear mitochondrial network (Figure 9G, S5D). V5 contains exon 4b and is quantitively converted into s-Opa1 by Oma1 cleavage (Introduction Figure 3F, Figure 9F)[168]. In contrast to l-Opa1, s-Opa1 lacks the membrane spanning domain and is recruited to membranes by its association with l-Opa1 and cardiolipin binding to its paddle domain. Notably, s-Opa1 indirectly stimulate l-Opa1-GTPase activity by stabilizing and forming hetero-oligomers[75,176]. In this way, s-Opa1 promotes the efficiency and range of IM fusion, allowing fusion to take place not only near the nucleus but along the entire mitochondrial network, which promotes a wide-ranging, continuous network. s-Opa1 may ensures efficient IM fusion, explaining why re-expression of Opa1v5 specifically enables the transition from a perinuclear cluster to a continuous network distributed throughout the cell. It remains to be investigated whether increased mito-ER contact sites in *Opa1v1Δ4* MEFs can also be restored by expression of Opa1 variant v5 (Figure 2J-M). Mito-ER contact sites are considered as hotspots for fission marking and Ca^{2+} transfer[131]. They mark mitochondrial fission sites and the initiation of mitophagosome formation[177]. Increased Mito-ER contacts may therefore reflect impaired mitochondrial fission and, concomitantly, mitophagy which may be halted at an early stage. This could explain why we found evidence of autophagic deficiencies *in vivo* and *in vitro*, leading to limited mitochondrial quality control. Referring to the changed LC3 lipidation and p62 levels (Figure 5I,I, Figure S 3K) as well as the accumulation of Bnip3 and Bnip3l and the downregulation of Pptc7 in *Cox10$^{-/-}$Opa1v1Δ4* hearts compared to *Cox10$^{-/-}$* (Figure 6E).

S-Opa1 as central mobile cristae partner to ensure translation and OXPHOS and mtDNA levels

Our *in vivo* data showed that the absence of Opa1 processing under basal conditions has no phenotype. Conversely, in isolated MEFs from this model, we detected moderately impaired ETC assembly with limited respiration and mtDNA maintenance (Figure 8B, C, G, I), which is most likely explained by threshold effects *in vivo* or altered stress conditions in our cultured cells. The re-expression of Opa1v5 shows a partial stabilization of OXPHOS complexes but does not restore the OCR (Figure 9H, I, S5E). Assuming, that the integration of Opa1v5 promotes IM fusion and network elongation, fusion also promotes mixing of mtDNA molecules and distribution of nucleoids across the network[178], which supports high mtDNA replication rates (and thereby OXPHOS subunit levels). Conversely, cristae remodeling can be completely decoupled from fusion activity showing optimized respiratory chain supercomplex assembly through a defined balance of long and short Opa1[93]. It might be, that this balance is still not given in *Opa1v1Δ4+v5* cells. Additionally, Opa1v1Δ4 cleavage mutant continues to be expressed in this MEF model, which may prevent optimal IM adaptation through blocked processing. Cleavage of l-Opa1 might therefore be necessary for successful supercomplex formation and respiration. Another possibility is that the elevated OXPHOS protein levels, which still don't reach WT levels, are not enough to guarantee supercomplex formation.

We observed a reduction in mtDNA content dependent on *Opa1v1Δ4* in the hearts and via nucleoid staining in MEFs (Figure 6G, 8G) what can be the consequence of reduced mitochondrial biogenesis due to a lack of Opa1 processing. On the other hand, we found decreased ability of mtDNA repopulation upon mtDNA depletion with ddC in *Cox10$^{-/-}$Opa1v1Δ4 and Opa1v1Δ4* MEFs (Figure 8I). Silencing of the exon 4b variants leads to significant mtDNA depletion, suggesting a disruption of mtDNA replication and nucleoid distribution[81]. It is likely that expression of only isoform V1 is not sufficient for mtDNA replication and V5 integration (containing exon 4b) stabilizes the levels in cultured MEFs. Opa1v5 could provide additional scaffold structures in the IM, allowing nucleoids to be distributed equally along the network and the mtDNA copy number per nucleoid and per mitochondrion remains stable. Furthermore, s-Opa1 reintegration allows a spread mitochondrial network in *Opa1v1Δ4*, which supports the maintenance of the stoichiometry of the protein components of the mtDNA replisome and mtDNA

itself. Evidences that this does not happen in the V1Δ4 expressing cells is shown by the mislocalization of nucleoids to the middle and the tip of the mitochondria (Figure 8D,F). However, this observation might also be explained by altered mito-ER contacts and mitochondrial dynamics in *Opa1v1Δ4* cells. Studies indicate that the ER marks not only fission sites but also mtDNA replication sites on the mitochondria[163]. This demonstrates the dual necessity of s-Opa1 presence in the cell. Restoration of the network and contact sites would also be beneficial for mtDNA replication. In the future, mtDNA rescue experiments with *Opa1v1Δ4+v5* should be performed to provide further insight.

Oma1-mediated Opa1 processing in cellular stress adaptation

Various stress conditions, such as oxidative stress, heat stress, protein stress or OXPHOS deficiencies activate Oma1, leading to increased l-Opa1 processing and the mitochondrial fragmentation due to ongoing fission events[179]. This early stress step is central for the adaptation of mitochondrial dynamics to outer influences and can affect both survival and death. In *Opa1v1Δ4* MEFs, l-Opa1 remains stable, ROS production is reduced, and we detect moderately delayed H_2O_2 cell death (Figure 9A,B), suggesting that these cells appear to be better protected at the first glance. Nevertheless, it can also be interpreted as a sign of an inadequate response to stress. The parallels can be seen in the lack of adaptation of hypertrophic growth *in vivo*, which initially seems as protection but ultimately leads to a reduced lifespan with impaired stress adaptation. The fact that we see less ROS production in the *Cox10*$^{-/-}$ and *Opa1v1Δ4* MEFs presumes a model in which reduced OXPHOS function throttles the overall electron flow by relying more on glycolysis, thereby reducing the number of potential leakage sites (Figure 9C)[180]. Galactose culturing forces cells to produce ATP predominantly via the mitochondria. In WT cells, this leads to higher OXPHOS throughput and thus potentially more electron leakage and ROS production[71]. In *Cox10*$^{-/-}$ and *Opa1v1Δ4* however, OXPHOS is limited, the entire ETC flow is reduced, respectively, even if cells are grown in the presence of galactose as sole carbon source[181], resulting in less ROS production even when the cells are bioenergetically stressed. Nevertheless, this assumption is rather controversial and must be handled with caution, as OXPHOS deficiency is typically associated with increased ROS production. Taking into account that ROS is mainly generated at complexes I and III[182],

those levels are downregulated in *Opa1v1Δ4* MEFs supporting the assumption of general lower electron flow (Figure 9H, S5E). It should be noted that ROS production is not generally considered as harmful, as they also act a signaling molecules[180]. In *Opa1v1Δ4* cells, reduced mitochondrial ROS might attenuates redox-dependent input into the NF-κB signaling cascade, which may result in diminished or delayed NF-κB activation and consequently a blunted ISG program[183,184]. NF-κB and cGAS-STING are closely connected in the innate immune response: cGAS-STING activates NF-κB, and conversely, NF-κB can modulate the strength and duration of STING signals[185]. In fact, *Opa1v1Δ4* cells lacking s-Opa1 exhibit a blunted ISG response and lower level of phosphorylated Stat1 (Figure 9J,K). We inhibited the thymidylate synthase by 5-FU treatment, causing dNTP pools imbalance. This leads to replication stress, single- and double-strand breaks, and incorrect repair resulting in DNA fragments and R-loops that are released into the cytosol and causing an ISG response which in turn is also promoted by ROS-driven membrane damage or pore formation[186,187]. The suppressed basal and active ISG response in the *OPA1v1Δ4* cells is consistent with lower ROS peaks (lower NF-κB signaling) and more delocalized nucleoids (Figure 8F) bringing less mtDNA into the cytosolic space and thus downregulating the IFN tone, while WT cells with a normal Oma1-Opa1 stress axis generate more such DAMP signals. However, it must be clearly stated that we have not investigated any further evidence of reduced NF-κB signaling upon depleted Opa1 processing. Opa1v5 reintegration rescues the ISG response to some extent, which may have several causes in the processing-deficient background: Broadening the network and distributing nucleoids across more tubuli, or generating subtle changes in cristae structure and supercomplex organization, which again allow sufficient ROS/mtDNA signals for normal ISG activation without excessively damaging the cells. Further investigation is needed to determine whether the DAMP release mechanism differs between WT and *OPA1v1Δ4*. In our proximity proteomics data set, MAVS (mitochondrial antiviral signaling protein) was another hit in relation to s-Opa1 interaction (Figure 10C). MAVS is an adapter protein of the innate immune response that sits on the OM membrane and translates antiviral signals into interferon responses. Upon activation, MAVS oligomerizes and recruits kinases (e.g., TBK1, IKK), leading to the activation of IRF3/IRF7 and NF-κB[188]. This hit links s-Opa1 to zones where mitochondrial morphology and antiviral stress signals are directly coupled. The consistent picture is that Oma1-dependent Opa1

processing is important for adjusting the level of mitochondrial stress signals to guarantee and adequate response.

The interactome profile of s-OPA1: Fine-tuner at the IM

Previous cryo-electron tomography and reconstruction data emphasize that the central, mechanistically defined partners of OPA1 are cardiolipin, OPA1 oligomers themselves, MICOS components, the regulatory proteases YME1L and OMA1 and a cooperation with MFN1/2 to ensure the common fusion model[72,94,189]. For l- and s-OPA1, there are hardly any known separated interactors. The partners are relevant for both forms, with different contributions. S-OPA1 possesses all functional domains of large GTPases and its structure is highly conserved[76] and to date, s-OPA1 has not been assigned a role independent of l-OPA1. Therefore, we created an interactome profile of s-OPA1 tagged with APEX2 labeling approximately 20 nm surrounding of the protein (Figure 10A and B)[190]. This study is also limited in the fact that we cannot exclude the possibility that l-OPA1 also communicates with the identified interactors, or that the interaction only takes place in the (hetero-)oligomeric state. Accordingly, the interactors might be specific for OPA1 but not specific for its processed form. Nevertheless, our study distinguishes the role of GTPase activity in potential interactions by comparing s-OPA1 with s-OPA1^{K301A}, the catalytically inactive form.
We found 41 significant hits, 22 of them mostly belonging to the top hits, appeared for both the active and inactive s-OPA1 tagged protein. 12 hits were exclusively significant for the GTPase-active s-OPA1 variant and 8 for s-OPA1^{K301A}. Almost all of these hits belong to the low confidence interaction partners (>1 log2FC). The overlap of most top hits between s-OPA1 and s-OPA1^{K301A} indicates a GTPase-independent proximity defined by membrane association and oligomeric scaffolding rather than by the specific GTP reaction. Initially, OPA1 itself was among the most prominent hits in active and inactive Opa1 probes, confirming that s-OPA1 forms oligomers (with l- and s-OPA1) to ensure efficient fusion and membrane tubulation[75]. We categorized the other hits into 5 classes depending on their localization and common function (Figure 10C). The first class locates processed s-OPA1 to energy-rich cristae “hubs” indicated by the close proximity to tafazzin, a cardiolipin remodeling enzyme associated with Barth syndrome [191,192], MIC26 (a subunit of the MICOS complex)[193], and proteins that are functionally coupled to cristae-associated processes (ECH1, ECHB, PRDX3, HADHB)[194-196]. All

four proteins are matrix enzymes involved in fatty acid oxidation/redox control and are functionally located close to the IM. However, direct contact with s-OPA1 is not possible, which merely reflects the immediate proximity of the OPA1-rich IM to the matrix. Recent studies have shown that PRDX3, the major counteractor for H_2O_2, is also present in the IMS, where it plays a key role in limiting H_2O_2 diffusion into the cytosol[196]. In general, OPA1 is distributed across the entire inner mitochondrial membrane and is located both at the inner boundary membrane, which is parallel and directly opposite the OM, and at the cristae membrane[197]. L-OPA1 is anchored in both subdomains, while the cleaved s-OPA1 forms remain soluble in the IMS, where it continues to interact with the IM at cristae and CJs. The presence of the class 1 proteins in the s-OPA1 proximity environment suggests that s-OPA1 is preferentially located in regions/cristae with high fatty acid oxidation and NADH/$FADH_2$ production, close to β-oxidation hotspots. A possible role of s-OPA1 could be a “structural tuner” that controls cristae geometry and supercomplex organization so that β-oxidation run efficiently and ROS production is controlled, thereby helping to regulate the functional energy space of the cristae.

The second class comprises a series of OM fission regulating proteins, which indicates that s-OPA1 might play an active role in OM dynamics and fission as well. Examples include potential interactions with FIS1, MID51 MARCH5, AKAP1, and SLC25A46[198-202]. The first two hits are direct DRP1 receptors (fission receptors). The other proteins also modulate dynamics by regulating DRP1 and marking fusion and fission events. For example, MARCH5 could determine when and where fission is triggered by ubiquitinating OM dynamic proteins. S-OPA1 might simultaneously remodel the IM to ensure that these events proceed in an energetically and structurally efficient manner[199]. However, interaction with these OM proteins is primarily plausible via shared contact points and substrate-complexes, rather than via direct and stable bindings. Nevertheless, there is a strong correlation between the accumulation of s-OPA1 and network fragmentation. S-OPA1 is primarily described as a co-regulator of fusion, although at high concentrations or in the wrong l/s ratio, it actively support fission by coupling IM remodeling with DRP1 fission hotspots, thereby promoting network fragmentation[203]. S-OPA1 creates a fusion-incompetent state, thereby facilitating fission labeling. This function would explain why s-OPA1 colocalizes with the various OM fission proteins.

The third class includes numerous mitophagy sensors and proteins from the ubiquitin-proteostasis system: BNIP3, PINK1, and FKBP8 are all OM proteins that are involved in the decision to preserve the organelle, undergo mitophagy, or cell death, thus representing typical quality control mechanisms[204-206]. Another potential s-OPA1 interactor is YKT6, which is not primarily located on mitochondria but may be indirectly functionally coupled with s-OPA1 via autophagy/mitophagy processes. YKT6 forms a fusion complex on autophagosomes for lysosome fusion, making it essential for the final stage of mitophagy as well[207]. These findings are particularly interesting in the context that we found evidence for impaired mitophagy and dysfunctional autophagosome formation in s-OPA1 depleted hearts and MEFs. Also altered mito-ER contact sites upon loss of OPA1 cleavage in MEFs indicate, that the generation of s-OPA1 could be an essential factor in sustaining controlled mitophagy. The question arises whether s-OPA1 plays an active role in this process or if the OPA1 cleavage represents more an upstream event. So far, it has only been shown that the loss of the long, membrane-bound OPA1 variant promotes mitophagy by limiting fusion and facilitating fragmentation of damaged mitochondria[78]. Here, a link could be made to class 2 proteins and the findings from *Anand et al.*[203], which indicate that s-OPA1 might also have an active role in the fission process. USP30, PSMD3, and VDAC1 define which damaged mitochondria are targeted for ubiquitination and mitophagy and how easily metabolites, ROS, and possibly mtDNA is entering the cytosol[208-210]. HSPA8 recognizes ubiquitinated or misfolded OM proteins, organizes their disaggregation, and supports the recruitment of the autophagy apparatus[211]. If s-OPA1 is located directly at such OM domains, it could modulate cristae opening in a way that the amount of released material arriving at VDAC1-rich OM regions is controlled. This assumption is consistent with the published results that OPA1 limits the amount of cytochrome c and other pro-apoptotic factors by keeping CJs narrow[94]. Loss of OPA1 or its stress-induced inactivation leads to BAX/BAK- and BH3-dependent cristae opening and widening, thereby facilitating increased release of cristae stored material[94,212]. Hereby, the appearance of l-/ and s-OPA1 is essential for efficient cristae remodeling[95]. Compared to the membrane-bound protein, the presence of s-OPA1 makes the cristae more flexible and allows an appropriate adaptation to the environment. This assumption can also be linked to the reduced H_2O_2 sensitivity in *Opa1v1Δ4* MEFs, which confirms that OPA1-dependent cristae remodeling plays a decisive role in cell death signaling[95]. Thus, s-OPA1 could

indirectly determine whether a stressed mitochondrion is classified as still reparable or is sent toward mitophagy or if direct cell death takes place.

The proximity analysis identified cytoskeleton-related proteins, such as S100A2, RHOA, ARHGAP17, and Myosin XIX in proximity to s-OPA1. These proteins regulate actin organization, cell migration and the subcellular distribution of organelles, thereby localizing s-OPA1 to areas that control the positioning and shuttling of mitochondria. In this context, mitochondrial shape is controlled not only by classical fission and fusion factors, but also by actin filaments and motor protein mediated transport processes. RHOA and ARHGAP17 actively control the dynamics of the actin cytoskeleton, stress fibers, and protrusions[213,214], and S100A2 acts as a Ca^{2+} sensitive protein that can modulate RHO signaling pathways and thus influence actin organization and cell migration[215]. The co-presence of Myosin XIX, a motor protein that transports mitochondria along actin filaments[216], with s-OPA1 suggests functional clusters that are closely linked to the actin cortex, protrusion zones, and other contact areas of the cell periphery. In this context, s-OPA1 can be interpreted as an integral component of a positioning module that couples internal membrane architecture with external membrane dynamics and actin-dependent motility. In zones where RHO/actin signaling pathways are active, s-OPA1 could ensure that mitochondria fuse efficiently and remain functionally competent, to ensure an active distributed throughout the cell to the periphery or back to perinuclear regions as needed. However, it should be noted that the interaction of s-OPA1 with these proteins can only be explained by OM bridge proteins or contact zones and not by direct contacts. For example, so-called actin cages often form at mito-ER contact sites, where mitochondria are anchored via OM receptors and motors (e.g., Myosin XIX)[217]. Actin cages, in turn, are an important component of quality control and mitophagy, as they trap damaged mitochondria so that their contents remain confined[218]. This observation is also consistent with the above-mentioned proteins that actively couple s-OPA1 to mitophagy and the fission machinery.

The fifth class links s-OPA1 with central elements of mitochondrial translation and transcription. Particularly striking is the strongly enriched interaction with FAM210A, an IM protein that directly intervenes in the control of translation of mitochondria-encoded OXPHOS subunits and the maintenance of mitochondrial proteostasis[157]. In addition, this hit was only found in the active s-OPA1-tagged sample and was not detected in s-

OPA1^{K301A}. The fact that mitochondrial translation takes place in the matrix makes the identification of FAM210A as an IM protein even more interesting, as it links the process to the IMS and s-OPA1. FAM210A is enriched in cristae domains, where respiratory chain complexes and translation machinery coexist. It is described as a scaffold protein in the IM that binds to the mitochondrial elongation factor EF-Tu in the matrix, thereby modulating the translation elongation of mitochondrial-encoded mRNAs[159]. Loss of FAM210A results in decreased mitochondrial encoded proteins (like OXPHOS complex subunits) and respiration and a lower number of mitochondria with less cristae integrity[157]. We also confirmed lower mtDNA encoded CoxI levels in our *Fam210a*$^{-/-}$ MEFs (Figure 10F). FAM210A remodels cristae by influencing the l/s-OPA1 ratio via interaction with YME1L which in turn regulates OMA1 activity[155]. Since FAM210A affects the presence of s-OPA1, it might be that the two proteins promote each other's functionality. The pronounced spatial proximity of s-OPA1 and FAM210A might suggest that s-OPA1-rich cristae domains are preferred platforms for FAM210A-mediated translation processes. Conversely, FAM210A could indirectly support the function of s-OPA1 by ensuring balanced synthesis of mitochondrial-encoded RC subunits, thereby creating a bioenergetic state that promotes the formation and stability of OPA1 oligomers, cristae compaction, and the integration of import proteins. The absence of s-OPA1 in *OPA1v1Δ4* cells could mimic a FAM210A-deficient state, assuming that one protein needs the other to function. With the loss of the s-OPA1-FAM210A axis, *OPA1v1Δ4* cells might exhibit reduced translation, which is reflected in decreased OXPHOS complex levels and respiration. The partial restoration of OXPHOS levels in *OPA1v1Δ4+v5* could therefore also be explained by a more effective translation through re-expressing the co-player (s-OPA1) of FAM210A.

The additional interactions with CLUH and TDRKH support the colocalization of s-OPA1 with transcriptional and translational active regions: CLUH is predominantly localized in the cytosol, but is closely positioned to mitochondrial surfaces and microtubules. It forms cytosolic RNA granules and selectively binds mRNAs of nuclear-encoded mitochondrial proteins inclusive many OXPHOS components[219]. TDRKH is also coupled to mitochondria-associated RNA-rich compartments and links RNA-complexes to the mitochondrial surface[220]. Findings in the gene expression profile of *Cox10*$^{-/-}$*Opa1v1Δ4* and *Cox10*$^{-/-}$ hearts identified Cluh as most significantly down-regulated upon inhibition of Opa1 processing (Figure S4C). Loss of Cluh results in

downregulation of mitochondrial proteins and biogenesis and the mitochondria cluster around the nucleus[219]. Precisely the phenotype we observe in the isolated MEFs that express exclusively *Opa1v1Δ4* (Figure 8D, E). Furthermore, mitochondrial ribosomes are downregulated in processing depleted hearts as well, which further inhibits mitochondrial translation (Figure 6C, D). These observations fit with the assumption that s-OPA1 is spatial proximity with the CLUH and (in-)actively participated in the transcription and translation machinery in mitochondria. Moreover, it could explain why the loss of Opa1 cleavage in mice leads to a block in mitochondrial biogenesis upon severe stress. CLUH granules enables local translation and co-translocation of mitochondrial proteins[221]. This thesis is supported by the hits TOMM40, TIMM22, TIMM13, and MTX1, locating s-OPA1 to import hotspots between the outer and inner membranes where newly imported carriers, IM proteins, and cristae components arrive and are integrated into the architecture[222]. MTX1, for example, is important for the import of nuclear-encoded mitochondrial proteins and for the assembly of OM proteins, which is particularly relevant for the biogenesis of the respiratory chain and CJs[223]. Together with the proximity to the (co-)translational machinery, s-OPA1 could thus indirectly influence ETC capacity and ROS profiles.

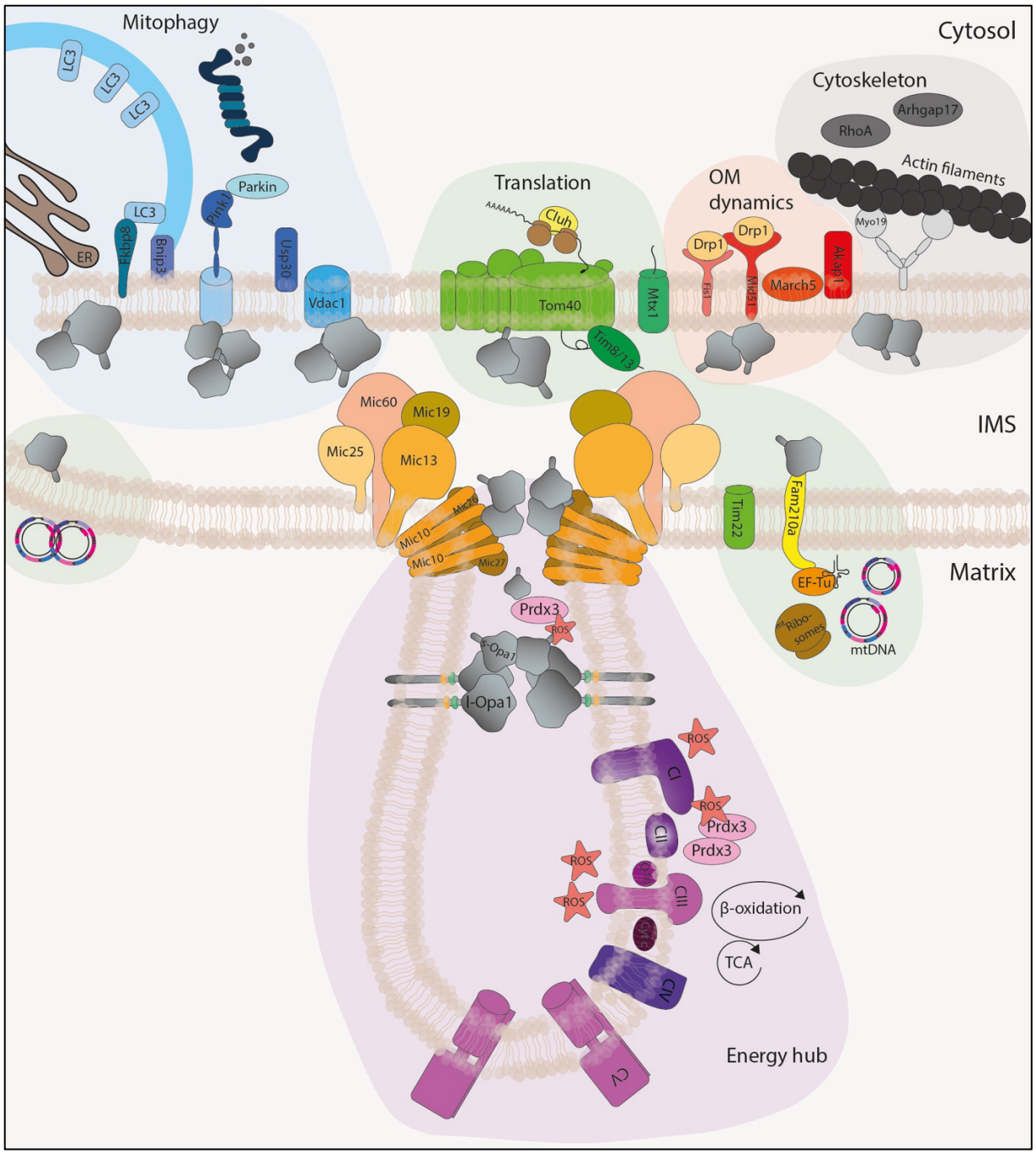

Figure 11: Overview of the identified impact clusters of s-Opa1 based on the proximity proteomics dataset. Divided into the groups energy hub (purple), translation (green), mitophagy (blue), OM dynamics (red), and actin cytoskeleton (grey)

Future perspectives

In this thesis, we have demonstrated that the loss of Opa1 processing results in disrupted mitochondrial biogenesis and deregulated mitophagy, which leads to pathological manifestations under severe OXPHOS stress and in old age. It remains unknown to what extent these effects are dispensable in basal conditions and under

mild stress, to understand which threshold is exceeded to observe a physiological relevance for Opa1 processing. An undiscovered tissue-dependent phenotype can also not be excluded, as our focus was on characterizing the underlying processes in the heart. Therefore, the characterization of *Opa1v1* and *Opa1v1Δ4* mice needs to be extended to other tissues in order to obtain an overall picture. For future studies, the generation of an additional knock-in mouse line expressing *Opa1v1Δ4+v5* would be useful. Within this model, uncleavable l-Opa1 continues to be expressed, but the additional integration of the V5 isoform allows the expression of s-Opa1 based on constant Oma1 cleavage. By generating this model, accurate statements about which effects are attributed to the processing of the long V1 isoform and which rely on lack of Oma1-mediated s-Opa1 generation.

The presence of s-Opa1 is essential for mitochondrial adaptation to cellular demands through guaranteeing efficient IM fusion and cristae remodeling. Via *in vitro* studies, we gained indications that s-Opa1 modulates the cristae to ensure optimal translation and adaptation to stress response. Greater investment in the interplay between Fam210a and s-Opa1 would be valuable for the mitochondrial research field. The fact that the proximity hit was only found with the active s-Opa1 protein and its IM localization makes Fam201a to a promising candidate. It is conceivable that s-Opa1 binds to Fam210a on the IMS side and initiates a conformational change that makes Fam210a accessible for binding to matrix proteins such as EF-Tu. This could explain possible phenotypes such as reduced OXOPHS protein levels and respiration in s-Opa1-deficient cells. For the future, it would be of great interest to determine whether this could be the first active role of s-Opa1 that has remained hidden until now.

4 Materials and Methods

4.1 Materials and methods from results section 2.1 (published article)

See results section page 48-51.

4.2 Materials and methods from results section 2.2

4.2.1 Materials from section 2.2

Table 2: Materials from section 2.2

Reagent or resource	Source	Identifier
Antibodies		
EF-Tu	Santa Cruz	sc-393924
Fam210a	Sigma Aldrich	HPA014324
HRP-conjugated secondary antibody, anti-mouse	BioRad	170-6516
HRP-conjugated secondary antibody, anti-rabbit	BioRad	170-6515
Opa1	BD Biosciences	612607
OXPHOS cocktail	Abcam	ab110413
Phospho-Stat1 (Tyr701) mouse monoclonal	Abcam	ab29045
Sdha	Abcam	ab14715
Vinculin	Cell Signaling	4650
Yme1l	Protein Tech	11510-1-AP
Chemicals and products		
2′,3′-dideoxycytidine (ddC)	Sigma Aldrich	D5782
5-fluorouracil (5-FU)	Sigma Aldrich	F6627
Biotin	Sigma Aldrich	B450
Biotin-phenol	Sigma Aldrich	SML2135
Cumate	System Biosciences	QM150A-1
Digitonin	Merck	300410
Dimethylsulfoxide (DMSO)	AppliChem	A3672
Genejuice transfection reagent	Merck	70967
GoScriptTM Reverse Transcription Mix	Promega	A2791
HEPES	Sigma Aldrich	H4034
Hydrogenperoxide	Roth	8070.4
Lipofectamine 2000 Transfection Reagent	Thermo Fisher Scientific	11668019
MitoSOX Red mitochondrial superoxide indicator	life technologies	M36008
Picogreen™, Quant-iT™ dsDNA	Thermo Fisher Scientific	P11495
Pierce™ NeutrAvidin™ beads	Pierce	29200

PKmito ORANGE	Genvivo/ tebubio-Sprirochrome	202205/ SC053
PowerSYBR Green PCR Master Mix	Thermo Fisher Scientific	4368708
Protease inhibitor cocktail tablet	Merck	11836170001
Sodium ascorbate	Sigma Aldrich	A4034
Sodium azide	Sigma Aldrich	S8032
Sodium deoxycholate	Sigma Aldrich	D6750
Sodium dodecyl sulfate	Sigma Aldrich	L4509
Tetracycline	Roth	0237.1
Tris	Roth	9140.3
Triton-X-100	Merck	1086031000
Trolox	Merck	648471
Urea	Serva	24524
YOYO-1 Iodide (491/509)	Invitrogen	Y3601
Kits		
DNeasy Blood & Tissue	Quiagen	69506
nCounter SPRINT reagent pack	Nanostring	NAA-AKIT-012 NAA-AKIT-048 NAA-AKIT-192
NucleoSpin RNA	Macherey-Nagel	740955.250
Q5 site-directed mutagenesis kit	New England Biolabs	E0554S
Seahorse XF Mito Stress Test Kits	Agilent	103016-100
Plasmids and vectors		
Alt-R™ CRISPR-Cas9 crRNA	Integrated DNA Technologies	513181565
Alt-R™ HDR Donor Oligo	Integrated DNA Technologies	513181564
Fam210a-pSpCas9 BB-2A-GFP PX458	GenScript	SC1678
Human OPA1 Variant 5 pLVX TRE3G	Fiona Mayer	N/A
SuperPiggyBac™ Transposase Expression Vector	System Biosciences	PB210PA-1-SBI
SuperPiggyBac™ Transposon Vector System	System Biosciences	PB210PA-1
Cell lines		
HEK293 WT MICU1-sOPA1-FLAG-APEX2	Tom McVicar	N/A
HEK293 WT MICU1-sOPA1^{K301A}-FLAG-APEX2	Tom McVicar	N/A
Immortalized Mus musculus embryonic fibroblasts (MEFs), *Cox10*$^{-/-}$	Ahola, Pazurek et al.	N/A
Immortalized Mus musculus embryonic fibroblasts (MEFs), *Cox10*$^{-/-}$*Opa1v1Δ4*	Ahola, Pazurek et al.	N/A
Immortalized Mus musculus embryonic fibroblasts (MEFs), *Fam210a*$^{-/-}$	This thesis	N/A
Immortalized Mus musculus embryonic fibroblasts (MEFs), *Opa1v1Δ4+v5*	This thesis	N/A
Immortalized Mus musculus embryonic fibroblasts (MEFs), WT, *Opa1v1, Opa1v1Δ4*	Ahola, Pazurek et al.	N/A

Oligonucleotides		
Cytb mouse qPCR forward primer GCTTTCCACTTCATCTTACCATTTA	This thesis	N/A
Cytb mouse qPCR reverse primer TGTTGGGTTGTTTGATCCTG	This thesis	N/A
Dloop1 mouse qPCR forward primer GTCCCTTGACCATCCTC	This thesis	N/A
Dloop1 mouse qPCR reverse primer GTAGCACTCTTGTGCGGGAT	This thesis	N/A
Fam210a mouse qPCR forward primer GGTTACCTGACAC	This thesis	N/A
Fam210a mouse qPCR reverse primer TTCCTCCCAAGGTCACGGTGTA	This thesis	N/A
Hprt mouse qPCR forward primer TCCTCCTCAGACCGCTTTT	This thesis	N/A
Hprt mouse qPCR reverse primer CATAACCTGGTTCATCATCGC	This thesis	N/A
Ifi44 mouse qPCR forward primer CTGATTACAAAAGAAGACATGACAGAC	This thesis	N/A
Ifi44 mouse qPCR reverse primer AGGCAAAACCAAAGACTCCA	This thesis	N/A
Ifit3 mouse qPCR forward primer TTCCCAGCAGCACAGAAAC	This thesis	N/A
Ifit3 mouse qPCR reverse primer AAATTCCAGGTGAAATGGCA	This thesis	N/A
Isg15 mouse qPCR forward primer CTAGAGCTAGAGCCTGCAG	This thesis	N/A
Isg15 mouse qPCR reverse primer AGTTAGTCACGGACACCAG	This thesis	N/A
Usp18 mouse qPCR forward primer GAGAGGACCATGAAGAGGA	This thesis	N/A
Usp18 mouse qPCR reverse primer TAAACCAACCAGACCATGAG	This thesis	N/A
Software and algorithms		
BioRender	BioRender	BioRender.com
IncuCyte® S3 Software	Sartorius	v2021C
Prism 9	Graph Pad	graphpad.com
ImageJ2 version 2.9.0/1.53t	Public domain	imagej.nih.gov/ij
InstantClue v0.12.0	Nolte, et al.[224]	instantclue.de
nSolver Analysis Software 4.0.70	Nanostring	nanostring.com

4.2.2 Methods from section 2.2

For the following methods see results section page 48-51:

Cell culture, transfection, SDS-PAGE and immunoblotting, quantitative Real-time PCR (qPCR), proteomics processing, STED and confocal imaging.

4.2.2.1 Animal Methods

Animal perfusion and tissue imaging

52-weeks-old mice were anesthetized intraperitoneally with a solution of ketamine (100 mg/kg body weight) and xylazine (20 mg/kg body weight). The injection volume corresponds to the recommended volume specified by GV-SOLAS of 10 ml/kg body weight. The mouse was slowly perfused with room-temperature saline until the fluid was clear with a switch to cold 4 % paraformaldehyde (PFA) for slow perfusion. Relevant organs were washed in 70 % ethanol for 8 h to remove excess formaldehyde. For dehydration, the organs were placed in an ascending alcohol series followed by incubation in xylene for 2 x 30 min to make the tissue permeable for paraffin. The tissue was transferred to casting molds with fresh, hot paraffin (60°C) and allowed to cool down. The blocks were cut into 4 µm thin sections using a rotary microtome and fixed on a glass slide for microscopy. Fixed tissues were imaged in a Leica Sp8-X confocal microscope equipped with a 40× oil/numerical aperture (NA) 1.45 objective with an excitation wavelength at 510 nm to image mitoYFP.

4.2.2.2 Cell culture-based methods and experimental procedures

CRISPR/Cas9 gene editing

To generate *Fam210a*$^{-/-}$ MEFs, cells were transfected with the eSpCas9 plasmid from GenScript (px458) containing the guide RNAs for a Cas9-dependent deletion (gRNA for *Fam210a* GATCACCATTGGCGCATAAA). MEFs were cultured under standard conditions in DMEM supplemented with 10 % fetal bovine serum (FBS), 1 % non-essential amino acids (NEAA) and 1 % sodium pyruvate. For transfection, 2x10^5 WT MEFs were seeded in 6-well plates one day prior to transfection to achieve approximately 70-80 % confluency. For transfection, 2.5 µg of the CRISPR-Cas9-eGFP plasmid DNA was mixed with 2,5 µL PLUS reagent in 150 µL Opti-MEM reduced serum medium and incubated for 5 min. Separately, 10 µL of Lipofectamine LTX was diluted in150 µL Opti-MEM and combined with the DNA/PLUS reagent mix, followed by 5 min incubation at RT. The mix was added dropwise to the well and incubated at 37°C with 5 % CO_2. After 3 days of incubation, single GFP-positive cells were isolated by FACS sorting and collected on 96-well to enrich for transfected cell populations. Monoclonal cells were screened for successful *Fam210a*$^{-/-}$ by western blot.

Generation of stable cell lines

Stable *Opa1v1Δ4+v5* cell lines with inducible expression of *Opa1v5* were generated in MEFs using the PiggyBac transposon system. The complementary cDNA encoding for human Opa1v5 was cloned into a PiggyBac transposon vector via the Q5 site-directed mutagenesis kit (NEB). $2x10^5$ MEFs were cultured in 6-well under standard conditions one day before transfection to reach 70-80 % confluency. 1 µg PiggyBac transposon vector containing the gene of interest and 0.4 µg/µL of SuperPiggyBac Transposase Expression Vector were applied onto the cells via Genejuice transfection reagent (72µL Opti-MEM +4,5 µL GeneJuice, 15 min incubation). After 24 h, cells were harvested and plated on 10 cm dishes. Cells were subjected to puromycin selection (4 µg/mL) up to 5 days to enrich for stably integrated clones. Selected bulk populations were expanded and diluted for single-cell selection. Protein expression was induced by the addition of cumate (15-60 µg/mL). Expression levels were monitored via western blot to confirm cumate-dependent induction and background expression in the absence of inducer.

5-FU treatment

MEFs were seeded $0.6x10^5$ per well in 6-well plates one day prior to 5-FU treatment. Afterwards, cells were treated with 5 µM 5-FU (in DMSO) diluted in complete culture medium. Cells were incubated with the drug for 16 h under standard culture conditions. In the last step, cells were scaped in the medium, washed with PBS and the pellet was used for RNA isolation.

mtDNA repopulation assay

Cells were seeded $0.1x10^5$ in 6-well plates and treaded with 40 µM ddC. After 72 h, untreaded and day 3 treaded sample were collected and medium was exchanged for the remaining wells with normal culturing medium. Samples were collected after 4, 5, 6 and 7 days. Afterwards, mtDNA content was analyzed via DNA isolation and qPCR.

Picogreen staining and imaging

Cells were seeded $1.5x10^5$ on live-cell imaging glass bottom dishes (ibidi, µ-dish, 35-mm high). Next day, 1:1000 Picogreen in complete medium was added to the cells and incubated for 20 min. Afterwards, cells were washed 3x with PBS and incubated for 2 h to remove unbound stain. In a next step, cells were recorded using a Facility Line microscope (Abberior Instruments) equipped with an Olympus UPLXAPO 60× oil/NA

1.4 objective at 37°C and an excitation wavelength at 488-nm with 30 % laser power and 3x line accumulations.

4.2.2.3 Molecular and biochemical methods

Measurement of oxygen consumption rate

For OCR measurement, cells were seeded $2x10^5$ in Agilent provided 96-well plate one day before performing the "Seahorse XF Cell Mito Stress Test". Sensor cartridge hydration and drug preparation was performed according to the manufacturer's instructions (oligomycin - 2µM, FCCP - 0.5 µM, rotenone and antimycin A - 0.5 µM). 1 h before the stress test, cell growth media was exchanged to assay media containing Seahorse assay media (103575-100) supplemented with 10 mM glucose, 2mM l-glutamine, 1 mM sodium-pyruvate and 1 mM NEAA. Mitochondrial respiration was measured in a Seahorse Extracellular Flux Analyzer XFe96.

IncuCyte-based quantitative cell death assay

For IncuCyte, $2x10^5$ cells per well were seeded in a 96-well plate containing 1:500 YOYO and 500 µM H_2O_2 in normal culturing medium. Proliferation and cell death were monitored using phase-contrast microscopy at 10× magnification on the IncuCyte Live-Cell Analysis System allowing real-time, non-invasive imaging within the incubator. To evaluate cell death, the dead cells vs. confluence were plotted over time. Statistical significance was analyzed using one-way ANOVA. Data visualization and statistical analyses were conducted using GraphPad Prism software.

ISG mRNA quantifications with Nanostring nCounter

Cells were treated with 5-FU as described above. After total RNA isolation using the NucleoSpin RNA isolation kit, RNA quantity and purity were assessed via NanoDrop spectrophotometer. For NanoString analysis, 500 ng of total RNA in 5 µL was subjected to CodeSet hybridization (70 µL hybridization buffer and reporter code set, 8 µL per sample) and incubated with 2µL capture probe set at 65°C for 16 h. After hybridization, samples were diluted with 20 µL nuclease-free water, and 33 µL of each sample was applied onto a NanoString cartridge. The run was performed following the manufacturer's guidelines with the selected library for chosen ISG markers. Data quality control and normalization were performed using nSolver analysis software.

Statistical analyses were conducted using one-way ANOVA. Reference genes ActB, B2m, Gapdh, Sdha, and Hprt were used for normalization purposes to ensure accurate expression quantification.

MitoSOX staining and flow cytometry analysis

Cells were harvested by trypsinization, washed and resuspended in 1 mL PBS and incubated with 5 µM MitoSOX Red (Thermo Fisher Scientific) at 37°C for 20 min in the dark. After incubation, cells were washed 2x with warm PBS to remove excess dye. Afterwards, cell pellets were resuspended in 0.5 µL PBS with 1 µL DAPI and transferred into flow cytometry tubes. Flow cytometry was performed immediately on BD FACSCanto II instrument, measuring the fluorescence emission at 580 nm (DAPI in PE channel). Data were analyzed using FlowJo software to quantify mitochondrial superoxide levels as mean fluorescence intensity. Data visualization and statistical analyses were conducted using GraphPad Prism software.

Proximity-proteomics assay

For APEX2 proximity labeling, $4x10^5$ stable HEK293 WT MICU1(MTS aa 1-60)-sOPA1 (aa 194-997)-FLAG-APEX2 and HEK293 WT MICU1(MTS aa1-60)-sOPA1^{K301A}FLAG-APEX2 cells were seeded on 15 cm dishes and protein expression was allowed for 24 h with 0.5 µg/mL tetracycline. For biotin labeling, cells were incubated with 500 µM biotin-phenol for 30 min at 37°C. Afterwards, 25 µL of 1 M H_2O_2 in 500 µL media was added per well for 1 min at RT. To terminate labelling, media was aspirated and cells were wash 4x with 10 mL quencher solution (10 mM sodium ascorbate, 10 mM sodium azide, 5 mM Trolox in PBS). Cells were scaped in 5 mL quencher solution and pellet was resuspended in 350 µL RIPA lysis buffer and incubated for 15 min on ice. Supernatants were collected and biotin labeling was monitored via western blot with streptavidin-HRP. Neutravidin beads were washed twice with 500 µL RIPA buffer and incubated with the lysates (orbital rotor, 1 h at RT). Beads were washed 2x with RIPA, 1x with 1 mL 2 M Urea/Tris-HCl pH 8.0 and again 2x with RIPA. In the final step, 40 µL 2x LDS-sample buffer (NuPAGE-with 20 mM DTT) supplemented with 2 mM biotin was added to the beads and boiled at 95°C for 5 min. Afterwards, samples were submitted for mass spectrometry analysis. For protein digestion, 20 µg protein lysate and eluates of proximity labeling were subjected to tryptic digestion. Proteins were reduced (10 mM TCEP) and alkylated (20 mM CAA) in the dark for 45 min at 45°C. Samples were

subjected to an SP3-based digestion 1. Washed SP3 beads (SP3 beads (Sera-Mag(TM) Magnetic Carboxylate Modified Particles (Hydrophobic, GE44152105050250), Sera-Mag(TM) Magnetic Carboxylate Modified Particles (Hydrophilic, GE24152105050250) from Sigma Aldrich) were mixed equally, and 3 µL of bead slurry were added to each sample. Acetonitrile was added to a final concentration of 50 % and washed twice using 70 % ethanol (V=200 µL) on an in-house manufactured magnet. After an additional acetonitrile wash (V=200µL), 5 µL digestion solution (10 mM HEPES pH = 8.5 containing 0.5µg Trypsin (Sigma) and 0.5µg LysC (Wako)) was added to each sample and incubated overnight at 37°C. Peptides were desalted on a magnet using 2 x 200 µL acetonitrile. Peptides were eluted in 10 µL 5 % DMSO in LC-MS water (Sigma Aldrich) in an ultrasonic bath for 10 min. Formic acid and acetonitrile were added to a final concentration of 2.5 % and 2 %, respectively. Samples were stored at -20°C before subjection to LC-MS/MS analysis.

LC-MS/MS (proximity labeling)

LC-MS/MS instrumentation consisted of an Easy-LC 1200 (Thermo Fisher Scientific) coupled via a nano-electrospray ionization source to an Exploris 480 mass spectrometer (Thermo Fisher Scientific, Bremen, Germany). An Aurora Frontier column (60cm length, 1.7 µm particle diameter, 75 µm inner diameter, Ionopticks). A binary buffer system (A: 0.1 % formic acid and B: 0.1 % formic acid in 80 % acetonitrile) based gradient was utilized as follows at a flow rate of 185 nL/min; a linear increase of buffer B from 4 % to 28 % within 70 min, followed by a linear increase to 40 % within 10 min. The buffer B content was further ramped to 50 % within 4 minutes and then to 65 % within 3 minutes. 95 % buffer B was kept for a further 3 min to wash the column (total gradient time: 90 min). The RF Lens amplitude was set to 45 %, the capillary temperature was 275°C and the polarity was set to positive. MS1 profile spectra were acquired using a resolution of 30,000 (at 200 m/z) at a mass range of 500/800 m/z and an AGC target of 1 × 106. For MS/MS independent spectra acquisition, 34 equally spaced windows were acquired at an isolation m/z range of 8 Th, and the isolation windows overlapped by 1 Th. The fixed first mass was 200 m/z. The isolation center range covered a mass range of 500–740 m/z. Fragmentation spectra were acquired at a resolution of 30,000 at 200 m/z using a maximal injection time setting of ‘auto’ and stepped normalized collision energies (NCE) of 24, 28, and 30. The default charge

state was set to 3. The AGC target was set to 3e6 (900 % - Exploris 480). MS2 spectra were acquired in centroid mode. FAIMS was enabled using an inner electrode temperature of 100°C and an outer electrode temperature of 90°C. The compensation voltage was set to -45V.

Data Analysis (proximity labeling)

DIA data were processed using Spectronaut 19 (version 19.1.240806.62635) using default settings. Database searching was performed with the Pulsar engine against the Homo sapiens UniProt reference proteome (UP000005640_9606) using Trypsin/P specificity, allowing up to two missed cleavages, a minimum peptide length of 7 amino acids, and a maximum length of 52. Carbamidomethylation of cysteine was specified as a fixed modification, and variable modifications included N-terminal protein acetylation and methionine oxidation; N-terminal methionine excision was allowed. For peptide-spectrum identification, Spectronaut applied 1 % FDR filtering at the precursor and protein levels. Decoys were generated dynamically using mutated sequences with neural network–predicted fragments, and p-values were estimated via kernel density estimation. IDPicker was used for protein inference. MS1 and MS2 mass tolerances, as well as extraction windows for retention time and ion mobility, were determined dynamically. Fragment ions were filtered to b/y types between m/z 200–3000 with a minimum fragment length of three amino acids.Quantification was performed at the MS2 fragment-ion level using area-based intensities. Only Q-value–filtered precursors were used, without imputation. Cross-run normalization was enabled and performed automatically. Protein quantification followed a Top-3 mean peptide strategy and the MaxLFQ intensity normalization.

4.2.2.4 AI tools

DeepL Translator/Write and perplexity AI were used supporting the writing process of this thesis**.** Schematic illustrations were generated using BioRender.

5 Appendix

Science Advances
AAAS

Supplementary Materials for

Opa1 processing is dispensable in mouse development but is protective in mitochondrial cardiomyopathy

Sofia Ahola *et al.*

Corresponding author: Thomas Langer, tlanger@age.mpg.de

Sci. Adv. **10**, eadp0443 (2024)
DOI: 10.1126/sciadv.adp0443

The PDF file includes:

Figs. S1 to S4
Table S1
Legend for table S2

Other Supplementary Material for this manuscript includes the following:

Table S2

Supplementary Figure 1

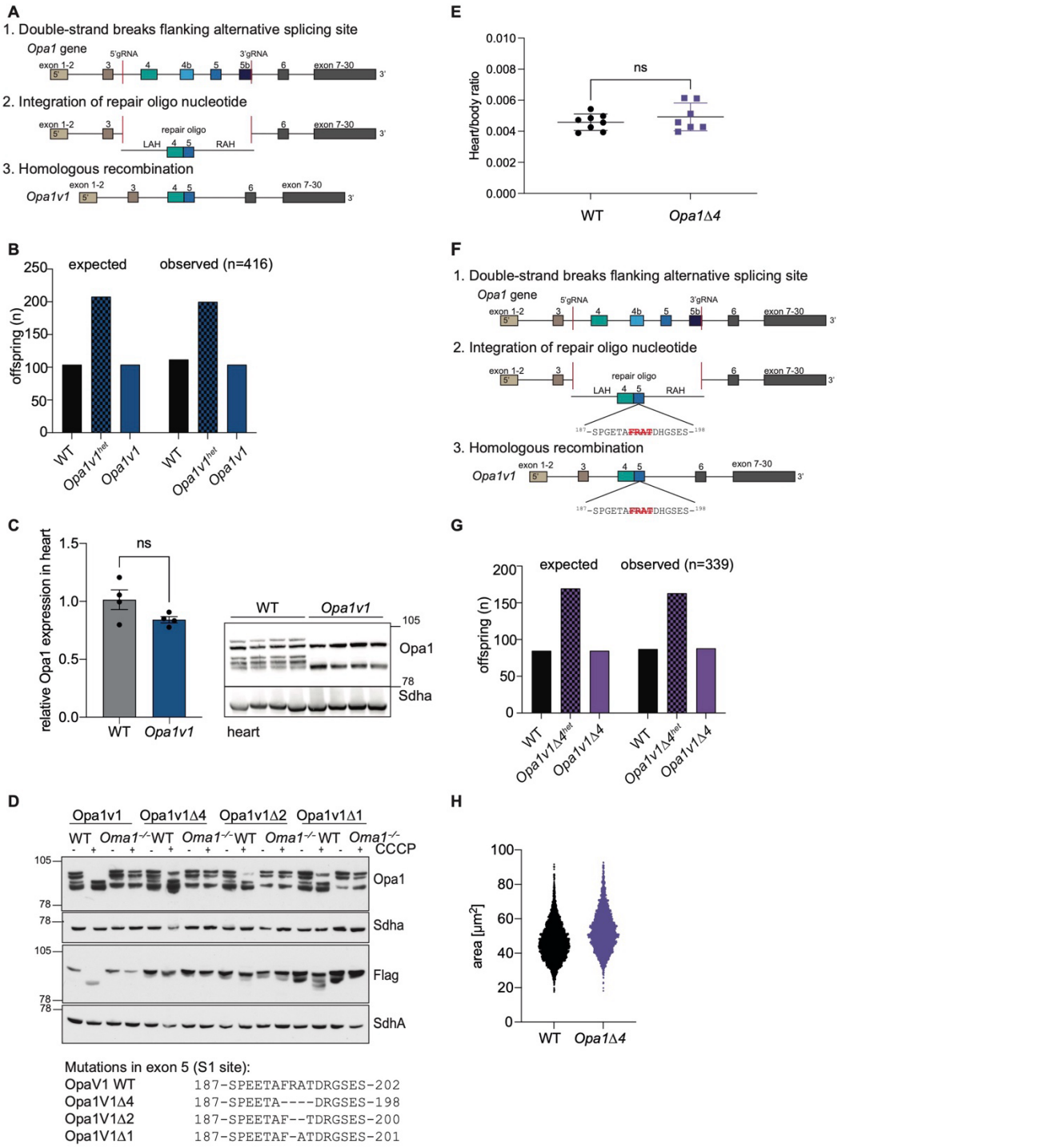

Supplementary Figure 1. Generation of transgenic *Opa1v1* and *Opa1v1Δ4* mice. **(A)** Gene editing strategy for transgenic Opa1v1 mice using CRISPR/Cas9 system. 1. gRNAs flanking the alternative splicing site induced a double-strand break upstream of exon 4 and downstream of exon 5b. The two gRNA templates excise a 10kb region in the Opa1 locus. 2. A defined repair oligonucleotide is annealed to the alternative splicing site by homology arms. 3. The repair oligonucleotide is integrated into the endogenous site by homologous recombination. **(B)** Expected and observed birth ratios of Opa1v1 mice from heterozygous crosses (n=416 pups). **(C)** Quantification of Opa1 levels in the heart of 12-weeks old WT (n=4) and *Opa1v1Δ4* (n=4) mice, unpaired t-test. **(D)** WT and Oma1$^{-/-}$ MEFs transiently expressing Flag-tagged Opa1 variants and treated with CCCP (20 µM) for 2 h. Amino acid sequences at S1 of different Opa1 mutants. **(E)** Heart/body weight ratio from 64-weeks old WT (n=7) and *Opa1v1Δ4* (n=7) mice, unpaired t-test. **(F)** Gene editing strategy for *Opa1v1Δ4* mice showing the deleted four amino acids in the repair oligo in red. **(G)** Expected and observed birth ratios of *Opa1v1* mice from heterozygous crosses (n=339 pups). **(H)** Analysis of the cell size via flow cytometry (Cytek® Corporation). The size of up to 2000 cells in n=3 biological replicates of WT and *Opa1v1Δ4* MEFs was analyzed (in µm2).

Supplementary Figure 2

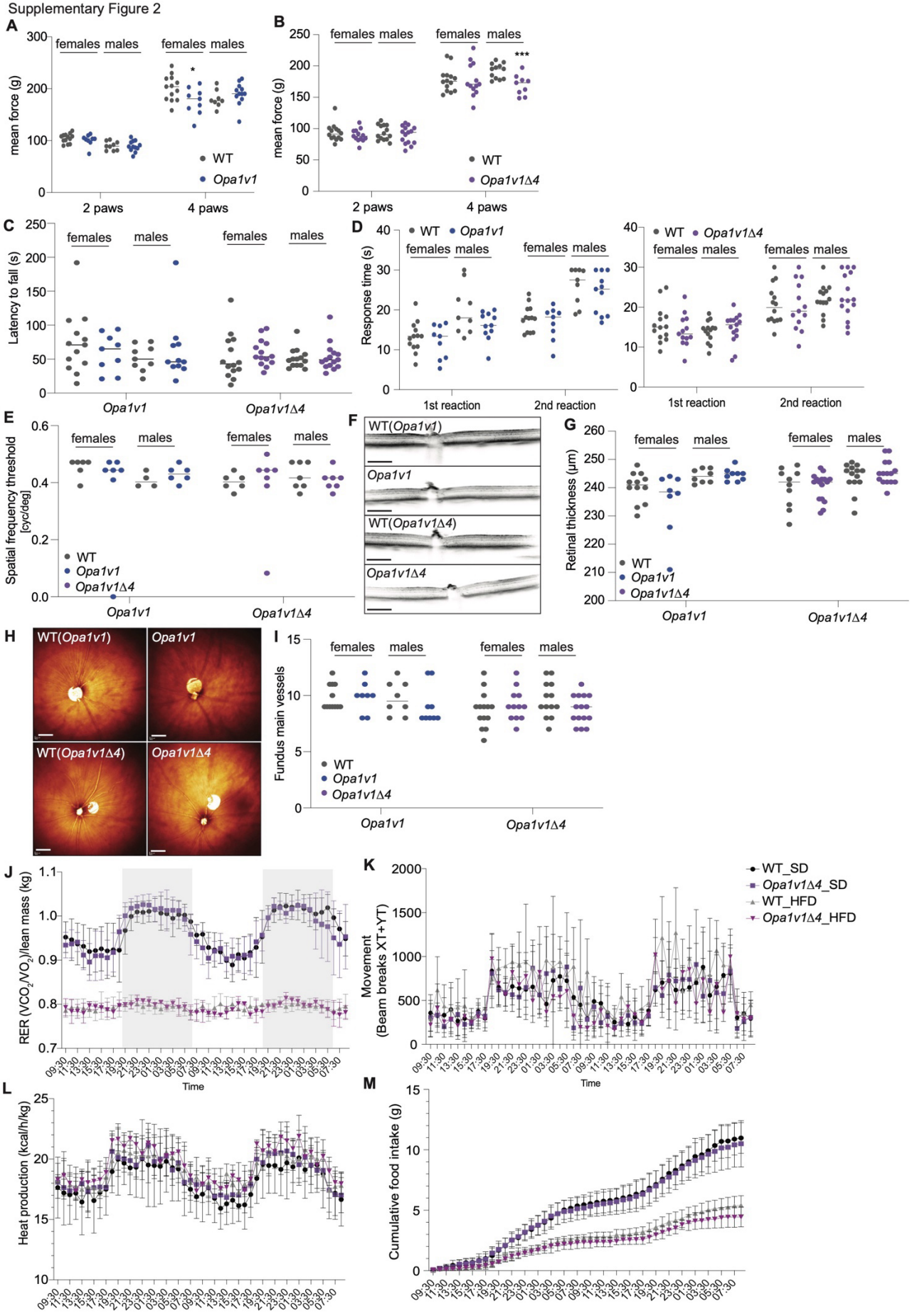

Supplementary Figure 2. Phenotypic analysis of 68-77-weeks-old *Opa1v1* and *Opa1v1Δ4* mice and corresponding WT littermates. (**A**) Grip strength test for *Opa1v1* mice with two and four paws (WT f=13, m=8-9, *Opa1v1* f= 9, m=12). (**B**) Grip strength test for *Opa1v1Δ4* mice with two and four paws (wt f =14, m = 12-14, *Opa1v1Δ4* f=13-14, m= 9-15). **(C)** Accelerating rotarod test for *Opa1v1* and *Opa1v1Δ4* mice (WT f= 13, m= 9, *Opa1v1* f=9, m=11, and WT f=14, m=14, *Opa1v1Δ4* f=14, m=15). **(D)** Hotplate test for *Opa1v1* and *Opa1v1Δ4* mice and corresponding WT littermates showing the time of first and second reaction (WT f=13, m=9, *Opa1v1* f=9, m=11 and WT f=14, m=14, *Opa1v1Δ4* f=13, m=15). (**E**) Virtual drum measurements (WT f=6, m=4, *Opa1v1* f=7, m=6 and WT f=6, m=7, *Opa1v1Δ4* f=7, m=7). (**F**) Representative images of left retinal layers. Scale bar, 1 mm. (**G**) Left retinal thickness (WT f=12, m=8, *Opa1v1* f=8, m=8 and WT f=10, m=14, *Opa1v1Δ4* f=16, m=15). (**H**) Representative images of left fundus. **(I)** Number of blood veins in the left retinal fundus (WT f=12, m=8, *Opa1v1* f=8, m=9 and WT f=14, m=13, *Opa1v1Δ4* f=12, m=15). Scale bar, 1 mm. (**J-M**) Phenomaster data for respiratory exchange ratio (RER), movement, estimated heat production and cumulative food intake of control diet and HFD fed WT and *Opa1v1Δ4* male mice after 10 weeks of diets (WT control diet=7, HFD=4, *Opa1v1Δ4* control diet=6, HFD=3).

Supplementary Figure 3

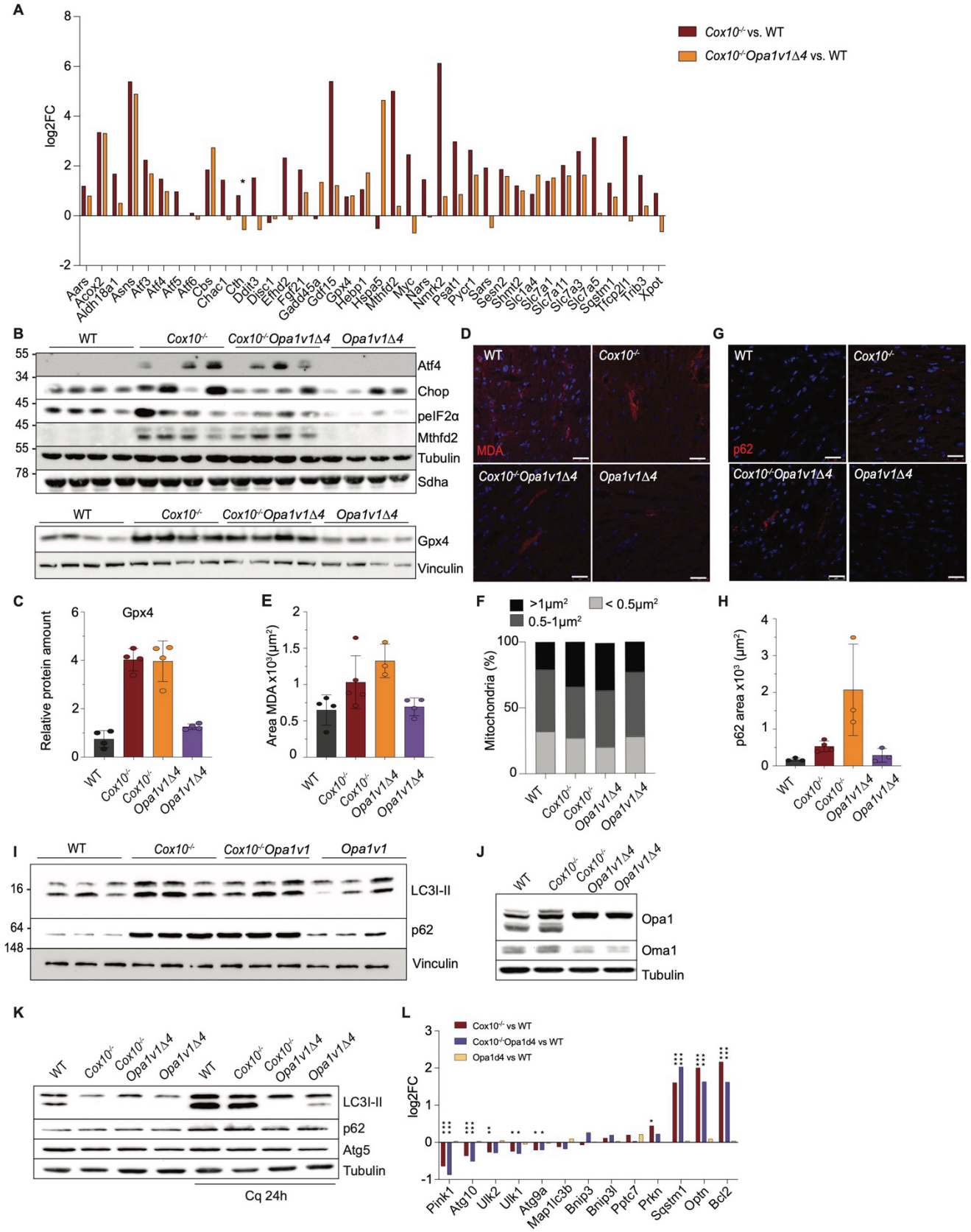

Supplementary Figure 3. Analysis of 2-weeks-old WT, *Cox10*$^{-/-}$, *Cox10*$^{-/-}$*Opa1v1Δ4* and *Opa1v1Δ4* mice and corresponding WT littermates. (**A**) mRNA levels of ISR target genes in hearts of WT, *Cox10*$^{-/-}$ and *Cox10*$^{-/-}$*Opa1v1Δ4* mice, which were determined by Nanostring analysis and which are shown as log 2-fold change between WT and *Cox10*$^{-/-}$ and WT and *Cox10*$^{-/-}$*Opa1v1Δ4.* (**B**) Immunoblot analysis of heart lysates using antibodies against the ISR target protein Mthfd2, peIF2a, the transcription factors Atf4 and Chop, and, in the lower panel, Gpx4. The steady state levels of Sdha and vinculin were monitored for control. (**C**) Quantification of Gpx4 levels in (B). (**D, E**) Representative images for malondialdehyde (MDA) immunohistochemistry staining from the mouse heart with quantification shown in (E) (n=3-4). Scale bars, 25 µm. (**F**) Quantification of mitochondrial sizes in TEM analysis (n=3, >200 mitochondria were analyzed/mouse, data shown as average). (**G, H**) Representative images for p62 immunohistochemistry staining from the mouse heart with quantification shown in (H) (n=3-4). (**I**) Immunoblot analysis of LCI-II and p62 of 2-week-old animals in WT (n=3) , *Cox10*$^{-/-}$ (n=3), *Cox10*$^{-/-}$*Opa1v1* (n=3) and *Opa1v1* (n=3). Lipidated LC3II form and p62 accumulate in *Cox10*$^{-/-}$ and *Cox10*$^{-/-}$*Opa1v1* hearts. (**J**) Immunoblot analysis of Opa1 in MEFs. Scale bars, 25 µm. (**K**) Immunoblot analysis of LC3I-II, p62 and Atg5 in MEFs treated for 24 h with chloroquinone (Cq, 10 µM). (**L**) RNAseq data of autophagy markers in *Cox10*$^{-/-}$ vs WT (red), *Cox10*$^{-/-}$*Opa1v1Δ4* vs WT (purple) and *Opa1v1Δ4* vs WT (yellow), *p< 0.05, **p< 0.01, ***p< 0.001.

Supplementary Figure 4

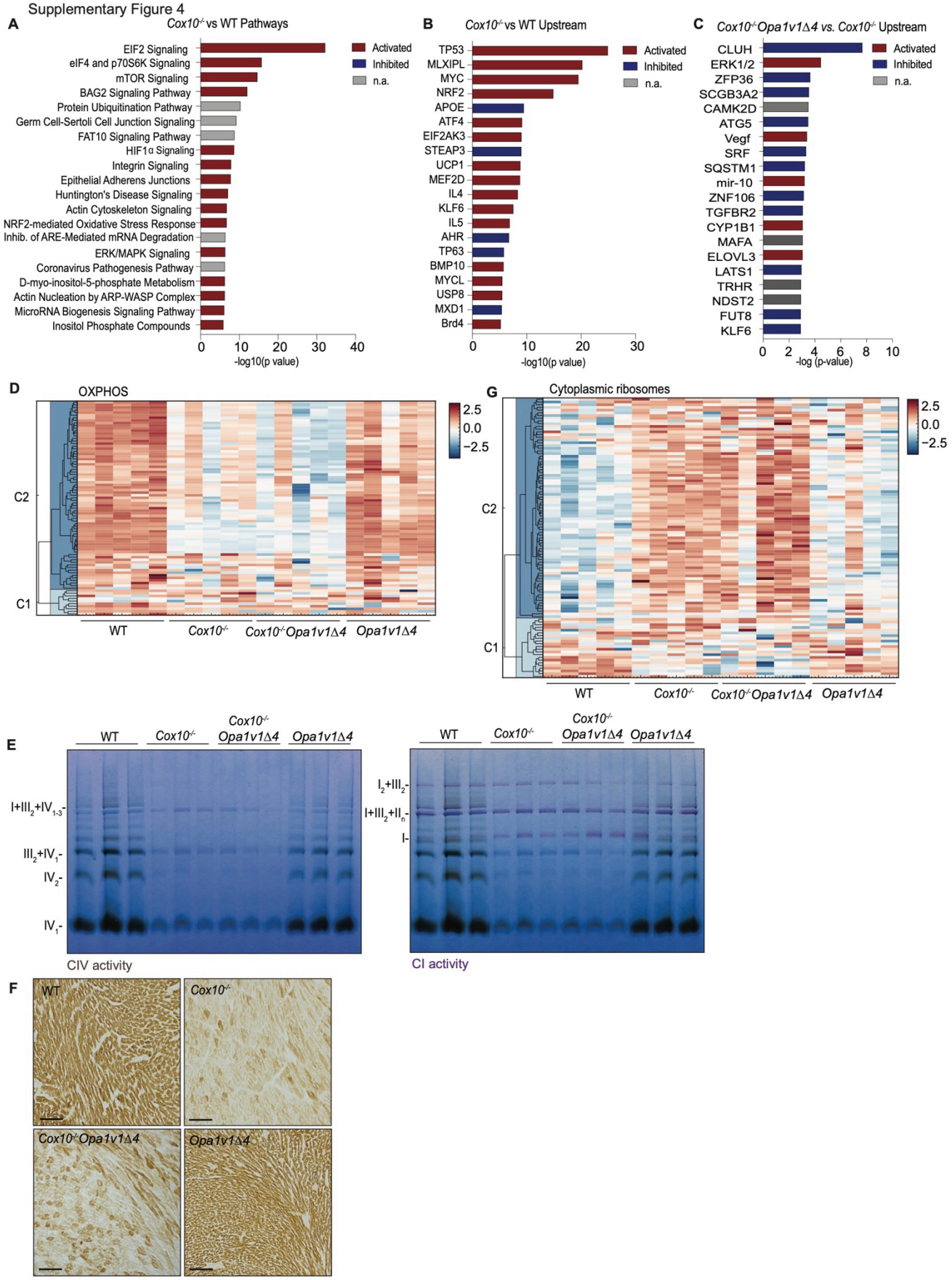

Supplementary Figure 4. Analysis of gene expression and mitochondrial functions of 2-weeks-old WT, *Cox10*$^{-/-}$, *Cox10*$^{-/-}$*Opa1v1Δ4* and *Opa1v1Δ4* mouse hearts. (**A**) Ingenuity pathway analysis of RNAseq datasets for WT and *Cox10*$^{-/-}$ hearts. (**B**) Ingenuity analysis of RNAseq datasets (as in A) to identify predicted upstream regulatory factors whose target gene expression is most significantly altered between WT and *Cox10*$^{-/-}$ hearts. (**C**) Most significantly changed upstream regulatory factors between *Cox10*$^{-/-}$ and *Cox10*$^{-/-}$*Opa1v1Δ4* identified the altered expression of target genes by the Ingenuity analysis. (**D**) Heatmap of Z-scores of OXPHOS-annotated proteins from the heart proteome dataset. (**E**) Blue native gel electrophoresis of mitochondria isolated from the hearts of 2-week-old mice stained for complex IV (CIV) and complex I (CI) activity. (**F**) Representative images for CIV activity staining of mouse hearts of the indicated genotypes. Scale bar, 0.1 mm. (**G**) Heatmap of Z-scores of cytoplasmic ribosome-annotated proteins from the heart proteome dataset.

Supplementary information

Supplementary Table 1: Primers and oligos

Oligo	Sequence
5' gRNA *mOpa1* intron 3/4	AAAACTACAGCACACGGCAA
3' gRNA *mOpa1* exon 5b	CTATGCCCAACAGAAGCGCA
5' gRNA h*OPA1* exon 1	GCGGGATGTGGCGACTACGTCGG
3' gRNA h*OPA1* exon 11	CCTATTTAAAGATAGTTCTC
3' gRNA *mCox10*	GTCGAGGGAATGGTCCACTA
mCox10 sequencing primer forward	GTAATGTGTGCTATTTGTCTGTCTG
mCox10 sequencing primer reverse	ATGTGAGACAATCCACAATCATGT

Oligo	Sequence (5'->3')
Opa1v1 ssODN	TAGAAAAGCCCTGCCCAGCTCAGAAGACCTTGCCAGTTTAG CTCCCGACCTGGACAAGATTACTGAGAGCCTCAGCTTGTTG AAGGACTTCTTCACTGCAGGTTCACCTGGAGAAACAGCATT TCGAGCAACAGATCATGGATCTGAAAGTGACAAGCATTACC GCAAG
Opa1v1Δ4 ssODN	TAGAAAAGCCCTGCCCAGCTCAGAAGACCTTGCCAGTTTAG CTCCCGACCTGGACAAGATTACTGAGAGCCTCAGCTTGTTG AAGGACTTCTTCACTGCAGGTTCACCTGGAGAAACAGCAGA TCATGGATCTGAAAGTGACAAGCATTACCGCAAG

Supplementary Table Legends

Supplementary Table 1. Primers and oligoes used to modify the Opa1 locus by CRISPR-mediated genome editing.

Supplementary Table 2. Protein group DIA-NN quantitative matrix including the log2 LFQ intensity accompanied with protein annotations and statistical analysis (pairwise comparison, one-way ANOVA, and K-Means clustering).

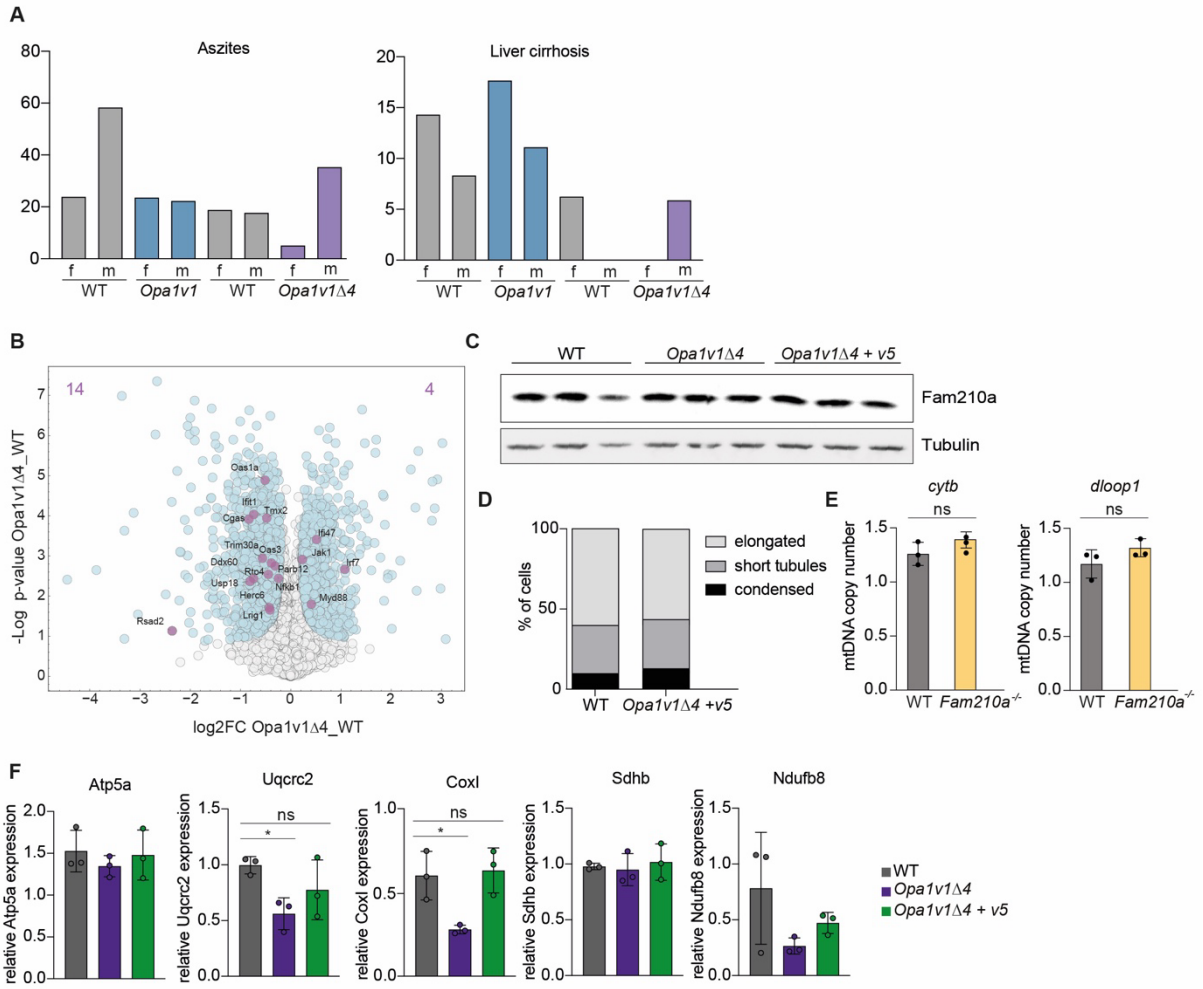

Supplementary Figure 5: (A): Bar diagrams of observed age and disease-associated abnormalities in old mice in WT^{Opa1v1} (female (f) n=21, male (m)=12, grey), *Opa1v1* (female (f) n=17, male (m)=18, light blue), WT$^{Opa1v1\Delta4}$ (female (f) n=16, male (m)=17, grey) and *Opa1v1Δ4* (female (f) n=20, male (m)=17, light violet). **(B):** Volcano plot of the mass spectrometry data of *Opa1v1Δ4* vs. WT with indicated significant changed proteins in blue. Known ISG upregulated proteins are marked in purple. **(C):** Western blot analysis of Fam210a levels in WT and *Fam210a*$^{-/-}$ **(D):** Bar-diagram representation of morphology of WT and *Opa1v1Δ4+v5* MEFs in the subgroups elongated, short tubules and condensed (n=10). **(E):** Bar-diagram of relative mtDNA copy numbers in WT (grey) and *Fam210a*$^{-/-}$(yellow) MEFs (n=3). **(F):** Levels of OXPHOS subunits in WT, *Opa1v1Δ4* and *Opa1v1Δ4+v5* normalized to Vinculin. Statistical significance was analyzed using one-way ANOVA**.**

6 References

1. Palade, G.E. (1953). An electron microscope study of the mitochondrial structure. J Histochem Cytochem *1*, 188–211. 10.1177/1.4.188.
2. Sagan, L. (1967). On the origin of mitosing cells. J Theor Biol *14*, 255–274. 10.1016/0022-5193(67)90079-3.
3. Veltri, K.L., Espiritu, M., and Singh, G. (1990). Distinct genomic copy number in mitochondria of different mammalian organs. J Cell Physiol *143*, 160–164. 10.1002/jcp.1041430122.
4. Pesta, D. (2024). Mitochondrial density in skeletal and cardiac muscle. Mitochondrion *75*, 101838. https://doi.org/10.1016/j.mito.2023.101838.
5. Hinton, A., Jr., Claypool, S.M., Neikirk, K., Senoo, N., Wanjalla, C.N., Kirabo, A., and Williams, C.R. (2024). Mitochondrial Structure and Function in Human Heart Failure. Circ Res *135*, 372–396. 10.1161/circresaha.124.323800.
6. Mitchell, P. (1966). Chemiosmotic coupling in oxidative and photosynthetic phosphorylation. Biol Rev Camb Philos Soc *41*, 445–502. 10.1111/j.1469-185x.1966.tb01501.x.
7. Lehninger, A.L., Wadkins, C.L., Cooper, C., Devlin, T.M., and Gamble, J.L. (1958). Oxidative Phosphorylation. Science *128*, 450–456. DOI 10.1126/science.128.3322.450.
8. Kushnareva, Y., Gerencser, A., Bossy, B., Ju, W., White, A., Waggoner, J., Ellisman, M., Perkins, G., and Bossy-Wetzel, E. (2013). Loss of OPA1 disturbs cellular calcium homeostasis and sensitizes for excitotoxicity. Cell Death & Differentiation *20*, 353–365.
9. Olichon, A., Baricault, L., Gas, N., Guillou, E., Valette, A., Belenguer, P., and Lenaers, G. (2003). Loss of OPA1 perturbates the mitochondrial inner membrane structure and integrity, leading to cytochrome c release and apoptosis. Journal of Biological Chemistry *278*, 7743–7746.
10. Gómez-Valadés, A.G., Pozo, M., Varela, L., Boudjadja, M.B., Ramírez, S., Chivite, I., Eyre, E., Haddad-Tóvolli, R., Obri, A., and Milà-Guasch, M. (2021). Mitochondrial cristae-remodeling protein OPA1 in POMC neurons couples Ca2+ homeostasis with adipose tissue lipolysis. Cell metabolism *33*, 1820–1835. e1829.
11. Kunau, W.H., Dommes, V., and Schulz, H. (1995). beta-oxidation of fatty acids in mitochondria, peroxisomes, and bacteria: a century of continued progress. Prog Lipid Res *34*, 267–342. 10.1016/0163-7827(95)00011-9.
12. Klopstock, T., Priglinger, C., Yilmaz, A., Kornblum, C., Distelmaier, F., and Prokisch, H. (2021). Mitochondrial Disorders. Dtsch Arztebl Int *118*, 741–748. 10.3238/arztebl.m2021.0251.
13. Schlieben, L.D., and Prokisch, H. (2020). The Dimensions of Primary Mitochondrial Disorders. Front Cell Dev Biol *8*, 600079. 10.3389/fcell.2020.600079.
14. Giles, R.E., Blanc, H., Cann, H.M., and Wallace, D.C. (1980). Maternal inheritance of human mitochondrial DNA. Proceedings of the National Academy of Sciences *77*, 6715–6719. doi:10.1073/pnas.77.11.6715.
15. Müller-Höcker, J. (1992). Mitochondria and Ageing. Brain Pathology *2*, 149–158. https://doi.org/10.1111/j.1750-3639.1992.tb00683.x.
16. Yin, F., Sancheti, H., Liu, Z., and Cadenas, E. (2016). Mitochondrial function in ageing: coordination with signalling and transcriptional pathways. J Physiol *594*, 2025–2042. 10.1113/jp270541.
17. Nass , M.M.K., and Nass , S. (1963). INTRAMITOCHONDRIAL FIBERS WITH DNA CHARACTERISTICS : I. Fixation and Electron Staining Reactions. Journal of Cell Biology *19*, 593–611. 10.1083/jcb.19.3.593.

18. Schatz, G., Haslbrunner, E., and Tuppy, H. (1964). Deoxyribonucleic acid associated with yeast mitochondria. Biochemical and Biophysical Research Communications *15*, 127–132. https://doi.org/10.1016/0006-291X(64)90311-0.
19. Anderson, S., Bankier, A.T., Barrell, B.G., de Bruijn, M.H., Coulson, A.R., Drouin, J., Eperon, I.C., Nierlich, D.P., Roe, B.A., Sanger, F., et al. (1981). Sequence and organization of the human mitochondrial genome. Nature *290*, 457–465. 10.1038/290457a0.
20. KANKI, T., NAKAYAMA, H., SASAKI, N., TAKIO, K., ALAM, T.I., HAMASAKI, N., and KANG, D. (2004). Mitochondrial Nucleoid and Transcription Factor A. Annals of the New York Academy of Sciences *1011*, 61–68. https://doi.org/10.1196/annals.1293.007.
21. Milenkovic, D., Matic, S., Kuhl, I., Ruzzenente, B., Freyer, C., Jemt, E., Park, C.B., Falkenberg, M., and Larsson, N.G. (2013). TWINKLE is an essential mitochondrial helicase required for synthesis of nascent D-loop strands and complete mtDNA replication. Hum Mol Genet *22*, 1983–1993. 10.1093/hmg/ddt051.
22. Hoppins, S., Lackner, L., and Nunnari, J. (2007). The machines that divide and fuse mitochondria. Annu Rev Biochem *76*, 751–780. 10.1146/annurev.biochem.76.071905.090048.
23. D'Souza, A.R., and Minczuk, M. (2018). Mitochondrial transcription and translation: overview. Essays Biochem *62*, 309–320. 10.1042/ebc20170102.
24. Rossignol, R., Faustin, B., Rocher, C., Malgat, M., Mazat, J.P., and Letellier, T. (2003). Mitochondrial threshold effects. Biochem J *370*, 751–762. 10.1042/bj20021594.
25. Cree, L.M., Samuels, D.C., de Sousa Lopes, S.C., Rajasimha, H.K., Wonnapinij, P., Mann, J.R., Dahl, H.H., and Chinnery, P.F. (2008). A reduction of mitochondrial DNA molecules during embryogenesis explains the rapid segregation of genotypes. Nat Genet *40*, 249–254. 10.1038/ng.2007.63.
26. Green, D.E., and Tzagoloff, A. (1966). The mitochondrial electron transfer chain. Archives of Biochemistry and Biophysics *116*, 293–304. https://doi.org/10.1016/0003-9861(66)90036-1.
27. Slater, E.C. (1953). Mechanism of phosphorylation in the respiratory chain. Nature *172*, 975–978. 10.1038/172975a0.
28. Signes, A., and Fernandez-Vizarra, E. (2018). Assembly of mammalian oxidative phosphorylation complexes I-V and supercomplexes. Essays Biochem *62*, 255–270. 10.1042/ebc20170098.
29. Zhou, A., Rohou, A., Schep, D.G., Bason, J.V., Montgomery, M.G., Walker, J.E., Grigorieff, N., and Rubinstein, J.L. (2015). Structure and conformational states of the bovine mitochondrial ATP synthase by cryo-EM. eLife *4*, e10180. 10.7554/eLife.10180.
30. Heinz, S., Freyberger, A., Lawrenz, B., Schladt, L., Schmuck, G., and Ellinger-Ziegelbauer, H. (2017). Mechanistic Investigations of the Mitochondrial Complex I Inhibitor Rotenone in the Context of Pharmacological and Safety Evaluation. Scientific Reports *7*, 45465. 10.1038/srep45465.
31. Aldakkak, M., Stowe, D.F., Chen, Q., Lesnefsky, E.J., and Camara, A.K.S. (2008). Inhibited mitochondrial respiration by amobarbital during cardiac ischaemia improves redox state and reduces matrix Ca2+ overload and ROS release†. Cardiovascular Research *77*, 406–415. 10.1016/j.cardiores.2007.08.008.
32. You, B.R., and Park, W.H. (2010). The effects of antimycin A on endothelial cells in cell death, reactive oxygen species and GSH levels. Toxicol In Vitro *24*, 1111–1118. 10.1016/j.tiv.2010.03.009.
33. Demine, S., Renard, P., and Arnould, T. (2019). Mitochondrial Uncoupling: A Key Controller of Biological Processes in Physiology and Diseases. Cells *8*. 10.3390/cells8080795.
34. Leichner, J.M., Konyukhov, E., Kamoun, D., and Yaniv, Y. (2019). Real time mitochondrial dimension measurements. J Biol Methods *6*, e111. 10.14440/jbm.2019.262.

35. Wai, T., and Langer, T. (2016). Mitochondrial Dynamics and Metabolic Regulation. Trends in Endocrinology & Metabolism *27*, 105–117. https://doi.org/10.1016/j.tem.2015.12.001.
36. Labbe, K., Murley, A., and Nunnari, J. (2014). Determinants and functions of mitochondrial behavior. Annu Rev Cell Dev Biol *30*, 357–391. 10.1146/annurev-cellbio-101011-155756.
37. Anand, R., Langer, T., and Baker, M.J. (2013). Proteolytic control of mitochondrial function and morphogenesis. Biochim Biophys Acta *1833*, 195–204. 10.1016/j.bbamcr.2012.06.025.
38. Griparic, L., and van der Bliek, A.M. (2001). The many shapes of mitochondrial membranes. Traffic *2*, 235–244. 10.1034/j.1600-0854.2001.1r008.x.
39. Chen, H., Detmer, S.A., Ewald, A.J., Griffin, E.E., Fraser, S.E., and Chan, D.C. (2003). Mitofusins Mfn1 and Mfn2 coordinately regulate mitochondrial fusion and are essential for embryonic development. J Cell Biol *160*, 189–200. 10.1083/jcb.200211046.
40. Zanna, C., Ghelli, A., Porcelli, A.M., Karbowski, M., Youle, R.J., Schimpf, S., Wissinger, B., Pinti, M., Cossarizza, A., Vidoni, S., et al. (2008). OPA1 mutations associated with dominant optic atrophy impair oxidative phosphorylation and mitochondrial fusion. Brain *131*, 352–367. 10.1093/brain/awm335.
41. Smirnova, E., Griparic, L., Shurland, D.L., and van der Bliek, A.M. (2001). Dynamin-related protein Drp1 is required for mitochondrial division in mammalian cells. Mol Biol Cell *12*, 2245–2256. 10.1091/mbc.12.8.2245.
42. Kan, K.T., Wilcock, J., and Lu, H. (2024). Role of Yme1 in mitochondrial protein homeostasis: from regulation of protein import, OXPHOS function to lipid synthesis and mitochondrial dynamics. Biochem Soc Trans *52*, 1539–1548. 10.1042/bst20240450.
43. Ruan, Y., Li, H., Zhang, K., Jian, F., Tang, J., and Song, Z. (2013). Loss of Yme1L perturbates mitochondrial dynamics. Cell Death Dis *4*, e896. 10.1038/cddis.2013.414.
44. Stiburek, L., Cesnekova, J., Kostkova, O., Fornuskova, D., Vinsova, K., Wenchich, L., Houstek, J., and Zeman, J. (2012). YME1L controls the accumulation of respiratory chain subunits and is required for apoptotic resistance, cristae morphogenesis, and cell proliferation. Mol Biol Cell *23*, 1010–1023. 10.1091/mbc.E11-08-0674.
45. Richter, F., Dennerlein, S., Nikolov, M., Jans, D.C., Naumenko, N., Aich, A., MacVicar, T., Linden, A., Jakobs, S., Urlaub, H., et al. (2018). ROMO1 is a constituent of the human presequence translocase required for YME1L protease import. Journal of Cell Biology *218*, 598–614. 10.1083/jcb.201806093.
46. Wu, X., Li, L., and Jiang, H. (2017). Mitochondrial inner-membrane protease Yme1 degrades outer-membrane proteins Tom22 and Om45. Journal of Cell Biology *217*, 139–149. 10.1083/jcb.201702125.
47. Anand, R., Wai, T., Baker, M.J., Kladt, N., Schauss, A.C., Rugarli, E., and Langer, T. (2014). The i-AAA protease YME1L and OMA1 cleave OPA1 to balance mitochondrial fusion and fission. Journal of Cell Biology *204*, 919–929. 10.1083/jcb.201308006.
48. Wai, T., Saita, S., Nolte, H., Müller, S., König, T., Richter-Dennerlein, R., Sprenger, H.G., Madrenas, J., Mühlmeister, M., Brandt, U., et al. (2016). The membrane scaffold SLP2 anchors a proteolytic hub in mitochondria containing PARL and the i‐AAA protease YME1L. EMBO reports *17*, 1844–1856. https://doi.org/10.15252/embr.201642698.
49. Ohba, Y., MacVicar, T., and Langer, T. (2020). Regulation of mitochondrial plasticity by the i-AAA protease YME1L. Biol Chem *401*, 877–890. 10.1515/hsz-2020-0120.
50. MacVicar, T., Ohba, Y., Nolte, H., Mayer, F.C., Tatsuta, T., Sprenger, H.-G., Lindner, B., Zhao, Y., Li, J., Bruns, C., et al. (2019). Lipid signalling drives proteolytic rewiring of mitochondria by YME1L. Nature *575*, 361–365. 10.1038/s41586-019-1738-6.
51. MacVicar, T., Ohba, Y., Nolte, H., Mayer, F.C., Tatsuta, T., Sprenger, H.G., Lindner, B., Zhao, Y., Li, J., Bruns, C., et al. (2019). Lipid signalling drives proteolytic rewiring of mitochondria by YME1L. Nature *575*, 361–365. 10.1038/s41586-019-1738-6.

52. Wai, T., García-Prieto, J., Baker, M.J., Merkwirth, C., Benit, P., Rustin, P., Rupérez, F.J., Barbas, C., Ibañez, B., and Langer, T. (2015). Imbalanced OPA1 processing and mitochondrial fragmentation cause heart failure in mice. Science *350*, aad0116. doi:10.1126/science.aad0116.
53. Sprenger, H.G., Wani, G., Hesseling, A., König, T., Patron, M., MacVicar, T., Ahola, S., Wai, T., Barth, E., Rugarli, E.I., et al. (2019). Loss of the mitochondrial i‐AAA protease YME1L leads to ocular dysfunction and spinal axonopathy. EMBO Molecular Medicine *11*, e9288. https://doi.org/10.15252/emmm.201809288.
54. Sprenger, H.G., MacVicar, T., Bahat, A., Fiedler, K.U., Hermans, S., Ehrentraut, D., Ried, K., Milenkovic, D., Bonekamp, N., Larsson, N.G., et al. (2021). Cellular pyrimidine imbalance triggers mitochondrial DNA-dependent innate immunity. Nat Metab *3*, 636–650. 10.1038/s42255-021-00385-9.
55. Lee, Y.J., Kim, G.H., Park, S.I., and Lim, J.H. (2020). Down-regulation of the mitochondrial i-AAA protease Yme1L induces muscle atrophy via FoxO3a and myostatin activation. J Cell Mol Med *24*, 899–909. 10.1111/jcmm.14799.
56. Käser, M., Kambacheld, M., Kisters-Woike, B., and Langer, T. (2003). Oma1, a Novel Membrane-bound Metallopeptidase in Mitochondria with Activities Overlapping with the m-AAA Protease*. Journal of Biological Chemistry *278*, 46414–46423. https://doi.org/10.1074/jbc.M305584200.
57. Alavi, M.V. (2021). OMA1-An integral membrane protease? Biochim Biophys Acta Proteins Proteom *1869*, 140558. 10.1016/j.bbapap.2020.140558.
58. Zhang, K., Li, H., and Song, Z. (2014). Membrane depolarization activates the mitochondrial protease OMA1 by stimulating self-cleavage. EMBO Rep *15*, 576–585. 10.1002/embr.201338240.
59. Rainbolt, T.K., Lebeau, J., Puchades, C., and Wiseman, R.L. (2016). Reciprocal Degradation of YME1L and OMA1 Adapts Mitochondrial Proteolytic Activity during Stress. Cell Rep *14*, 2041–2049. 10.1016/j.celrep.2016.02.011.
60. Guo, X., Aviles, G., Liu, Y., Tian, R., Unger, B.A., Lin, Y.T., Wiita, A.P., Xu, K., Correia, M.A., and Kampmann, M. (2020). Mitochondrial stress is relayed to the cytosol by an OMA1-DELE1-HRI pathway. Nature *579*, 427–432. 10.1038/s41586-020-2078-2.
61. Ehses, S., Raschke, I., Mancuso, G., Bernacchia, A., Geimer, S., Tondera, D., Martinou, J.-C., Westermann, B., Rugarli, E.I., and Langer, T. (2009). Regulation of OPA1 processing and mitochondrial fusion by m-AAA protease isoenzymes and OMA1. Journal of Cell Biology *187*, 1023–1036.
62. Siebert, V., Silber, M., Heuten, E., Muhle-Goll, C., and Lemberg, M.K. (2022). Cleavage of mitochondrial homeostasis regulator PGAM5 by the intramembrane protease PARL is governed by transmembrane helix dynamics and oligomeric state. J Biol Chem *298*, 102321. 10.1016/j.jbc.2022.102321.
63. Kroczek, L., Nolte, H., Lasarzewski, Y., Molinié, T., Pinero, D.C., Lemke, K., Rugarli, E., and Langer, T. (2025). Stress adaptation of mitochondrial protein import by OMA1-mediated degradation of DNAJC15. bioRxiv, 2025.2003. 2004.641455.
64. Sekine, S., Wang, C., Sideris, D.P., Bunker, E., Zhang, Z., and Youle, R.J. (2019). Reciprocal Roles of Tom7 and OMA1 during Mitochondrial Import and Activation of PINK1. Mol Cell *73*, 1028–1043.e1025. 10.1016/j.molcel.2019.01.002.
65. Rivera-Mejías, P., Narbona-Pérez Á, J., Hasberg, L., Kroczek, L., Bahat, A., Lawo, S., Folz-Donahue, K., Schumacher, A.L., Ahola, S., Mayer, F.C., et al. (2023). The mitochondrial protease OMA1 acts as a metabolic safeguard upon nuclear DNA damage. Cell Rep *42*, 112332. 10.1016/j.celrep.2023.112332.
66. Quirós, P.M., Ramsay, A.J., Sala, D., Fernández-Vizarra, E., Rodríguez, F., Peinado, J.R., Fernández-García, M.S., Vega, J.A., Enríquez, J.A., Zorzano, A., and López-Otín, C. (2012). Loss of mitochondrial protease OMA1 alters processing of the GTPase OPA1 and causes

obesity and defective thermogenesis in mice. Embo j *31*, 2117–2133. 10.1038/emboj.2012.70.

67. Korwitz, A., Merkwirth, C., Richter-Dennerlein, R., Tröder, S.E., Sprenger, H.G., Quirós, P.M., López-Otín, C., Rugarli, E.I., and Langer, T. (2016). Loss of OMA1 delays neurodegeneration by preventing stress-induced OPA1 processing in mitochondria. J Cell Biol *212*, 157–166. 10.1083/jcb.201507022.
68. Ahola, S., Rivera Mejías, P., Hermans, S., Chandragiri, S., Giavalisco, P., Nolte, H., and Langer, T. (2022). OMA1-mediated integrated stress response protects against ferroptosis in mitochondrial cardiomyopathy. Cell Metab *34*, 1875–1891.e1877. 10.1016/j.cmet.2022.08.017.
69. Gilkerson, R., De La Torre, P., and St Vallier, S. (2021). Mitochondrial OMA1 and OPA1 as Gatekeepers of Organellar Structure/Function and Cellular Stress Response. Front Cell Dev Biol *9*, 626117. 10.3389/fcell.2021.626117.
70. Cipolat, S., Martins de Brito, O., Dal Zilio, B., and Scorrano, L. (2004). OPA1 requires mitofusin 1 to promote mitochondrial fusion. Proc Natl Acad Sci U S A *101*, 15927–15932. 10.1073/pnas.0407043101.
71. Aguer, C., Gambarotta, D., Mailloux, R.J., Moffat, C., Dent, R., McPherson, R., and Harper, M.E. (2011). Galactose enhances oxidative metabolism and reveals mitochondrial dysfunction in human primary muscle cells. PLoS One *6*, e28536. 10.1371/journal.pone.0028536.
72. Hu, C., Shu, L., Huang, X., Yu, J., Li, L., Gong, L., Yang, M., Wu, Z., Gao, Z., Zhao, Y., et al. (2020). OPA1 and MICOS Regulate mitochondrial crista dynamics and formation. Cell Death Dis *11*, 940. 10.1038/s41419-020-03152-y.
73. Cartes-Saavedra, B., Lagos, D., Macuada, J., Arancibia, D., Burté, F., Sjöberg-Herrera, M.K., Andrés, M.E., Horvath, R., Yu-Wai-Man, P., Hajnóczky, G., and Eisner, V. (2023). OPA1 disease-causing mutants have domain-specific effects on mitochondrial ultrastructure and fusion. Proc Natl Acad Sci U S A *120*, e2207471120. 10.1073/pnas.2207471120.
74. Wang, L., Wei, Q., Xu, R., Chen, Y., Li, S., Bu, Q., Zhao, Y., Li, H., Zhao, Y., Jiang, L., et al. (2023). Cardiolipin and OPA1 Team up for Methamphetamine-Induced Locomotor Activity by Promoting Neuronal Mitochondrial Fusion in the Nucleus Accumbens of Mice. ACS Chem Neurosci *14*, 1585–1601. 10.1021/acschemneuro.2c00709.
75. Ge, Y., Shi, X., Boopathy, S., McDonald, J., Smith, A.W., and Chao, L.H. (2020). Two forms of Opa1 cooperate to complete fusion of the mitochondrial inner-membrane. Elife *9*. 10.7554/eLife.50973.
76. Li, D., Wang, J., Jin, Z., and Zhang, Z. (2019). Structural and evolutionary characteristics of dynamin-related GTPase OPA1. PeerJ *7*, e7285. 10.7717/peerj.7285.
77. Nyenhuis, S.B., Wu, X., Strub, M.-P., Yim, Y.-I., Stanton, A.E., Baena, V., Syed, Z.A., Canagarajah, B., Hammer, J.A., and Hinshaw, J.E. (2023). OPA1 helical structures give perspective to mitochondrial dysfunction. Nature *620*, 1109–1116. 10.1038/s41586-023-06462-1.
78. MacVicar, T., and Langer, T. (2016). OPA1 processing in cell death and disease – the long and short of it. Journal of Cell Science *129*, 2297–2306. 10.1242/jcs.159186.
79. Delettre, C., Lenaers, G., Griffoin, J.-M., Gigarel, N., Lorenzo, C., Belenguer, P., Pelloquin, L., Grosgeorge, J., Turc-Carel, C., and Perret, E. (2000). Nuclear gene OPA1, encoding a mitochondrial dynamin-related protein, is mutated in dominant optic atrophy. Nature genetics *26*, 207–210.
80. Scorrano, L., Ashiya, M., Buttle, K., Weiler, S., Oakes, S.A., Mannella, C.A., and Korsmeyer, S.J. (2002). A distinct pathway remodels mitochondrial cristae and mobilizes cytochrome c during apoptosis. Developmental cell *2*, 55–67.
81. Elachouri, G., Vidoni, S., Zanna, C., Pattyn, A., Boukhaddaoui, H., Gaget, K., Yu-Wai-Man, P., Gasparre, G., Sarzi, E., and Delettre, C. (2011). OPA1 links human mitochondrial

genome maintenance to mtDNA replication and distribution. Genome research *21*, 12–20.

82. Del Dotto, V., Mishra, P., Vidoni, S., Fogazza, M., Maresca, A., Caporali, L., McCaffery, J.M., Cappelletti, M., Baruffini, E., Lenaers, G., et al. (2017). OPA1 Isoforms in the Hierarchical Organization of Mitochondrial Functions. Cell Reports *19*, 2557–2571. 10.1016/j.celrep.2017.05.073.
83. Chen, H., Chomyn, A., and Chan, D.C. (2005). Disruption of fusion results in mitochondrial heterogeneity and dysfunction. J Biol Chem *280*, 26185–26192. 10.1074/jbc.M503062200.
84. Malsburg, A. (2024). Die Rolle von OPA1 bei der Fusion von Mitochondrien. BIOspektrum *30*, 410–413. 10.1007/s12268-024-2220-z.
85. Kawano, I., Bazila, B., Jezek, P., and Dlaskova, A. (2023). Mitochondrial Dynamics and Cristae Shape Changes During Metabolic Reprogramming. Antioxid Redox Signal *39*, 684–707. 10.1089/ars.2023.0268.
86. Cogliati, S., Enriquez, J.A., and Scorrano, L. (2016). Mitochondrial Cristae: Where Beauty Meets Functionality. Trends Biochem Sci *41*, 261–273. 10.1016/j.tibs.2016.01.001.
87. Scorrano, L., Ashiya, M., Buttle, K., Weiler, S., Oakes, S.A., Mannella, C.A., and Korsmeyer, S.J. (2002). A distinct pathway remodels mitochondrial cristae and mobilizes cytochrome c during apoptosis. Dev Cell *2*, 55–67. 10.1016/s1534-5807(01)00116-2.
88. Caron, C., and Bertolin, G. (2024). Cristae shaping and dynamics in mitochondrial function. J Cell Sci *137*. 10.1242/jcs.260986.
89. Siegmund, S.E., Grassucci, R., Carter, S.D., Barca, E., Farino, Z.J., Juanola-Falgarona, M., Zhang, P., Tanji, K., Hirano, M., Schon, E.A., et al. (2018). Three-Dimensional Analysis of Mitochondrial Crista Ultrastructure in a Patient with Leigh Syndrome by In Situ Cryoelectron Tomography. iScience *6*, 83–91. 10.1016/j.isci.2018.07.014.
90. Harner, M.E., Unger, A.K., Geerts, W.J., Mari, M., Izawa, T., Stenger, M., Geimer, S., Reggiori, F., Westermann, B., and Neupert, W. (2016). An evidence based hypothesis on the existence of two pathways of mitochondrial crista formation. Elife *5*. 10.7554/eLife.18853.
91. Yu, J., Luo, Y., Lin, J., Li, Z., Fang, Z., He, H., Yan, C., and Song, Z. (2025). Mitochondrial cristae remodeling: Mechanisms, functions, and pathology. Cell Insight *4*, 100285. 10.1016/j.cellin.2025.100285.
92. Stephan, T., Bruser, C., Deckers, M., Steyer, A.M., Balzarotti, F., Barbot, M., Behr, T.S., Heim, G., Hubner, W., Ilgen, P., et al. (2020). MICOS assembly controls mitochondrial inner membrane remodeling and crista junction redistribution to mediate cristae formation. EMBO J *39*, e104105. 10.15252/embj.2019104105.
93. Patten, D.A., Wong, J., Khacho, M., Soubannier, V., Mailloux, R.J., Pilon-Larose, K., MacLaurin, J.G., Park, D.S., McBride, H.M., Trinkle-Mulcahy, L., et al. (2014). OPA1-dependent cristae modulation is essential for cellular adaptation to metabolic demand. EMBO J *33*, 2676–2691. 10.15252/embj.201488349.
94. Fry, M.Y., Navarro, P.P., Hakim, P., Ananda, V.Y., Qin, X., Landoni, J.C., Rath, S., Inde, Z., Lugo, C.M., Luce, B.E., et al. (2024). In situ architecture of Opa1-dependent mitochondrial cristae remodeling. EMBO J *43*, 391–413. 10.1038/s44318-024-00027-2.
95. Frezza, C., Cipolat, S., Martins de Brito, O., Micaroni, M., Beznoussenko, G.V., Rudka, T., Bartoli, D., Polishuck, R.S., Danial, N.N., De Strooper, B., and Scorrano, L. (2006). OPA1 controls apoptotic cristae remodeling independently from mitochondrial fusion. Cell *126*, 177–189. 10.1016/j.cell.2006.06.025.
96. Hardie, D.G. (2011). AMP-activated protein kinase: an energy sensor that regulates all aspects of cell function. Genes Dev *25*, 1895–1908. 10.1101/gad.17420111.
97. Lin, J., Handschin, C., and Spiegelman, B.M. (2005). Metabolic control through the PGC-1 family of transcription coactivators. Cell Metab *1*, 361–370. 10.1016/j.cmet.2005.05.004.

98. Neupert, W. (1997). Protein import into mitochondria. Annual review of biochemistry *66*, 863–917.
99. Pfanner, N., Craig, E.A., and Hönlinger, A. (1997). Mitochondrial preprotein translocase. Annual review of cell and developmental biology *13*, 25–51.
100. Lim, J.H., Martin, F., Guiard, B., Pfanner, N., and Voos, W. (2001). The mitochondrial Hsp70-dependent import system actively unfolds preproteins and shortens the lag phase of translocation. The EMBO Journal *20*, 941–950. https://doi.org/10.1093/emboj/20.5.941.
101. Decker, S.T., and Funai, K. (2024). Mitochondrial membrane lipids in the regulation of bioenergetic flux. Cell Metab *36*, 1963–1978. 10.1016/j.cmet.2024.07.024.
102. Cockcroft, S., and Raghu, P. (2018). Phospholipid transport protein function at organelle contact sites. Curr Opin Cell Biol *53*, 52–60. 10.1016/j.ceb.2018.04.011.
103. Quiles, J.M., and Gustafsson, A.B. (2020). Mitochondrial Quality Control and Cellular Proteostasis: Two Sides of the Same Coin. Front Physiol *11*, 515. 10.3389/fphys.2020.00515.
104. Held, N.M., and Houtkooper, R.H. (2015). Mitochondrial quality control pathways as determinants of metabolic health. Bioessays *37*, 867–876. 10.1002/bies.201500013.
105. Baker, M.J., Yek, K.Q., and Stojanovski, D. (2025). Quality control at the powerhouse: mitochondrial proteostasis dysfunction and disease. Biochem Soc Trans *53*, 1–13. 10.1042/BST20253044.
106. Baker, M.J., Tatsuta, T., and Langer, T. (2011). Quality control of mitochondrial proteostasis. Cold Spring Harb Perspect Biol *3*. 10.1101/cshperspect.a007559.
107. Johns, A., Higuchi-Sanabria, R., Thorwald, M.A., and Vilchez, D. (2023). A tale of two pathways: Regulation of proteostasis by UPR(mt) and MDPs. Curr Opin Neurobiol *78*, 102673. 10.1016/j.conb.2022.102673.
108. Ron, D., and Walter, P. (2007). Signal integration in the endoplasmic reticulum unfolded protein response. Nat Rev Mol Cell Biol *8*, 519–529. 10.1038/nrm2199.
109. Fessler, E., Eckl, E.M., Schmitt, S., Mancilla, I.A., Meyer-Bender, M.F., Hanf, M., Philippou-Massier, J., Krebs, S., Zischka, H., and Jae, L.T. (2020). A pathway coordinated by DELE1 relays mitochondrial stress to the cytosol. Nature *579*, 433–437. 10.1038/s41586-020-2076-4.
110. Fessler, E., Krumwiede, L., and Jae, L.T. (2022). DELE1 tracks perturbed protein import and processing in human mitochondria. Nat Commun *13*, 1853. 10.1038/s41467-022-29479-y.
111. Pakos-Zebrucka, K., Koryga, I., Mnich, K., Ljujic, M., Samali, A., and Gorman, A.M. (2016). The integrated stress response. EMBO reports *17*, 1374–1395. https://doi.org/10.15252/embr.201642195.
112. Costa-Mattioli, M., and Walter, P. (2020). The integrated stress response: From mechanism to disease. Science *368*. 10.1126/science.aat5314.
113. Harding, H.P., Novoa, I., Zhang, Y., Zeng, H., Wek, R., Schapira, M., and Ron, D. (2000). Regulated translation initiation controls stress-induced gene expression in mammalian cells. Mol Cell *6*, 1099–1108. 10.1016/s1097-2765(00)00108-8.
114. Pakos-Zebrucka, K., Koryga, I., Mnich, K., Ljujic, M., Samali, A., and Gorman, A.M. (2016). The integrated stress response. EMBO Rep *17*, 1374–1395. 10.15252/embr.201642195.
115. Popov, L.D. (2022). Mitochondrial-derived vesicles: Recent insights. J Cell Mol Med *26*, 3323–3328. 10.1111/jcmm.17391.
116. Sen, A., Kallabis, S., Gaedke, F., Jungst, C., Boix, J., Nuchel, J., Maliphol, K., Hofmann, J., Schauss, A.C., Kruger, M., et al. (2022). Mitochondrial membrane proteins and VPS35 orchestrate selective removal of mtDNA. Nat Commun *13*, 6704. 10.1038/s41467-022-34205-9.
117. Springer, W., and Kahle, P.J. (2011). Regulation of PINK1-Parkin-mediated mitophagy. Autophagy *7*, 266–278. 10.4161/auto.7.3.14348.

118. Zhou, T.-Y., Ma, R.-X., Li, J., Zou, B., Yang, H., Ma, R.-Y., Wu, Z.-Q., Li, J., and Yao, Y. (2023). Review of PINK1-Parkin-mediated mitochondrial autophagy in Alzheimer's disease. European Journal of Pharmacology *959*, 176057. https://doi.org/10.1016/j.ejphar.2023.176057.
119. Narendra, D., Tanaka, A., Suen, D.F., and Youle, R.J. (2008). Parkin is recruited selectively to impaired mitochondria and promotes their autophagy. J Cell Biol *183*, 795–803. 10.1083/jcb.200809125.
120. Shi, R.Y., Zhu, S.H., Li, V., Gibson, S.B., Xu, X.S., and Kong, J.M. (2014). BNIP3 interacting with LC3 triggers excessive mitophagy in delayed neuronal death in stroke. CNS Neurosci Ther *20*, 1045–1055. 10.1111/cns.12325.
121. Lampert, M.A., Orogo, A.M., Najor, R.H., Hammerling, B.C., Leon, L.J., Wang, B.J., Kim, T., Sussman, M.A., and Gustafsson, A.B. (2019). BNIP3L/NIX and FUNDC1-mediated mitophagy is required for mitochondrial network remodeling during cardiac progenitor cell differentiation. Autophagy *15*, 1182–1198. 10.1080/15548627.2019.1580095.
122. Kuang, Y., Ma, K., Zhou, C., Ding, P., Zhu, Y., Chen, Q., and Xia, B. (2016). Structural basis for the phosphorylation of FUNDC1 LIR as a molecular switch of mitophagy. Autophagy *12*, 2363–2373. 10.1080/15548627.2016.1238552.
123. Egan, D.F., Shackelford, D.B., Mihaylova, M.M., Gelino, S., Kohnz, R.A., Mair, W., Vasquez, D.S., Joshi, A., Gwinn, D.M., and Taylor, R. (2011). Phosphorylation of ULK1 (hATG1) by AMP-activated protein kinase connects energy sensing to mitophagy. Science *331*, 456–461.
124. Cetrullo, S., D'Adamo, S., Tantini, B., Borzi, R.M., and Flamigni, F. (2015). mTOR, AMPK, and Sirt1: Key Players in Metabolic Stress Management. Crit Rev Eukaryot Gene Expr *25*, 59–75. 10.1615/critreveukaryotgeneexpr.2015012975.
125. Saxton, R.A., and Sabatini, D.M. (2017). mTOR Signaling in Growth, Metabolism, and Disease. Cell *168*, 960–976. 10.1016/j.cell.2017.02.004.
126. Morgan, M.J., and Liu, Z.G. (2011). Crosstalk of reactive oxygen species and NF-κB signaling. Cell Res *21*, 103–115. 10.1038/cr.2010.178.
127. Sancak, Y., Markhard, A.L., Kitami, T., Kovács-Bogdán, E., Kamer, K.J., Udeshi, N.D., Carr, S.A., Chaudhuri, D., Clapham, D.E., Li, A.A., et al. (2013). EMRE is an essential component of the mitochondrial calcium uniporter complex. Science *342*, 1379–1382. 10.1126/science.1242993.
128. Baumgartner, H.K., Gerasimenko, J.V., Thorne, C., Ferdek, P., Pozzan, T., Tepikin, A.V., Petersen, O.H., Sutton, R., Watson, A.J., and Gerasimenko, O.V. (2009). Calcium elevation in mitochondria is the main Ca2+ requirement for mitochondrial permeability transition pore (mPTP) opening. Journal of Biological Chemistry *284*, 20796–20803.
129. Gincel, D., Zaid, H., and Shoshan-Barmatz, V. (2001). Calcium binding and translocation by the voltage-dependent anion channel: a possible regulatory mechanism in mitochondrial function. Biochem J *358*, 147–155. 10.1042/0264-6021:3580147.
130. Chen, S., Sun, Y., Qin, Y., Yang, L., Hao, Z., Xu, Z., Björklund, M., Liu, W., and Hong, Z. (2024). Dynamic interaction of REEP5-MFN1/2 enables mitochondrial hitchhiking on tubular ER. J Cell Biol *223*. 10.1083/jcb.202304031.
131. Bartok, A., Weaver, D., Golenár, T., Nichtova, Z., Katona, M., Bánsághi, S., Alzayady, K.J., Thomas, V.K., Ando, H., Mikoshiba, K., et al. (2019). IP3 receptor isoforms differently regulate ER-mitochondrial contacts and local calcium transfer. Nature Communications *10*, 3726. 10.1038/s41467-019-11646-3.
132. Kluck, R.M., Bossy-Wetzel, E., Green, D.R., and Newmeyer, D.D. (1997). The Release of Cytochrome c from Mitochondria: A Primary Site for Bcl-2 Regulation of Apoptosis. Science *275*, 1132–1136. doi:10.1126/science.275.5303.1132.
133. Zou, H., Li, Y., Liu, X., and Wang, X. (1999). An APAF-1·Cytochrome c Multimeric Complex Is a Functional Apoptosome That Activates Procaspase-9*. Journal of Biological Chemistry *274*, 11549–11556. https://doi.org/10.1074/jbc.274.17.11549.

134. Ghisletti, S., and Russo, M. (2025). TCA-cycle metabolites in the nucleus: drivers of chromatin and epigenetic control. BMC Biol *23*, 316. 10.1186/s12915-025-02423-4.
135. Martinez-Reyes, I., and Chandel, N.S. (2020). Mitochondrial TCA cycle metabolites control physiology and disease. Nat Commun *11*, 102. 10.1038/s41467-019-13668-3.
136. Zhang, C., Meng, Y., and Han, J. (2024). Emerging roles of mitochondrial functions and epigenetic changes in the modulation of stem cell fate. Cell Mol Life Sci *81*, 26. 10.1007/s00018-023-05070-6.
137. Devall, M., Roubroeks, J., Mill, J., Weedon, M., and Lunnon, K. (2016). Epigenetic regulation of mitochondrial function in neurodegenerative disease: New insights from advances in genomic technologies. Neurosci Lett *625*, 47–55. 10.1016/j.neulet.2016.02.013.
138. Santos, J.H. (2021). Mitochondria signaling to the epigenome: A novel role for an old organelle. Free Radic Biol Med *170*, 59–69. 10.1016/j.freeradbiomed.2020.11.016.
139. Su, X., Wellen, K.E., and Rabinowitz, J.D. (2016). Metabolic control of methylation and acetylation. Curr Opin Chem Biol *30*, 52–60. 10.1016/j.cbpa.2015.10.030.
140. Shaw, A.E., Hughes, J., Gu, Q., Behdenna, A., Singer, J.B., Dennis, T., Orton, R.J., Varela, M., Gifford, R.J., Wilson, S.J., and Palmarini, M. (2017). Fundamental properties of the mammalian innate immune system revealed by multispecies comparison of type I interferon responses. PLOS Biology *15*, e2004086. 10.1371/journal.pbio.2004086.
141. Sun, L., Wu, J., Du, F., Chen, X., and Chen, Z.J. (2013). Cyclic GMP-AMP synthase is a cytosolic DNA sensor that activates the type I interferon pathway. Science *339*, 786–791. 10.1126/science.1232458.
142. Tanaka, Y., and Chen, Z.J. (2012). STING specifies IRF3 phosphorylation by TBK1 in the cytosolic DNA signaling pathway. Sci Signal *5*, ra20. 10.1126/scisignal.2002521.
143. Stark, G.R., and Darnell, J.E., Jr. (2012). The JAK-STAT pathway at twenty. Immunity *36*, 503–514. 10.1016/j.immuni.2012.03.013.
144. West, A.P., and Shadel, G.S. (2017). Mitochondrial DNA in innate immune responses and inflammatory pathology. Nat Rev Immunol *17*, 363–375. 10.1038/nri.2017.21.
145. Xian, H., Watari, K., Sanchez-Lopez, E., Offenberger, J., Onyuru, J., Sampath, H., Ying, W., Hoffman, H.M., Shadel, G.S., and Karin, M. (2022). Oxidized DNA fragments exit mitochondria via mPTP- and VDAC-dependent channels to activate NLRP3 inflammasome and interferon signaling. Immunity *55*, 1370–1385.e1378. 10.1016/j.immuni.2022.06.007.
146. McArthur, K., Whitehead, L.W., Heddleston, J.M., Li, L., Padman, B.S., Oorschot, V., Geoghegan, N.D., Chappaz, S., Davidson, S., San Chin, H., et al. (2018). BAK/BAX macropores facilitate mitochondrial herniation and mtDNA efflux during apoptosis. Science *359*, eaao6047. doi:10.1126/science.aao6047.
147. Lu, T., Zhang, Z., Bi, Z., Lan, T., Zeng, H., Liu, Y., Mo, F., Yang, J., Chen, S., He, X., et al. (2023). TFAM deficiency in dendritic cells leads to mitochondrial dysfunction and enhanced antitumor immunity through cGAS-STING pathway. J Immunother Cancer *11*. 10.1136/jitc-2022-005430.
148. Mao, E.Y.C., Yen, H.-Y., and Wu, C.-C. (2024). Structural basis of how MGME1 processes DNA 5' ends to maintain mitochondrial genome integrity. Nucleic Acids Research *52*, 4067–4078. 10.1093/nar/gkae186.
149. Milenkovic, D., Sanz-Moreno, A., Calzada-Wack, J., Rathkolb, B., Veronica Amarie, O., Gerlini, R., Aguilar-Pimentel, A., Misic, J., Simard, M.-L., Wolf, E., et al. (2022). Mice lacking the mitochondrial exonuclease MGME1 develop inflammatory kidney disease with glomerular dysfunction. PLOS Genetics *18*, e1010190. 10.1371/journal.pgen.1010190.
150. Wei, F.L., Wang, T.F., Wang, C.L., Zhang, Z.P., Zhao, J.W., Heng, W., Tang, Z., Du, M.R., Yan, X.D., Li, X.X., et al. (2024). Cytoplasmic Escape of Mitochondrial DNA Mediated by Mfn2 Downregulation Promotes Microglial Activation via cGas-Sting Axis in Spinal Cord Injury. Adv Sci (Weinh) *11*, e2305442. 10.1002/advs.202305442.

151. He, B., Yu, H., Liu, S., Wan, H., Fu, S., Liu, S., Yang, J., Zhang, Z., Huang, H., Li, Q., et al. (2022). Mitochondrial cristae architecture protects against mtDNA release and inflammation. Cell Rep *41*, 111774. 10.1016/j.celrep.2022.111774.
152. Sugiura, A., McLelland, G.L., Fon, E.A., and McBride, H.M. (2014). A new pathway for mitochondrial quality control: mitochondrial-derived vesicles. The EMBO Journal *33*, 2142–2156. https://doi.org/10.15252/embj.201488104.
153. Zecchini, V., Paupe, V., Herranz-Montoya, I., Janssen, J., Wortel, I.M.N., Morris, J.L., Ferguson, A., Chowdury, S.R., Segarra-Mondejar, M., Costa, A.S.H., et al. (2023). Fumarate induces vesicular release of mtDNA to drive innate immunity. Nature *615*, 499–506. 10.1038/s41586-023-05770-w.
154. Heilig, R., Lee, J., and Tait, S.W.G. (2023). Mitochondrial DNA in cell death and inflammation. Biochem Soc Trans *51*, 457–472. 10.1042/BST20221525.
155. Qiu, J., Yue, F., Zhu, P., Chen, J., Xu, F., Zhang, L., Kim, K.H., Snyder, M.M., Luo, N., Xu, H.-w., et al. (2023). FAM210A is essential for cold-induced mitochondrial remodeling in brown adipocytes. Nature Communications *14*, 6344. 10.1038/s41467-023-41988-y.
156. Wu, J., Venkata Subbaiah, K.C., Jiang, F., Hedaya, O., Mohan, A., Yang, T., Welle, K., Ghaemmaghami, S., Tang, W.H.W., Small, E., et al. (2021). MicroRNA-574 regulates FAM210A expression and influences pathological cardiac remodeling. EMBO Molecular Medicine *13*, e12710. https://doi.org/10.15252/emmm.202012710.
157. Wang, Y., and Yue, F. (2024). FAM210A: An emerging regulator of mitochondrial homeostasis. Bioessays *46*, e2400090. 10.1002/bies.202400090.
158. Chen, J., Yue, F., Kim, K.H., Zhu, P., Qiu, J., Tao, W.A., and Kuang, S. (2023). FAM210A mediates an inter-organelle crosstalk essential for protein synthesis and muscle growth in mouse. bioRxiv. 10.1101/2023.08.03.551853.
159. Wu, J., Subbaiah, K.C.V., Hedaya, O., Chen, S., Munger, J., Tang, W.H.W., Yan, C., and Yao, P. (2023). FAM210A regulates mitochondrial translation and maintains cardiac mitochondrial homeostasis. Cardiovasc Res *119*, 2441–2457. 10.1093/cvr/cvad124.
160. Tezze, C., Romanello, V., Desbats, M.A., Fadini, G.P., Albiero, M., Favaro, G., Ciciliot, S., Soriano, M.E., Morbidoni, V., Cerqua, C., et al. (2017). Age-Associated Loss of OPA1 in Muscle Impacts Muscle Mass, Metabolic Homeostasis, Systemic Inflammation, and Epithelial Senescence. Cell Metab *25*, 1374–1389 e1376. 10.1016/j.cmet.2017.04.021.
161. Sterky, F.H., Lee, S., Wibom, R., Olson, L., and Larsson, N.G. (2011). Impaired mitochondrial transport and Parkin-independent degeneration of respiratory chain-deficient dopamine neurons in vivo. Proc Natl Acad Sci U S A *108*, 12937–12942. 10.1073/pnas.1103295108.
162. Elachouri, G., Vidoni, S., Zanna, C., Pattyn, A., Boukhaddaoui, H., Gaget, K., Yu-Wai-Man, P., Gasparre, G., Sarzi, E., Delettre, C., et al. (2011). OPA1 links human mitochondrial genome maintenance to mtDNA replication and distribution. Genome Res *21*, 12–20. 10.1101/gr.108696.110.
163. Lewis, S.C., Uchiyama, L.F., and Nunnari, J. (2016). ER-mitochondria contacts couple mtDNA synthesis with mitochondrial division in human cells. Science *353*, aaf5549. doi:10.1126/science.aaf5549.
164. Lee, H., Smith, S.B., Sheu, S.S., and Yoon, Y. (2020). The short variant of optic atrophy 1 (OPA1) improves cell survival under oxidative stress. J Biol Chem *295*, 6543–6560. 10.1074/jbc.RA119.010983.
165. Farrell, P.J., Broeze, R.J., and Lengyel, P. (1979). Accumulation of an mRNA and protein in interferon-treated Ehrlich ascites tumour cells. Nature *279*, 523–525. 10.1038/279523a0.
166. Pinto-Fernandez, A., Salio, M., Partridge, T., Chen, J., Vere, G., Greenwood, H., Olie, C.S., Damianou, A., Scott, H.C., Pegg, H.J., et al. (2021). Deletion of the deISGylating enzyme USP18 enhances tumour cell antigenicity and radiosensitivity. Br J Cancer *124*, 817–830. 10.1038/s41416-020-01167-y.

167. Der, S.D., Zhou, A., Williams, B.R.G., and Silverman, R.H. (1998). Identification of genes differentially regulated by interferon α, β, or γ using oligonucleotide arrays. Proceedings of the National Academy of Sciences *95*, 15623–15628. doi:10.1073/pnas.95.26.15623.
168. Wang, R., Mishra, P., Garbis, S.D., Moradian, A., Sweredoski, M.J., and Chan, D.C. (2021). Identification of new OPA1 cleavage site reveals that short isoforms regulate mitochondrial fusion. Mol Biol Cell *32*, 157–168. 10.1091/mbc.E20-09-0605.
169. Pilz, A., Ramsauer, K., Heidari, H., Leitges, M., Kovarik, P., and Decker, T. (2003). Phosphorylation of the Stat1 transactivating domain is required for the response to type I interferons. EMBO reports *4*, 368–373. https://doi.org/10.1038/sj.embor.embor802.
170. Rodríguez-Graciani, K.M., Chapa-Dubocq, X.R., MacMillan-Crow, L.A., and Javadov, S. (2020). Association Between L-OPA1 Cleavage and Cardiac Dysfunction During Ischemia-Reperfusion Injury in Rats. Cell Physiol Biochem *54*, 1101–1114. 10.33594/000000303.
171. Valnot, I., von Kleist-Retzow, J.C., Barrientos, A., Gorbatyuk, M., Taanman, J.W., Mehaye, B., Rustin, P., Tzagoloff, A., Munnich, A., and Rotig, A. (2000). A mutation in the human heme A:farnesyltransferase gene (COX10) causes cytochrome c oxidase deficiency. Hum Mol Genet *9*, 1245–1249. 10.1093/hmg/9.8.1245.
172. Molina-Riquelme, I., Barrientos, G., Breitsprecher, L., Gómez, W., Díaz-Castro, F., Morris, S., del Campo, A., Garrido-Olivares, L., Verdejo, H., Psathaki, O.E., et al. (2025). Multi-scale mitochondrial cristae remodeling links Opa1 downregulation to reduced OXPHOS capacity in aged hearts. bioRxiv, 2025.2004.2001.644555. 10.1101/2025.04.01.644555.
173. Klimitz, F.J., Shen, Y., Repetto, F., Brown, S., Knoedler, L., Ko, C.J., Abu Hussein, N., Crisler, W.J., Adams, T., Kaminski, N., et al. (2025). Keratinocytes as active regulators of cutaneous and mucosal immunity: a systematic review across inflammatory epithelial disorders. Frontiers in Immunology *Volume 16 - 2025*. 10.3389/fimmu.2025.1694066.
174. Lei, Y., Guerra Martinez, C., Torres-Odio, S., Bell, S.L., Birdwell, C.E., Bryant, J.D., Tong, C.W., Watson, R.O., West, L.C., and West, A.P. (2021). Elevated type I interferon responses potentiate metabolic dysfunction, inflammation, and accelerated aging in mtDNA mutator mice. Science Advances *7*, eabe7548. doi:10.1126/sciadv.abe7548.
175. Fry, M.Y., Navarro, P.P., Hakim, P., Ananda, V.Y., Qin, X., Landoni, J.C., Rath, S., Inde, Z., Lugo, C.M., Luce, B.E., et al. (2023). In situ architecture of Opa1-dependent mitochondrial cristae remodeling. bioRxiv. 10.1101/2023.01.16.524176.
176. Zhang, D., Zhang, Y., Ma, J., Zhu, C., Niu, T., Chen, W., Pang, X., Zhai, Y., and Sun, F. (2020). Cryo-EM structures of S-OPA1 reveal its interactions with membrane and changes upon nucleotide binding. Elife *9*. 10.7554/eLife.50294.
177. Rühmkorf, A., and Harbauer, A.B. (2023). Role of Mitochondria-ER Contact Sites in Mitophagy. Biomolecules *13*. 10.3390/biom13081198.
178. Silva Ramos, E., Motori, E., Bruser, C., Kuhl, I., Yeroslaviz, A., Ruzzenente, B., Kauppila, J.H.K., Busch, J.D., Hultenby, K., Habermann, B.H., et al. (2019). Mitochondrial fusion is required for regulation of mitochondrial DNA replication. PLoS Genet *15*, e1008085. 10.1371/journal.pgen.1008085.
179. Garcia, I., Innis-Whitehouse, W., Lopez, A., Keniry, M., and Gilkerson, R. (2018). Oxidative insults disrupt OPA1-mediated mitochondrial dynamics in cultured mammalian cells. Redox Rep *23*, 160–167. 10.1080/13510002.2018.1492766.
180. Liemburg-Apers, D.C., Willems, P.H., Koopman, W.J., and Grefte, S. (2015). Interactions between mitochondrial reactive oxygen species and cellular glucose metabolism. Arch Toxicol *89*, 1209–1226. 10.1007/s00204-015-1520-y.
181. Baek, J.H., Gomez, I.G., Wada, Y., Roach, A., Mahad, D., and Duffield, J.S. (2018). Deletion of the Mitochondrial Complex-IV Cofactor Heme A:Farnesyltransferase Causes Focal Segmental Glomerulosclerosis and Interferon Response. Am J Pathol *188*, 2745–2762. 10.1016/j.ajpath.2018.08.018.
182. Handy, D.E., and Loscalzo, J. (2011). Redox Regulation of Mitochondrial Function. Antioxidants & Redox Signaling *16*, 1323–1367. 10.1089/ars.2011.4123.

183. Kuo, C.-L., Lin, Y.-C., Lo, Y.K., Lu, Y.-Z., Babuharisankar, A.P., Lien, H.-W., Chou, H.-Y., and Lee, A.Y.-L. (2024). The mitochondrial stress signaling tunes immunity from a view of systemic tumor microenvironment and ecosystem. iScience *27*, 110710. https://doi.org/10.1016/j.isci.2024.110710.
184. Lingappan, K. (2018). NF-κB in Oxidative Stress. Curr Opin Toxicol *7*, 81–86. 10.1016/j.cotox.2017.11.002.
185. Mosallanejad, K., and Kagan, J.C. (2022). Control of innate immunity by the cGAS-STING pathway. Immunol Cell Biol *100*, 409–423. 10.1111/imcb.12555.
186. Grogan, B.C., Parker, J.B., Guminski, A.F., and Stivers, J.T. (2011). Effect of the Thymidylate Synthase Inhibitors on dUTP and TTP Pool Levels and the Activities of DNA Repair Glycosylases on Uracil and 5-Fluorouracil in DNA. Biochemistry *50*, 618–627. 10.1021/bi102046h.
187. Chatzidoukaki, O., Stratigi, K., Goulielmaki, E., Niotis, G., Akalestou-Clocher, A., Gkirtzimanaki, K., Zafeiropoulos, A., Altmüller, J., Topalis, P., and Garinis, G.A. (2021). R-loops trigger the release of cytoplasmic ssDNAs leading to chronic inflammation upon DNA damage. Science Advances *7*, eabj5769. doi:10.1126/sciadv.abj5769.
188. Jacobs, J.L., and Coyne, C.B. (2013). Mechanisms of MAVS regulation at the mitochondrial membrane. J Mol Biol *425*, 5009–5019. 10.1016/j.jmb.2013.10.007.
189. Liu, R., and Chan, D.C. (2017). OPA1 and cardiolipin team up for mitochondrial fusion. Nat Cell Biol *19*, 760–762. 10.1038/ncb3565.
190. Rhee, H.W., Zou, P., Udeshi, N.D., Martell, J.D., Mootha, V.K., Carr, S.A., and Ting, A.Y. (2013). Proteomic mapping of mitochondria in living cells via spatially restricted enzymatic tagging. Science *339*, 1328–1331. 10.1126/science.1230593.
191. Xu, Y., Erdjument-Bromage, H., Phoon, C.K.L., Neubert, T.A., Ren, M., and Schlame, M. (2021). Cardiolipin remodeling enables protein crowding in the inner mitochondrial membrane. Embo j *40*, e108428. 10.15252/embj.2021108428.
192. Ferreira, C., Pierre, G., Thompson, R., and Vernon, H. (1993). Barth Syndrome. In GeneReviews((R)), M.P. Adam, S. Bick, G.M. Mirzaa, R.A. Pagon, S.E. Wallace, and A. Amemiya, eds.
193. Koob, S., Barrera, M., Anand, R., and Reichert, A.S. (2015). The non-glycosylated isoform of MIC26 is a constituent of the mammalian MICOS complex and promotes formation of crista junctions. Biochim Biophys Acta *1853*, 1551–1563. 10.1016/j.bbamcr.2015.03.004.
194. Mao, X., Huang, D., Rao, C., Du, M., Liang, M., Li, F., Liu, B., and Huang, K. (2020). Enoyl coenzyme A hydratase 1 combats obesity and related metabolic disorders by promoting adipose tissue browning. American Journal of Physiology-Endocrinology and Metabolism *318*, E318–E329. 10.1152/ajpendo.00424.2019.
195. Xia, C., Fu, Z., Battaile, K.P., and Kim, J.-J.P. (2019). Crystal structure of human mitochondrial trifunctional protein, a fatty acid β-oxidation metabolon. Proceedings of the National Academy of Sciences *116*, 6069–6074. doi:10.1073/pnas.1816317116.
196. Gomes, F., Turano, H., Haddad, L.A., and Netto, L.E.S. (2024). Human mitochondrial peroxiredoxin Prdx3 is dually localized in the intermembrane space and matrix subcompartments. Redox Biol *78*, 103436. 10.1016/j.redox.2024.103436.
197. Kondadi, A.K., Anand, R., and Reichert, A.S. (2020). Cristae Membrane Dynamics - A Paradigm Change. Trends Cell Biol *30*, 923–936. 10.1016/j.tcb.2020.08.008.
198. Yu, R., Jin, S.B., Lendahl, U., Nistér, M., and Zhao, J. (2019). Human Fis1 regulates mitochondrial dynamics through inhibition of the fusion machinery. Embo j *38*. 10.15252/embj.201899748.
199. Shiiba, I., Takeda, K., Nagashima, S., and Yanagi, S. (2020). Overview of Mitochondrial E3 Ubiquitin Ligase MITOL/MARCH5 from Molecular Mechanisms to Diseases. Int J Mol Sci *21*. 10.3390/ijms21113781.

200. Schuettpelz, J., Janer, A., Antonicka, H., and Shoubridge, E.A. (2023). The role of the mitochondrial outer membrane protein SLC25A46 in mitochondrial fission and fusion. Life Sci Alliance *6*. 10.26508/lsa.202301914.
201. Chen, W., Zhao, H., and Li, Y. (2023). Mitochondrial dynamics in health and disease: mechanisms and potential targets. Signal Transduction and Targeted Therapy *8*, 333. 10.1038/s41392-023-01547-9.
202. Liu, Y., Merrill, R.A., and Strack, S. (2020). A-Kinase Anchoring Protein 1: Emerging Roles in Regulating Mitochondrial Form and Function in Health and Disease. Cells *9*. 10.3390/cells9020298.
203. Anand, R., Wai, T., Baker, M.J., Kladt, N., Schauss, A.C., Rugarli, E., and Langer, T. (2014). The i-AAA protease YME1L and OMA1 cleave OPA1 to balance mitochondrial fusion and fission. J Cell Biol *204*, 919–929. 10.1083/jcb.201308006.
204. Zhang, J., and Ney, P.A. (2009). Role of BNIP3 and NIX in cell death, autophagy, and mitophagy. Cell Death Differ *16*, 939–946. 10.1038/cdd.2009.16.
205. Jin, S.M., and Youle, R.J. (2012). PINK1- and Parkin-mediated mitophagy at a glance. Journal of Cell Science *125*, 795–799. 10.1242/jcs.093849.
206. Bhujabal, Z., Birgisdottir Å, B., Sjøttem, E., Brenne, H.B., Øvervatn, A., Habisov, S., Kirkin, V., Lamark, T., and Johansen, T. (2017). FKBP8 recruits LC3A to mediate Parkin-independent mitophagy. EMBO Rep *18*, 947–961. 10.15252/embr.201643147.
207. Bas, L., Papinski, D., Licheva, M., Torggler, R., Rohringer, S., Schuschnig, M., and Kraft, C. (2018). Reconstitution reveals Ykt6 as the autophagosomal SNARE in autophagosome–vacuole fusion. Journal of Cell Biology *217*, 3656–3669. 10.1083/jcb.201804028.
208. Bingol, B., Tea, J.S., Phu, L., Reichelt, M., Bakalarski, C.E., Song, Q., Foreman, O., Kirkpatrick, D.S., and Sheng, M. (2014). The mitochondrial deubiquitinase USP30 opposes parkin-mediated mitophagy. Nature *510*, 370–375. 10.1038/nature13418.
209. Cuinat, S., Bézieau, S., Deb, W., Mercier, S., Vignard, V., Isidor, B., Küry, S., and Ebstein, F. (2024). Understanding neurodevelopmental proteasomopathies as new rare disease entities: A review of current concepts, molecular biomarkers, and perspectives. Genes & Diseases *11*, 101130. https://doi.org/10.1016/j.gendis.2023.101130.
210. Shoshan-Barmatz, V., Maldonado, E.N., and Krelin, Y. (2017). VDAC1 at the crossroads of cell metabolism, apoptosis and cell stress. Cell Stress *1*, 11–36. 10.15698/cst2017.10.104.
211. Cristofani, R., Piccolella, M., Crippa, V., Tedesco, B., Montagnani Marelli, M., Poletti, A., and Moretti, R.M. (2021). The Role of HSPB8, a Component of the Chaperone-Assisted Selective Autophagy Machinery, in Cancer. Cells *10*. 10.3390/cells10020335.
212. Yamaguchi, R., Lartigue, L., Perkins, G., Scott, R.T., Dixit, A., Kushnareva, Y., Kuwana, T., Ellisman, M.H., and Newmeyer, D.D. (2008). Opa1-mediated cristae opening is Bax/Bak and BH3 dependent, required for apoptosis, and independent of Bak oligomerization. Mol Cell *31*, 557–569. 10.1016/j.molcel.2008.07.010.
213. Minin, A.A., Kulik, A.V., Gyoeva, F.K., Li, Y., Goshima, G., and Gelfand, V.I. (2006). Regulation of mitochondria distribution by RhoA and formins. Journal of Cell Science *119*, 659–670. 10.1242/jcs.02762.
214. Kreider-Letterman, G., Castillo, A., Mahlandt, E.K., Goedhart, J., Rabino, A., Goicoechea, S., and Garcia-Mata, R. (2022). ARHGAP17 regulates the spatiotemporal activity of Cdc42 at invadopodia. Journal of Cell Biology *222*. 10.1083/jcb.202207020.
215. Gross, S.R., Sin, C.G., Barraclough, R., and Rudland, P.S. (2014). Joining S100 proteins and migration: for better or for worse, in sickness and in health. Cell Mol Life Sci *71*, 1551–1579. 10.1007/s00018-013-1400-7.
216. Sato, O., Sakai, T., Choo, Y.Y., Ikebe, R., Watanabe, T.M., and Ikebe, M. (2022). Mitochondria-associated myosin 19 processively transports mitochondria on actin tracks in living cells. J Biol Chem *298*, 101883. 10.1016/j.jbc.2022.101883.

217. Coscia, S.M., Thompson, C.P., Tang, Q., Baltrusaitis, E.E., Rhodenhiser, J.A., Quintero-Carmona, O.A., Ostap, E.M., Lakadamyali, M., and Holzbaur, E.L.F. (2023). Myo19 tethers mitochondria to endoplasmic reticulum-associated actin to promote mitochondrial fission. Journal of Cell Science *136*. 10.1242/jcs.260612.
218. Kruppa, A.J., and Buss, F. (2018). Actin cages isolate damaged mitochondria during mitophagy. Autophagy *14*, 1644–1645. 10.1080/15548627.2018.1486152.
219. Gao, J., Schatton, D., Martinelli, P., Hansen, H., Pla-Martin, D., Barth, E., Becker, C., Altmueller, J., Frommolt, P., Sardiello, M., and Rugarli, E.I. (2014). CLUH regulates mitochondrial biogenesis by binding mRNAs of nuclear-encoded mitochondrial proteins. J Cell Biol *207*, 213–223. 10.1083/jcb.201403129.
220. Saxe, J.P., Chen, M., Zhao, H., and Lin, H. (2013). Tdrkh is essential for spermatogenesis and participates in primary piRNA biogenesis in the germline. Embo j *32*, 1869–1885. 10.1038/emboj.2013.121.
221. Hemono, M., Haller, A., Chicher, J., Duchene, A.M., and Ngondo, R.P. (2022). The interactome of CLUH reveals its association to SPAG5 and its co-translational proximity to mitochondrial proteins. BMC Biol *20*, 13. 10.1186/s12915-021-01213-y.
222. Herrmann, J.M., and Bykov, Y. (2023). Protein translocation in mitochondria: Sorting out the Toms, Tims, Pams, Sams and Mia. FEBS Lett *597*, 1553–1554. 10.1002/1873-3468.14614.
223. Mazur, M., Kmita, H., and Wojtkowska, M. (2021). The Diversity of the Mitochondrial Outer Membrane Protein Import Channels: Emerging Targets for Modulation. Molecules *26*. 10.3390/molecules26134087.
224. Nolte, H., MacVicar, T.D., Tellkamp, F., and Kruger, M. (2018). Instant Clue: A Software Suite for Interactive Data Visualization and Analysis. Sci Rep *8*, 12648. 10.1038/s41598-018-31154-6.